

2

AD-A264 002



PL-TR-92-2186

DTIC  
ELECTE  
APR 21 1993  
S C D

**MODELING REGIONAL SEISMIC WAVES**

**Donald V. Helmberger  
David G. Harkrider**

**California Institute of Technology  
Seismological Laboratory  
Division of Geological & Planetary Sciences  
Pasadena, CA 91125**

**29 June 1992**

**Scientific Report No. 1**

**APPROVED FOR PUBLIC RELEASE; DISTRIBUTION UNLIMITED**



**PHILLIPS LABORATORY  
Directorate of Geophysics  
AIR FORCE SYSTEMS COMMAND  
HANSCOM AFB, MASSACHUSETTS 01731-5000**

**93 4 20 065**

**93-08425**

REPORT DOCUMENTATION PAGE			Form Approved OMB No. 0704-0188	
<small>Public reporting burden for this collection of information is estimated to average 1 hour per response, including the time for reviewing the collection of information, searching existing data sources, gathering and maintaining the data needed, and completing and reviewing the collection of information. Send comments regarding this burden estimate or any other aspect of this collection of information, including suggestions for reducing this burden, to Washington Headquarters Services, Directorate for Information Operations and Reports, 1215 Jefferson Davis Highway, Suite 1204, Arlington, VA 22202-4302. Also send to the Office of Management and Budget, Paperwork Reduction Project (0704-0188), Washington, DC 20503.</small>				
1. AGENCY USE ONLY (Leave blank)		2. REPORT DATE 29 June 1992	3. REPORT TYPE AND DATES COVERED Scientific Report No. 1	
4. TITLE AND SUBTITLE Modeling Regional Seismic Waves			5. FUNDING NUMBERS PE 62101F PR 7600 TA 09 WU BA Contract F19628-90-K-0049	
6. AUTHOR(S) Donald V. HelMBERGER David G. HARKRIDER				
7. PERFORMING ORGANIZATION NAME(S) AND ADDRESS(ES) California Institute of Technology Seismological Laboratory Division of Geological & Planetary Sciences Pasadena, CA 91125			8. PERFORMING ORGANIZATION REPORT NUMBER	
9. SPONSORING/MONITORING AGENCY NAME(S) AND ADDRESS(ES) Phillips Laboratory Hanscom AFB, MA 01731-5000  Contract Manager: James Lewkowicz/GPEH			10. SPONSORING, MONITORING AGENCY REPORT NUMBER  PL-TR-92-2186	
11. SUPPLEMENTARY NOTES				
12a. DISTRIBUTION/AVAILABILITY STATEMENT  Approval for public release: distribution unlimited			12b. DISTRIBUTION CODE	
13. ABSTRACT (Maximum 200 words) <p>This research performed under the contract, during the period 26 September 1990 through 25 September 1991, can be divided into two main topics; determining compressional velocity by modeling waveforms and travel time data from long-period and short-period recordings and determining surface wave magnitudes for NTS events using regional data.</p> <p>In section 1, we derive a compressional velocity model for the northwest Atlantic Ocean by modeling wave form and travel time data from long-period and short-period WWSSN and Canadian network station recordings. A ninety kilometer thick lid with the velocity of 8.1 km/sec at the top gradually changing to 8.3 km/sec at the bottom is obtained by fitting the travel time data of first arrivals and waveform data of pure oceanic paths at distance of 8 - 20 degrees. Triplication P waveform data constrains the structure below the lid. A distinct low velocity zone is located at depth of about 170 km. Combining with the shear wave structure derived by Grand and HelMBERGER (1984a) for the same region, we can infer a very oliving-rich mineralogy in the upper 100 km and a very garnet - rich mineralogy at the depth of 200 - 400 km, at which partial melting should be also responsible for the very high <math>V_p/V_s</math> ratio.</p> <p>In section 2, we re-examine the use of surface wave magnitudes as a determination of</p>				
14. SUBJECT TERMS Generic model Broad-band modeling Regional events		Northeast US M <sub>s</sub> Regional surface wave magnitudes		15. NUMBER OF PAGES 114
		Site effects		16. PRICE CODE
17. SECURITY CLASSIFICATION OF REPORT Unclassified	18. SECURITY CLASSIFICATION OF THIS PAGE Unclassified	19. SECURITY CLASSIFICATION OF ABSTRACT Unclassified	20. LIMITATION OF ABSTRACT SAR	

yield of under-ground explosions and the associated magnitude-yield scaling relationship. We have calculated surface wave magnitudes for 190 Nevada Test Site (NTS) underground nuclear explosions from a data set of regional long-period seismograms from a combined super-network of 55 North American stations. Great effort went towards making the data set comprehensive and diverse in terms of yield, source location and shot medium in order to determine the portability of surface wave magnitude scales. In particular, we examine Pahute Mesa, Rainier Mesa and Yucca Flat explosions detonated above and below the water table that range in yield over three orders of magnitude. By observation we find a log-yield measure threshold of approximately one kiloton for (assumedly) moderately well-coupled explosions recorded at near regional (< 500 km), seismically "reasonably quiet" stations. In order to utilize the nearer regional stations ( $\Delta < 20^\circ$ ), we have developed several related methods for determining time domain surface wave magnitudes or scalar moments from regional Rayleigh waves, thus enhancing the utility of surface wave information for seismic event magnitude quantifying and discrimination purposes. One technique employs synthetic seismograms to establish a relationship between the amplitude of the regional Airy phase, or Rayleigh pulse of the Rayleigh wave-train and an associated surface wave magnitude, based on conventional  $M_s$  determinations, calculated from a synthetic seismogram propagated to  $40^\circ$ . The other method uses synthetic seismograms in a similar fashion, but the relationship used is a more straight forward one between scalar moment and peak Rayleigh wave amplitude. Path corrections are readily implemented to both methods. The inclusion of path corrections decreases the  $M_s$  variance by a factor of two and affects the absolute scaling relationship by up to a factor of 0.1 magnitude units. This latter effect is attributed to the particular station network used and the Green's function used to obtain the  $40^\circ M_s$  values. Using a generic structure for the distance traveled past the actual source receiver path minimizes the difference between magnitudes determined with and without path corrections. The method gives stable  $M_s$  values that correlate well with other magnitude scale values over a range of three orders of magnitude in source yield. Our most refined  $M_s$  values give the relationship  $M = 1.00 \times \log(\text{yield}) + B$ , where B is dependent upon source region and shot medium. This yield exponent of unity holds for events of all sizes and is in line with  $M_s$ -yield scaling relations found by other studies. When events are grouped with respect to source region, significantly better fits to these individual site linear regression curves are obtained compared to the fits obtained using a single, all inclusive model. This observation implies that shot site parameters and source structure affect surface wave magnitude measurements, although event yield-site distribution also may be in part responsible.

Since our magnitude values are based on a theoretical continental structure, we regressed our values with more standard teleseismic  $M_s$  values from several other studies. For all comparisons, our  $M_s$  values scaled favorably with the others, however absolute magnitude curves varied by  $\pm 0.5$  magnitude units. These differences are due in part to the choice of  $M_s$  formula used. It is also possibly due to differences in network station distribution between the studies, with this study using more nearer stations, as well as a wider range of station azimuths.

**INTERIM TECHNICAL REPORT**  
26 September 1990 - 25 September 1991

ARPA Order No: 5307

Name of Contractor: California Institute of Technology

Effective Date of Contract: 26 September 1990

Contract Expiration Date: 25 September 1991

Contract Number: F19628-90-K-0049

Principal Investigators: Donald V. Helmberger  
(818) 356-6998

David G. Harkrider  
(818) 356-6910

Program Manager: James F. Lewkowicz  
(617) 861-3028

Short Title of Work: Modeling Regional Seismic Waves

The views and conclusions contained in this document are those of the authors and should not be interpreted as necessarily representing the official policies, either expressed or implied, of the Defense Advance Research Projects Agency or the U. S. Government.

Sponsored by  
Defense Advanced Research Projects Agency (DoD)  
Nuclear Monitoring Research Office  
ARPA Order No. 5307  
Issued by the Air Force Geophysics Laboratory under  
Contract #F19628-90-K-0049

Seismological Laboratory  
Division of Geological and Planetary Sciences  
California Institute of Technology  
Pasadena, California 91125

**DTIC QUALITY INSPECTED 1**

Accession For	
NTIS CRA&I	<input checked="" type="checkbox"/>
DTIC TAB	<input type="checkbox"/>
Unannounced	<input type="checkbox"/>
Justification	
By _____	
Distribution /	
Availability Codes	
Dist	Avail and/or Special
A-1	

## TABLE OF CONTENTS

	Page #
Summary .....	V
Section 1. Exploration of the lower lithosphere; Northeastern United States.....	1
Section 2. Determining surface wave magnitudes from regional NTS.. data .....	37

## Summary

This research performed under the contract, during the period 26 September 1990 through 25 September 1991, can be divided into two main topics; modeling broadband seismograms from moderate-sized earthquakes at regional distances and determining surface wave magnitudes for NTS events using regional data.

In section 1, we report on modeling broadband seismograms from moderate-sized earthquakes at regional distances. We demonstrate that the longer period motions (WWSSN) preceding the direct S arrival can be modeled reasonably well with a crustal model consisting of a layer over a halfspace. While a generic model assumed to be the same everywhere, can be used to model the  $P_{n1}$  waveshape, Helmberger and Engen (1980), some adjustments are required to fit the  $P_n$  and  $S_n$  timing for specific paths. Inversion of 3-component seismograms assuming such simple models prove effective in source retrieval using a single station. Shorter periods can then be modeled by adding more detail to the velocity structure holding the source fixed and the process repeated.

Application of this modeling procedure to earthquakes occurring in the New England region proves interesting. In particular, paths on opposite sides of the Appalachian Thrust Belt produce distinct models. Paths along the western side of the Belt can be modeled with an average crustal thickness of 35 km, the compressional and shear velocities of the crust are 6.5 and 3.6-3.7 km/sec, and those of the upper mantle 8.4-8.5 and 4.7-4.8 km/sec respectively. The results are in agreement with the normal shield parameters, see LeFevre and Helmberger (1989) and Grand and Helmberger (1984). Paths along the eastern side of the Belt indicate more variability but yield consistently slower lithospheric velocities by 3 to 4% for P-waves. These models predict P-wave travel time delays across this zone of about 0.3 seconds in agreement with direct observations obtained by Taylor and Tököz (1979) and with their preferred interpretation.

In section 2, we re-examine the use of surface wave magnitudes as a determination of yield of under-ground explosions and the associated magnitude-yield scaling relationship. We have calculated surface wave magnitudes for 190 Nevada Test Site (NTS) underground nuclear explosions from a data set of regional long-period seismograms from a combined super-network of 55 North American stations. Great effort went towards making the data set comprehensive and diverse in terms of yield, source location and shot medium in order to determine the portability of surface wave magnitude scales. In particular, we examine Pahute Mesa, Rainier Mesa and Yucca Flat explosions detonated above and below the water table that range in yield over three orders of magnitude. By observation we find a log-yield measure threshold of approximately one kiloton for (assumedly) moderately well-coupled explosions recorded at near regional ( $< 500$  km), seismically "reasonably quiet" stations. In order to utilize the nearer regional stations ( $\Delta < 20^\circ$ ), we have developed several related methods for determining time domain surface wave magnitudes or scalar moments from regional Rayleigh waves, thus enhancing the utility of surface wave information for seismic event magnitude quantifying and discrimination purposes. One technique employs synthetic seismograms to establish a relationship between the amplitude of the regional Airy phase, or Rayleigh pulse of the Rayleigh wave-train and an associated surface wave magnitude, based on conventional  $M_s$  determinations, calculated from a synthetic seismogram propagated to  $40^\circ$ . The other method uses synthetic seismograms in a similar fashion, but the relationship used is a more straight forward one between scalar moment and peak Rayleigh wave amplitude. Path corrections are readily implemented to both methods. The inclusion of path corrections decreases the  $M_s$  variance by a factor of two and affects the absolute scaling relationship by up to a factor of 0.1 magnitude units. This latter effect is attributed to the particular station network used and the Green's

function used to obtain the  $40^\circ M_s$  values. Using a generic structure for the distance traveled past the actual source receiver path minimizes the difference between magnitudes determined with and without path corrections. The method gives stable  $M_s$  values that correlate well with other magnitude scale values over a range of three orders of magnitude in source yield. Our most refined  $M_s$  values give the relationship  $M = 1.00 \times \log(\text{yield}) + B$ , where  $B$  is dependent upon source region and shot medium. This yield exponent of unity holds for events of all sizes and is in line with  $M_s$ -yield scaling relations found by other studies. When events are grouped with respect to source region, significantly better fits to these individual site linear regression curves are obtained compared to the fits obtained using a single, all inclusive model. This observation implies that shot site parameters and source structure affect surface wave magnitude measurements, although event yield-site distribution also may be in part responsible.

Since our magnitude values are based on a theoretical continental structure, we regressed our values with more standard teleseismic  $M_s$  values from several other studies. For all comparisons, our  $M_s$  values scaled favorably with the others, however absolute magnitude curves varied by  $\pm 0.5$  magnitude units. These differences are due in part to the choice of  $M_s$  formula used. It is also possibly due to differences in network station distribution between the studies, with this study using more nearer stations, as well as a wider range of station azimuths.

SECTION 1

Exploration of the Lower Lithosphere; Northeastern United States

# Exploration of the Lower Lithosphere; Northeastern United States

D. V. Helmberger, L. S. Zhao, D. Dreger and V. LeFevre

## Abstract

In this study we report on modeling broadband seismograms from moderate-sized earthquakes at regional distances. We demonstrate that the longer period motions (WWSSN) preceding the direct S arrival can be modeled reasonably well with a crustal model consisting of a layer over a halfspace. While a generic model assumed to be the same everywhere, can be used to model the  $P_{nl}$  waveshape, Helmberger and Engen (1980), some adjustments are required to fit the  $P_n$  and  $S_n$  timing for specific paths. Inversion of 3-component seismograms assuming such simple models prove effective in source retrieval using a single station. Shorter periods can then be modeled by adding more detail to the velocity structure holding the source fixed and the process repeated.

Application of this modeling procedure to earthquakes occurring in the New England region proves interesting. In particular, paths on opposite sides of the Appalachian Thrust Belt produce distinct models. Paths along the western side of the Belt can be modeled with an average crustal thickness of 35 km, the compressional and shear velocities of the crust are 6.5 and 3.6-3.7 km/sec, and those of the upper mantle 8.4-8.5 and 4.7-4.8 km/sec respectively. The results are in agreement with the normal shield parameters, see LeFevre and Helmberger (1989) and Grand and Helmberger (1984). Paths along the eastern side of the Belt indicate more variability but yield consistently slower lithospheric velocities by 3 to 4% for P-waves. These models predict P-wave travel time delays across this zone of about 0.3 seconds in agreement with direct observations obtained by Taylor and Töksoz (1979) and with their preferred interpretation.

## Introduction

Seismic exploration of the lithosphere has progressed substantially in recent years based on a host of new types of analytical techniques and broadband data systems. New methods ranging from the inversion of teleseismic waveforms for receiver structures, modeling of 2-D seismic sections and 3-D tomographic imaging have renewed interest in relating velocity structures with geologic features, see Pakiser and Mooney (1989). One of the newest data acquisition systems available is the IRIS broadband digital stations consisting of the Wielandt-Streckeisen sensor and the Quanterra data logger. With the development of this equipment, we are able to observe seismic phenomenon never seen before. This is especially true at local and regional distances where signals have not suffered mantle attenuation and thus the broadband features of this system allow

us to see obvious propagational effects such as head waves and critical reflections. For example, fig. 1 displays such a set of seismograms from a recent Californian Earthquake recorded at Pasadena. The  $S_n$  arrival is long period as is made clear by filtering the broadband motions using conventional long, intermediate, and short period responses. The long period motions separate into the (P-SV) and (SH) systems of motion reasonably well, at least up to about the  $S_mS$  phase, (moho reflection). Note that the tangential motions remain small until  $S_n$  arrives. As the frequency increases this separation becomes less clear and appears to be path dependent as suggested in fig. 2. At HRV the  $P_n$  and  $P_g$  on the tangential component appears to be considerably smaller than on the PAS recordings. This phenomenon suggests a simpler receiver function at HRV which would not be unexpected.

In general, we find better separation of the (P-SV) and (SH) systems in eastern U.S. than in western U.S. Broadband seismograms for southern California are discussed at length in a recent paper by HelMBERGER, et al. (1991), in which they find that the broadband seismograms become increasingly complex after the onset of the direct S arrival. Since the primary surface waves, generated near the source, and secondary surface waves, generated near the receiver, are both strongly affected by shallow structure, this result is not surprising, see Stead (1989) and Ho-Liu and HelMBERGER (1989). For these reasons we will concentrate on the early portion of regional records, essentially the wavetrain preceding the surface waves, see fig. 2. The ray paths followed by these early arrivals  $P_n$  and  $S_n$  sample the faster lower crust and upper mantle and prove particularly effective in exploring the upper hundred kilometers of the mantle.

The events discussed in this report are located in fig. 3 along with recording stations consisting of WWSSN and a few modern stations at State College (SCP) and Harvard (HRV). The latter station produced the broadband motions given in fig. 2 of the 1988 Saguenay, Quebec earthquake. It is the only regional station that did not clip on the surface waves because of its large dynamic range. Fortunately, many of the long period WWSSN stations produced useful pre-direct S wavetrain signals for the three events considered.

We will address modeling these records in two stages of increasing detail. In the first stage, we model the  $P_{nl}$  portion of these records assuming a generic crustal model where we neglect absolute timing. This procedure allows us to determine the seismic source parameters. The second stage of modeling includes the faster crustal S-wave phases  $S_n$  and  $sS_n$  as well as consideration of absolute timing. Modeling at this level reveals that some shallow geological boundaries persist into the mantle. In particular, the lithosphere has distinctly different properties on the western and eastern sides of the Appalachian Thrust Belt (ATB) which forms the boundary of an old suture zone. We will demonstrate the usefulness of modeling regional phases along these interesting paths.

### Source Estimation from Modeling $P_{nl}$

Long-period body waves contain a great deal of information about the overall size and average source processes of an earthquake. In particular, seismic moment and source mechanism may be determined by teleseismic body-wave modeling (Langston and Helmberger, 1975). However, earthquakes in the magnitude range  $5 < m_b < 6$  often are not well-recorded teleseismically. For these events, long-period body waves at distances of less than about  $30^\circ$  provide useful data for waveform analysis.

Whereas teleseismic P-wave modeling requires consideration of only three rays, direct P and the surface reflections pP and sP, waveform modeling at less than  $30^\circ$  requires summation of many more arrivals. At distances of less than about  $15^\circ$ , the seismogram is dominated by waves traveling along the top of mantle and in the crustal waveguide. In terms of rays, the wavetrain includes rays which have undergone multiple reflections within the crust, including mode conversions at the free surface and at the Mohorovicic discontinuity. The initial part of the record is dominated by P headwaves (Pn) and the later part of the record includes more SV energy (PL). We refer to the entire wavetrain before the S-wavetrain as  $P_{nl}$ . At the longer periods, the waveform of  $P_{nl}$  is relatively insensitive to details of crustal structure but is quite sensitive to the source orientation of the event.

One method of computing the  $P_{nl}$  synthetic seismograms is discussed in detail in Helmberger and Engen (1980) and Wallace, et al. (1981). Briefly, a simple layer-over-half-space model is used to represent the crust and Mohorovicic discontinuity. Green's functions are computed by summing generalized rays for various paths through the model. For example, the vertical displacement can be written as

$$w(r, z, t) = \left( \frac{M_0}{4\pi\rho_0} \right) \left[ \left( \dot{D}(t) * \sum_{i=1}^3 W_i(t) \times A_i \right) \right] \quad (1)$$

where  $M_0$  is the seismic moment,  $\rho_0$  the source region density,  $\dot{D}(t)$  the far-field time history,  $W_i$  are the Green's functions for the three fundamental faults, and  $A_i$  are orientation constants which depend on the source orientation. These Green's functions were computed by summing generalized rays. Since the computation of the Green's functions is rather time consuming, they are computed for each of the fundamental faults, at 100 km intervals from 200 to 2000 km, and stored. A synthetic for any desired fault orientation can then be created by computing the appropriate  $A_i$ 's, summing, and convolving with the instrument response and source time function. When the desired distance falls between those of the Green's functions, the closest distance is used rather than recomputing the Green's functions for the exact distance. This is an adequate approximation since the  $P_{nl}$  waveforms at adjacent distances do not change abruptly (Helmberger and Engen, 1980). The Green's functions were calculated for an average crustal structure with a thickness of 32 km, essentially it is a generic model used in many regions. An

example set of Green's functions,  $W_i$ , are displayed in fig. 4 as a function of source depth. These Green's functions were computed by summing generalized rays. For sources below the crust the direct P-arrival becomes relatively strong but the basic  $P_{nl}$  wavetrain persists. The strong short period signals are not direct S but converted S to P arrivals that bounce in the crust. Direct S arrives much later.

For the events in this study previously-determined focal mechanisms, obtained from first motions, teleseismic body-wave modeling or surface wave spectral amplitude studies, were available and seismic moments had been estimated. We used these focal mechanisms as a starting model and adjusted them if the fit of the synthetic seismograms to the data was unsatisfactory. A revised seismic moment was calculated by a comparison of observed to synthetic amplitudes.

a) New Brunswick earthquake, 9 January 1982

This earthquake was the mainshock of the New Brunswick sequence. An inversion of teleseismic bodywave data was performed by Nabelek (1984) to determine source orientation, time function, and moment. He found strike =  $175^\circ$ , dip =  $54^\circ$ , rake =  $85^\circ$ , source depth = 7 km, and  $M_0 = 1.6 \times 10^{24}$  dyne-cm. Four stations provided usable waveforms for  $P_{nl}$  modeling. Three are WWSSN or Canadian, long-period (analog) records, and one is from the digital WWSSN station SCP. Data and synthetic waveforms are shown in fig. 5. Both have been convolved with a 2 sec triangle, which has little effect on the data but removes high frequencies from the synthetic waveforms. The synthetic waveforms were generated using the mechanism determined by Nabelek, and a trapezoidal time function (0.2, 0.4, 0.2 s) based on his estimate of overall source duration. The synthetics fit very well for this mechanism, and since all four stations with useable  $P_{nl}$  waveforms are in a narrow range of azimuth, there seems to be little point in attempting to adjust the mechanism for this dataset.

The excellent fit of the records for this event shows that the layer-over-a-halfspace model is adequate for fitting even many of the details of the long-period waveforms. It is unfortunate that only a narrow azimuth range is represented by these stations, and station WES is nearly nodal. However, since the agreement with the data is so good, all stations are included in the moment calculation. The seismic moment determined is  $1.3 \times 10^{24}$  dyne-cm, which is in very good agreement with the body-wave calculation of Nabelek (1984).

b) Kentucky, 27 July 1980

The Sharpsburg, Kentucky earthquake of 27 July 1980 occurred in eastern Kentucky, west of the Appalachian front in an area of low historical seismic activity. NEIS assigned this event a depth of 8 km. A well-constrained, first-motion mechanism presented by Mauk et al. (1982) gives strike-slip movement of strike= $42^\circ$ , dip= $50^\circ$ , and slip= $184^\circ$ . Hermann et al. (1982) studied surface-wave spectral amplitudes, performing a search for the best-fitting focal mechanism. They found a similar mechanism of strike= $30^\circ$ , dip= $60^\circ$ , and slip= $180^\circ$ , and a depth of 14 to 22 km.

The moment calculated from the surface waves varies considerably with depth. Assuming a depth of 18 km, they calculated a seismic moment of  $4.1 \times 10^{23}$  dyne-cm. They also modeled teleseismic short-period waves, which give a better resolution of depth. This gave a depth of 12 km, and a triangular time function with 0.8 sec rise and 0.2 sec fall.

Eight stations produced usable long-period records for  $P_{nl}$  modeling. Five are WWSSN stations within the eastern US and three are from the Canadian network, with distances ranging from 329 to 1216 km. This event is near the lower limit of seismic moment, which can be modeled using  $P_{nl}$ , and the signal-to-noise ratio is very small at some stations, as illustrated in fig. 6, see WES for example. At most stations, only the vertical component could be used. Radial components were obtained for three stations (BLA, FVM, and LHC).

Data and synthetic waveforms for this event are presented in fig. 6 where both sets of waveforms are convolved with a 1.5 s triangle. Considering the noise level of the data, the fit of the synthetic seismograms to the data is in general quite good. Adjustments to the focal mechanism were tried but did not improve the fits, and the mechanism of Herrmann et al. (1982) is used. The best fits are at the less distant stations, and at the stations away from the nodes: LHC, FVM, and BLA. Non-linearity of the instrument response may cause the later part of the FVM radial component to be poorly fit. The first two cycles at SHA are well fit but the data do not show the ringing character of the synthetic seismogram. However, the amplitude of this record was very small. Station GEO displays similar behavior in that the overall features of the waveform are matched, but fit in detail is not as good, partly because of the high noise level. The waveform fit is surprisingly good at nodal station WES but less good at near-nodal stations OTT and MNT. Deeper mantle structure (>50 km) begins to effect the  $P_n$  waveforms at the greater distances and a more refined structural model becomes necessary, see LeFevre and Helmberger (1989).

In determination of seismic moment, stations MNT and OTT are not included, since these stations are more distant, near-nodal, and the fit is not satisfactory. Averaging the remaining nine records (three radial and six vertical) gives  $M_0 = 7.5 \times 10^{23}$  dyne-cm, which is approximately twice the surface-wave estimate of Herrmann et al. (1982).

### c) Chicoutimi earthquake

The Chicoutimi or Saguenay earthquake,  $m=5.8$ , occurred on November 1988 and was one of the largest earthquakes to occur in eastern North America in two decades. This event as well as a number of historic events have occurred beneath the St. Lawrence River Basin, called the Charlevoix seismic zone, North et al. (1989), and has been studied extensively. The event proved to be almost pure thrust centered at a depth of 26 km as determined from surface reflected phases:  $pP$ ,  $sS$ , etc., Somerville et al. (1990).

A source duration of 1.8 secs and a moment of  $5 \times 10^{24}$  was obtained by modeling teleseismic waveforms. Observations from four stations used in the  $P_{nl}$  analysis are displayed in fig. 7. Unfortunately, severe microseisms greatly reduced the signal-to-noise ratio of most of the

Canadian Network. Fig. 7 compares recorded and synthetic  $P_{nl}$  waveforms for the preferred focal mechanism. Note that SCP is a GDSN digital station; OTT and SCH are analog; and IHC is a digital Streckeisen recording filtered with a WWSSN instrument response for a conventional mechanism determination. We will return to a broadband analysis of this station later. Fig. 8a displays the depth sensitivity of simple  $P_{nl}$  waveforms where the depth was varied from 18 to 30 km. An overlay of the observed waveforms with synthetics favors the depths near 27 kms. The observation at BLA displayed in figure 8b is near the cross-over in distance,  $\Delta=1400$  km, where energy from beneath the lithosphere begins to contribute and sharpens the  $P_n$  into P etc., see LeFevre and Helmberger (1989).

### Velocity Estimation from modeling regional seismograms

In the previous section we used a generic layer over a halfspace model to match observed  $P_{nl}$  waveform data to constraint source parameters. These waveform matches are quite good but they generally do not fit the absolute travel time, nor do they explain broadband observations. Some progress in modeling the latter has been made by Zhao and Helmberger (1991) for a path from Chicoutimi to HRV see fig. 9. The model obtained from this detailed forward modeling effort, MPM, is given in fig. 10 along with a Canadian Shield type model. (SNA and S25), and a relatively fast idealized model SPT discussed later.

The synthetic fits displayed in fig. 9 were obtained by breaking the seismogram into sections where the waveforms of each segment prove sensitive to a particular portion of the waveguide. Three divisions appear to be the most useful, namely the  $P_{nl}$  segment discussed earlier, the  $S_{nl}$  segment containing  $S_n$ ,  $sS_n$ ,  $S_mS$ , and its multiples and the fundamental Rayleigh wave segment. Synthetics were generated by a variety of methods including reflectivity, normal modes and generalized rays.

The most difficult portion of these records to model occurs near times corresponding to direct S. The laterally varying surface layer (top few kms) appears to be causing the most difficulties, see Helmberger et al. (1991), where S-coupled PL waves can be severely scattered at regional distances. The easiest portion of these records to model is the section blown-up in fig. 11, namely the first 100 secs before the direct S wave arrival. As discussed by Zhao and Helmberger (1991) the vertical component is expected to have the strongest  $S_{nl}$  wavetrain based on theoretical considerations.

The tangential motions or SH system is generally easier to handle than the P-SV system but is not so important at this particular station since  $S_n$  is nearly nodal as indicated in fig. 11. Also included in fig. 11 is the best fitting one layer model, (LPM) which does a reasonable job and since it has so few parameters it appears to be an obvious model to use as a basis for direct source inversion attempts as discussed later.

Both the one-layered model (LPM) and the complete model (MPM) displayed in fig. 10 are

relatively slow compared to previous studies of the eastern portion of the North American continent, see LeFevre and Helmberger (1989) and Grand and Helmberger (1984). However, this disagreement appears to be related to the local regional geology as displayed in fig. 12 where the paths east of the ATB are distinctly slower than paths to the west. The best example of the basic differences in velocities is obtained in modeling the Chicoutimi earthquake at SCP, which is following a path just to the west of the thrust-belt. Fits of three possible models to the SCP long period digital data is given in fig. 13. Unfortunately, the intermediate frequency band data is not available and the long period motions clip on the surface waves. The synthetic fits to  $P_n$  and  $S_n$  in timing favor model SPT although the PL portion would favor a slightly slower crust. Both models are very fast indicating a 3% jump in mantle P-velocity across this old suture zone boundary, see fig. 12. Synthetics and observed seismograms for other paths crossing this region are displayed in fig. 14. The path from New Brunswick to WES is relatively slow with the LPM model producing good results. The path is not that far from the Chicoutimi-HRV path so it might be expected to compare well. In contrast, the New Brunswick to SCP path appears to be intermediate in velocity with the  $S_n$  (tangential component) and  $P_n$  (vertical) nearly matching LPM but somewhat faster but not as fast as SPT.

Our results are in excellent agreement with the observations reported on by Taylor and Töksoz (1979), see fig. 12. These travel time residuals suggest a jump of about .6 secs crossing the northern portion of the Appalachian Thrust Belt. It is difficult to explain such large variations without changing the crustal thickness. In this case, the crustal thickness must be nearly the same since Bouguer gravity anomalies do not follow this boundary as discussed by Taylor and Töksoz (1982). They attribute a possible differential of .2 secs by thickening the crust by 3 km on the eastern side. They suggest that the remaining (.4) secs must be accommodated by the mantle. Our results suggest that the velocity contrast of (8.25-10-8.5) down to a depth of 150 km would explain this differential offset. Unfortunately, the residual data ends at the US-Canadian boundary so it becomes difficult to gain supporting evidence to north.

### Implications

In this section we will address some of the practical implications involving the acquisition of the new broadband regional data introduced earlier. We will first discuss how this data can be used in source inversion using very few stations and secondly, we will address the sensitivity of regional phases to directivity. The latter issue will become more important with the addition of more broadband stations.

Although regional phases are relatively complicated they do contain an immense amount of information about source properties as discussed above. To take advantage of this information is difficult but is greatly aided by multiple events in the same region, mainshock-aftershock sequence for example, see Dreger and Helmberger (1991). Such situations allow for the determination of

directivity, asperity distributions, etc. Nevertheless, a great deal can still be learned by treating events as point-sources and inverting for the usual fault-parameter given a set of regional Green's functions for example see Dreger et.al. (1991).

### Source Estimation

Previously, we demonstrated the usefulness of the model MPM in matching data for the eastern New England region. A set of these Green's function is displayed in fig. 15. These functions have been truncated near the onset of direct S to emphasize the most stable portion of these responses which can be used in source inversion. A reference line with the  $S_n$  velocity of 4.6 has been added for convenience in comparing responses. At the shortest distances the responses are limited to  $P_n$  and PL phases with very little  $S_n$ . As the range increases the phase  $sS_n$  becomes apparent. Note that it has the opposite polarity of  $S_n$  for the dip-slip case. The sharp spikes following  $S_n$  and  $sS_n$  at the larger distances are lower lithospheric reflections indicated by the dotted lines in fig. 15. The vertical responses show a distinct difference between the strike-slip and dip-slip cases where the ratio of  $P_n$  to PL excitation becomes apparent. The weakness of  $S_n(SV)$  for the dip-slip case relative to the strike-slip case is, also, apparent. Note that the phase  $S_n(SV)$  is allied transformed relative to  $S_n(SH)$  as discussed by Zhao and Helmberger (1991).

The utility of these Green's functions in source estimation is displayed in fig 16, where we assume that the observations can be modeled by summing a linear combination of the Green's function appropriate from the three fundamental fault orientations, strike-slip etc., see equation 1. The weighting determines the best estimates of strike, dip, and rake,  $(\theta, \delta, \lambda)$ , which maximizes the correlation coefficient between the data and synthetics. Fig. 16 displays the results for the above multi-layered model and the halfspace model (bottom). Both inversions start with the pure strike-slip case and iterate to the above orientations, see Dreger et. al (1991) for details of this particular method. A comparison of synthetics with data for a number of other source parameter studies, see Table I, is given in fig. 17. The nodal nature of  $S_n(SH)$  is obviously the main feature that distinguishes these models. Note that the two inversion results essentially bracket the Somerville et al. (1990) solution.

Although the fits between the data and synthetics displayed in fig. 16 are equally good, the corresponding whole seismogram comparison is not, see fig. 18. The layered model does much better since it was designed to fit the whole record, see Zhao and Helmberger (1991). However, the main point to recognize in this comparison is that we do not have to know very much about the upper crust to model the predirect S wave portion of the records.

### Directivity

One of the biggest advantages of the new IRIS instrumentation is the ability to recognize directivity. The dynamic range is necessary to compare  $P_n$  and  $S_n$  with the fundamental Rayleigh

wave and the broadband is necessary to see the various phase shifts in frequency content. Presently, we do not have enough of these stations to use this potential but we can simulate what we would expect to see for the well-studied Chicoutimi to HRV path. Four cases are considered assuming a line of five sources forming the diagonals of a rectangle fault plane, see fig. 7 where the northeast dipping plane is assumed to be the actual faulting surface. The fault plane is assumed to be a 5 by 5 km square. The simulated results assuming rupture along the diagonals is presented in fig. 19. The top traces show the broadband vertical data broken-up into two sections with a blow-up of the  $P_n$  and  $S_n$  portion on the left. The next row displays point source synthetics with a (.2,.2,.2) trapezoidal source, essentially all the moment in one asperity. Simulation of ruptures along various directions is constructed by adding 5 point sources with lags appropriate for a rupture velocity of 3.5 km/sec. Each source has (1/5) the total moment. Rupture downward clearly enhances  $P_n$  while rupture upward strengthens  $sP_n$ . The rupturing away cases tend to enhance the surface waves relative to the bodywaves since the latter are reduced by lengthening. The up and towards case appears to fit the data better than the point source case but clearly more calibrated stations would be needed to be definitive. Large aftershocks would be particularly useful for this purpose, see Dreger & Helmberger (1991).

### Conclusions

This paper demonstrates the usefulness of regional broadband data in the exploration of the lower lithosphere. Regional earthquakes are used as sources with their relatively strong shear wave excitation. Thus, we obtain shear velocity structure at depths not obtainable from controlled sources. The main disadvantage of working with earthquakes is that we must separate earthquake source excitation from propagational distortions caused by the structure. An iterative approach to this complexity was introduced where we start with a generic model: layer over a halfspace, and estimate the long period source properties. This proves possible for the bodywave portion of these records where the surface wave portion is neglected. With the source fixed we adjust the structural parameters to produce a more satisfactory fit in timing,  $P_n$ ,  $S_n$ , etc. Applying a waveform inversion code to this refined model allows a more detailed resolution of the source excitation. The whole procedure can be repeated where shorter period information is explained by adding more detailed structure. At this stage we could add the surface wave portion of the seismograms which is generally controlled by the upper crust at these ranges and period, Zhao and Helmberger (1991).

An application of above strategy to some events along the New England-Canadian boundary proved interesting. In particular, the Chicoutimi event (Nov. 25, 1988, Quebec) occurred near the northern extension of the Appalachian Thrust Belt, ATB. The path to SCP (College Station, Penn) travels along the western side of the ATB and yielded mantle velocities of 8.4-8.5 and 4.7-4.8 km/sec respectively. These results are in agreement with normal shield parameters, Grand and Helmberger (1984) and LeFevre and Helmberger (1989) and are expected

for the Greenville province. The path to HRV (Harvard, Mass) follows the eastern side of the ATB zone yields slower mantle velocities by 2 to 3% with some structural detail in the lower lithosphere. These models prove effective in explaining other paths in the region, namely from the New Brunswick event. Details of the crustal structure and the sharpness of the crust-mantle transition were not resolved in this region but only that the P and S travel time-delays across the ATB are not greatly different in this region. This conclusion is substantiated by gravity surveys and (COCORP) profiles, although the reflectivity of various crustal sections show considerable variation, Taylor (1989). Thus, our P-wave travel time delay of .3 secs represent the differences in mantle models across the ATB. Taylor and Töksoz (1982) report on a detailed travel time delay survey in New England and find a sharp jump in values crossing the ATB in basic agreement with our results. Clearly, more earthquakes and further refinement of the techniques discuss here should help clarify the nature of this old suture zone boundary and other shallow mantle anomalies not easily resolved by other methods.

#### Acknowledgements

We would like to thank Hiroo Kanamori for his review. This research was supported by NSF EAR-8904767 and by the Advanced Research Projects Agency of the Department of Defense and was monitored by the Phillips Laboratory under the contract F19628-90-K-0049. Contribution No. 5035, Division of Geological and Planetary Sciences, California Institute of Technology, Pasadena, California.

## References

- Carabajal, C., C., and J. S. Barker, Source Processes and Wave Propagation effects of the November 25, 1988, Saguenay, Quebec Earthquake, *E.O.S.*, April 1991.
- Dreger, D. S., and Helmberger, D. V., Complex Faulting Deduced from Broadband Modeling of the 28 February 1990 Upland Earthquake ( $M_L=5.2$ ) *Bull. Seismol. Soc. Am.*, August 91 (V.81).
- Dreger, Douglas S., Helmberger, Donald V., Zhao, Lian-She, Three component waveform inversion of regional earthquakes: The October 24, 1990 Lee Vining event, submitted to *Bull. Seismol. Soc. Am.*, 1991.
- Grand, S. P., and D. V. Helmberger, Upper mantle shear structure of North America, *Geophys. J. R. Astr. Soc.*, 76, 399-438, 1984b.
- Helmberger, D., R. Stead, P. Ho-Liu, and D. Dreger, Broad-band modeling of regional seismograms; Imperial Valley to Pasadena, *Geophys. J.*, Submitted, 1991.
- Helmberger, D. V., and G. R. Engen, Modeling the long-period body waves from shallow earthquakes at regional ranges, *Bull. Seismol. Soc. Am.*, 70, 1699-1714, 1980.
- Herrmann, R. B., C. A. Langston, and J. E. Zollweg, The Sharpsburg, Kentucky, earthquake of 27 July 1980, *Bull. Seismol. Soc. Am.*, 72, 1219-1239, 1982.
- Ho-Liu, P., and D. Helmberger, Modeling regional love waves: Imperial Valley to Pasadena, *Bull. Seismol. Soc. Am.*, 79, 1194-1209, 1989.
- Langston, C. A., and D. V. Helmberger, A procedure for modeling shallow dislocation sources, *Geophys. J. R. Astr. Soc.*, 42, 117-130, 1975.
- LeFevre, L., and D. V. Helmberger, Upper Mantle P Velocity Structure of the Canadian Shield, *J. Geophys. Res.*, 94, 17749-17765, 1989.
- Mauk, F. J., D. Christensen, and S. Henry, The Sharpsburg, Kentucky earthquake, 27 July 1980: Main shock parameters and isoseismal maps, *Seismo. Soc. Am., Bull.*, 72, 221-236, 1982.
- Näbëlek, J. L. Determination of earthquake source parameters from inversion of body waves, *Ph.D. Thesis*, Massachusetts Institute of Technology, Cambridge, Massachusetts, 361, 1984.
- North, R. G., R. J. Wetmiller, J. Adams, F. M. Anglin, H. S. Hasegawa, M. Lamontagne, R. Du Berger, L. Seeber, and J. Armbruster, Preliminary results from the November 25, 1988 Saguenay (Quebec) earthquake, *Seism. Res. Lett.*, 60, 89-93, 1989.
- Pakiser, L. C., and W. D. Mooney, Geophysical framework of the continental United States: Boulder, Colorado, *Geol. Soc. Am., Memoir 172*, 1989.

- Somerville, Paul G., James P. McLaren, Chandan K. Saikia, and Donald V. Helmberger, The 25 November 1988 Saguenay, Quebec, Earthquake: Source Parameters and the Attenuation of Strong Ground Motion, *Bull. Seismol. Soc. Am.*, 80, 1118-1143, 1990.
- Stead, R. J., Finite Differences and a Coupled Analytic Technique with applications to Explosions and Earthquakes, *Ph.D. Thesis*, pp., Caltech, Pasadena, California, 1989.
- Taylor, S. R., Geophysical framework of the Appalachians and adjacent Grenville Province, *Geological Society of Amer.*, Memoir 172, 1989.
- Taylor, S. R., and M. N. Töksoz, Three-dimensional crust and upper-mantle structure of the northeastern United States, *J. Geophys. Res.*, 84, 7627-7644, 1979.
- Taylor, S. R., and M. N. Töksoz, Crust and upper-mantle structure in the Appalachian orogenic belt; Implications for tectonic evolution: *Geological Society of America Bulletin*, 93, 315-329, 1982.
- Wallace, T. C., D. V. Helmberger, and G. R. Mellman, A technique for the inversion of regional data in source parameter studies, *J. Geophys. Res.*, 86, 1679-1685, 1981.
- Zhao, L. S., D. Helmberger, Broadband modeling along a regional shield path, Harvard recording of the Saguenay Earthquake, *Geophysical Journal*, in press, 1991.

Table 1. Source Orientation Estimates for the Saguenay Earthquake

	Strike	Dip	Rake
North et. al (1989)	326°	67°	54°
Carabajal and Barker (1991)	325°	74°	50°
Somerville et al. (1990)	320°	65°	78°
Inversion cmodel	334°	58°	79°
Inversion hspmodel	297°	75°	83°

## Figures

**Figure 1.** Three component seismograms recorded at Pasadena,  $\Delta=438$  km, of the Lee Vining, CA Event (24 October 1990,  $M_o=3.0 \times 10^{23}$  dyne-cm). Note the long period nature of  $S_n$ .

**Figure 2.** Three component seismograms recorded at Harvard,  $\Delta=640$  km, of the Chicoutimi, QB Event (25 November 1988,  $M_o=5.0 \times 10^{24}$  dyne-cm). Note how well the short-period signals rotated into (SH) and (P-SV) systems.

**Figure 3.** Map indicating the events and stations studied in this study. Events are shown by stars and stations by triangles.

**Figure 4.** This figure displays the sensitivity of  $P_{nl}$  to source depth;  $\Delta=1000$  km. Model parameters are given in Helmberger and Engen (1980), namely crust ( $\alpha_1=6.2$ ,  $\beta_1=3.5$ ,  $\rho_1=2.7$ ) and mantle ( $\alpha_2=8.2$ ,  $\beta_2=4.5$ ,  $\rho_2=3.4$ ). The crustal thickness is assumed to be 32 km.

**Figure 5.** Comparison of synthetics and observations for the New Brunswick earthquake. Amplitude given in cm assuming a moment of  $1.6 \times 10^{24}$  dyne-cm proposed by Nabelek (1984).

**Figure 6.** Observed and synthetic  $P_{nl}$  waveforms for the July 27, 1980 Kentucky earthquake,  $M=5.2$ . Peak to peak amplitudes in  $cm \times 10^{-3}$  are indicated above each trace.

**Figure 7.** Comparison of recorded and simulated  $P_{nl}$  for the preferred focal mechanism. Amplitudes are shown in units of  $10^{-3}cm$ .

**Figure 8a.** Depth sensitivity of the IHV synthetics showing the preference for deep origin depths.

**Figure 8b.** Depth sensitivity at BLA.

**Figure 9.** Comparison of broadband observations at IHV, with synthetics, after Zhao and Helmberger (1991).

**Figure 10.** Crustal and upper mantle models considered in this study. Model MPM was the preferred model from the broadband path from Chicoutimi to IHV. Model SPT is the preferred model from Chicoutimi to SCP.

**Figure 11.** Comparison of synthetics with IHV broadband and long period simulations.

**Figure 12.** Upper panel displays geologic structure across the northern portion of the Appalachian Thrust Belt. Note that the path from Chicoutimi to IHV is mostly along the eastern side while the path to SCP is along the western side. Lower panel displays the P-delays across this region, after Taylor and Töksoz (1979).

**Figure 13.** Upper trace displays the observed long-period (GDSN) at SCP. Lower three traces are synthetics for various models; upper (SPT) where  $\alpha_c=6.6$ ,  $\beta_c=3.7$ ,  $h=35$  km,  $\alpha_m=8.5$ ,  $\beta_m=4.7$ ; Middle model with  $\alpha_c=6.6$ ,  $\beta_c=3.7$ ,  $h=35$  km,  $\alpha_m=8.5$ ,  $\beta_m=4.8$ ; lower model with  $\alpha_c=6.6$ ,  $\beta_c=3.6$ ,  $h=35$  km,  $\alpha_m=8.5$ ,  $\beta_m=4.8$  km/sec.

**Figure 14.** Comparison of observations with synthetics for a number of paths.

**Figure 15.** Profile of synthetics for the vertical and tangential components assuming a pure strike-slip orientation and model MPM. Line indicates the  $S_n$  arrival, sharp spikes following  $S_n$  are produced by layering in the lithospheric model.

**Figure 16.** Waveform inversion results assuming the halfspace model (hsp) and model MPM (c). The correlation constants are (0.82, 0.93, 0.74) for c and (0.86, 0.78, 0.83) for hsp.

**Figure 17.** Comparison of data against synthetics for various proposed models. The correlation constants are Somerville (1990) 0.82, 0.93, 0.73; Carabajal and Barker (1991) 0.27, 0.71, 0.43; and North et al. (1989) 0.70, 0.84, 0.55.

**Figure 18.** Comparison of whole synthetics predicted from the bodywave inversions with observations. Surface waves are obviously more sensitive to the layered crust (c).

**Figure 19.** Comparison of synthetics containing directivity.

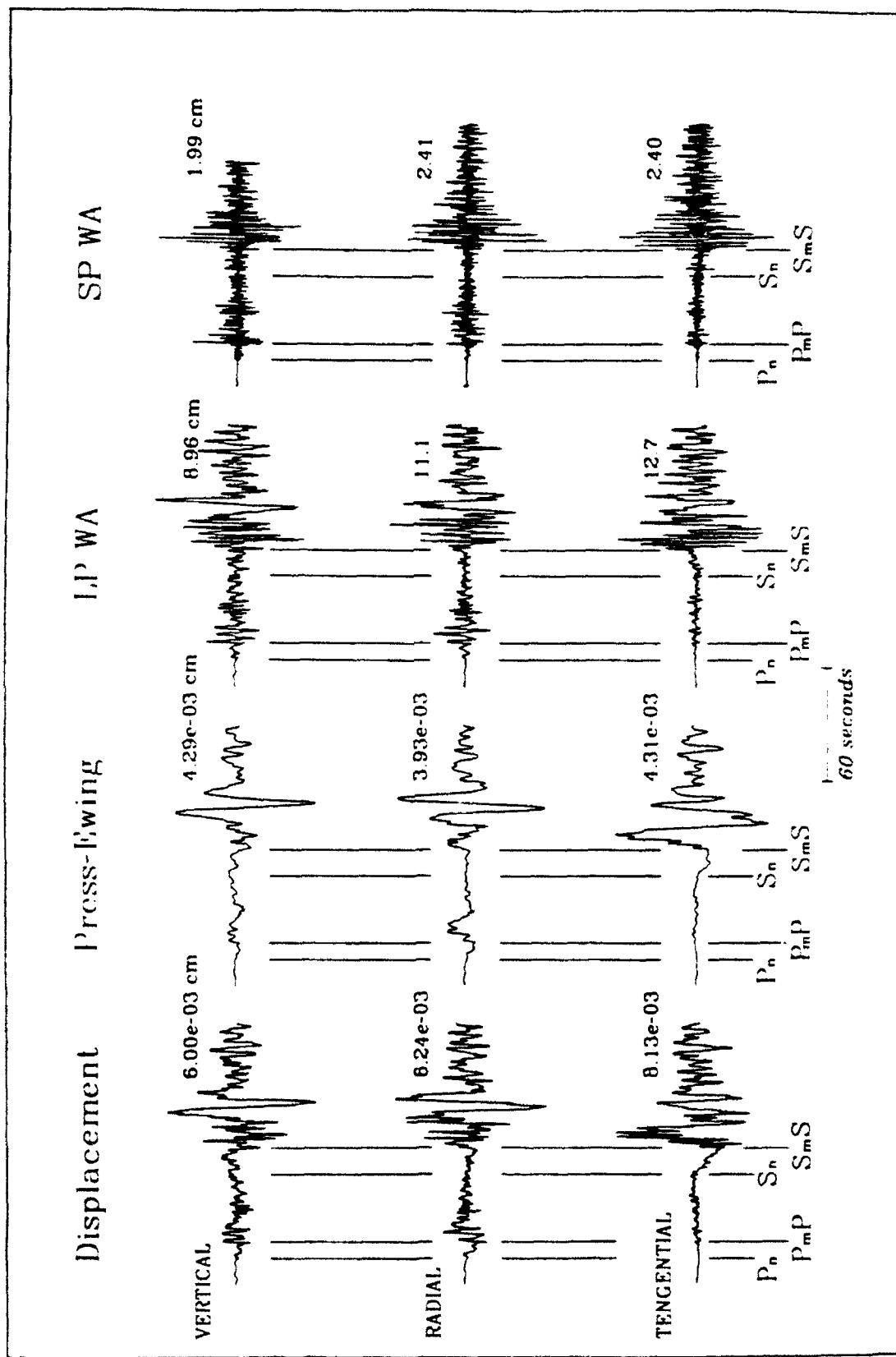


Figure 1



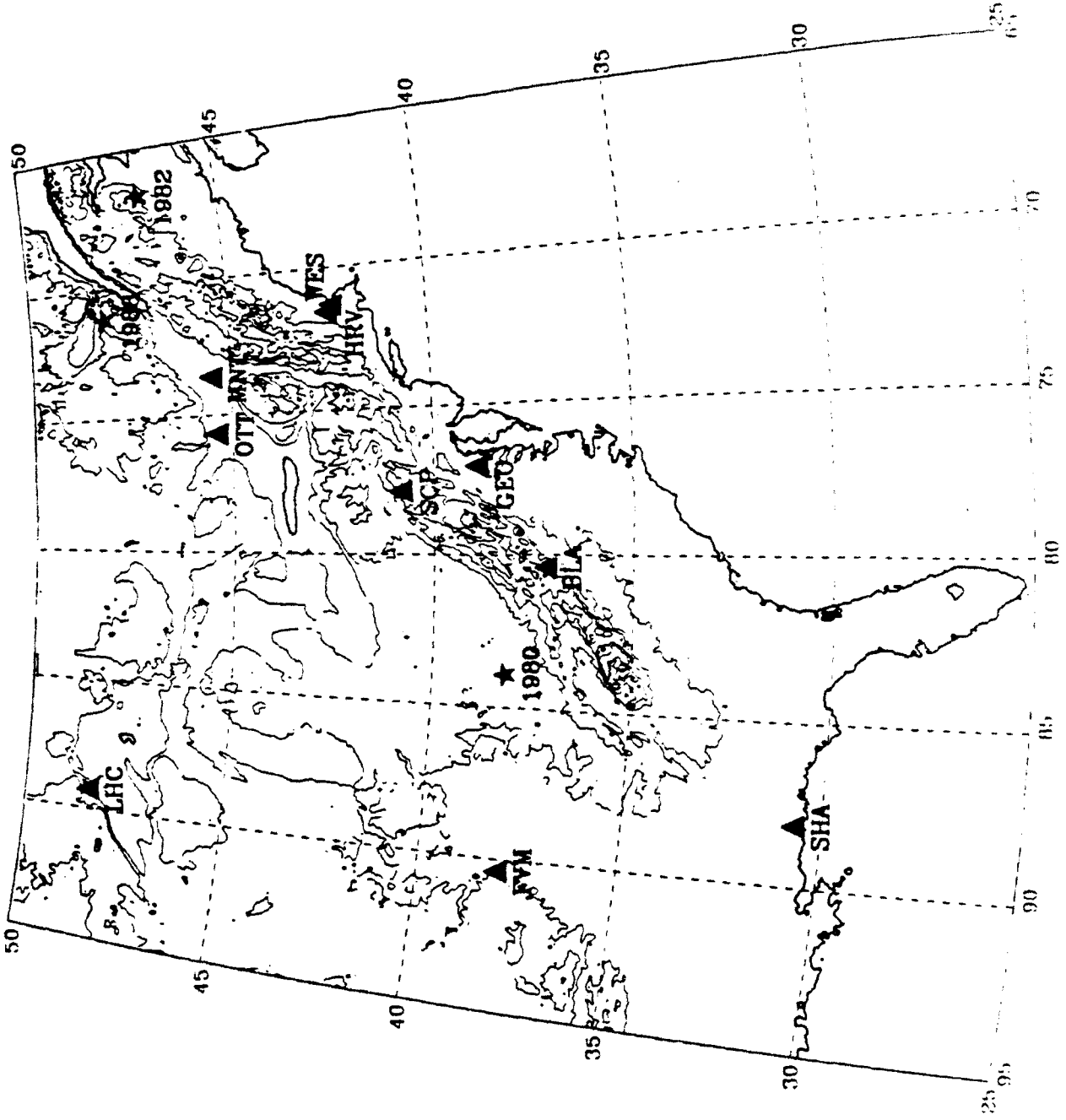
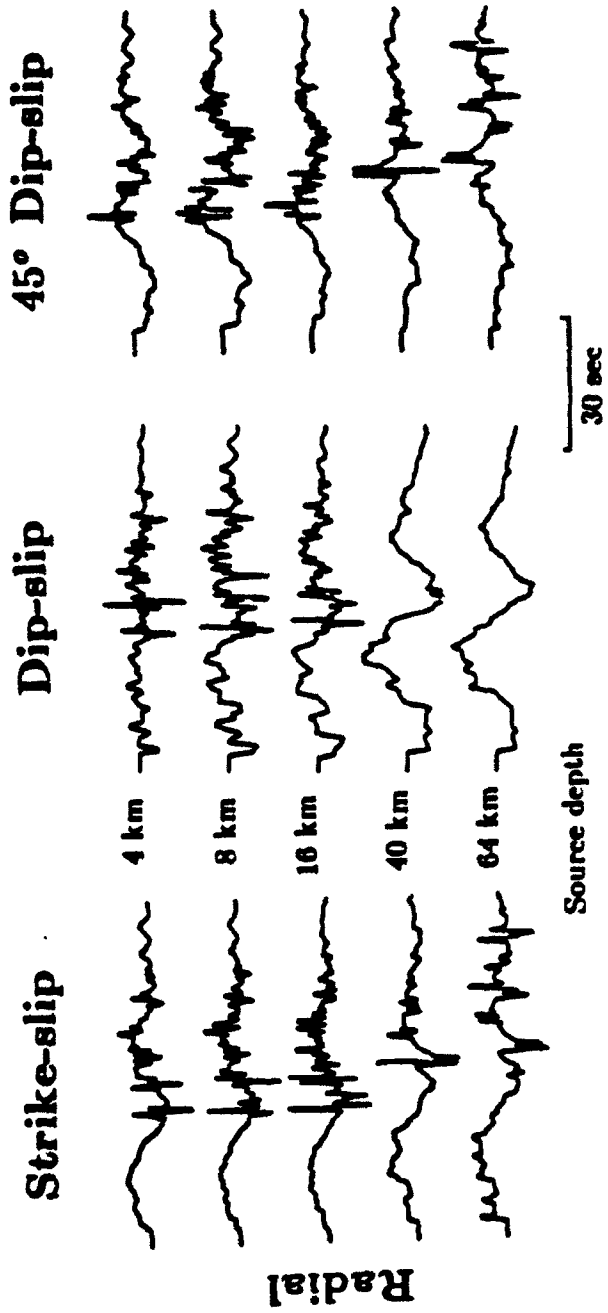


Figure 3



**Figure 4**

New Brunswick  
9 Jan 1982

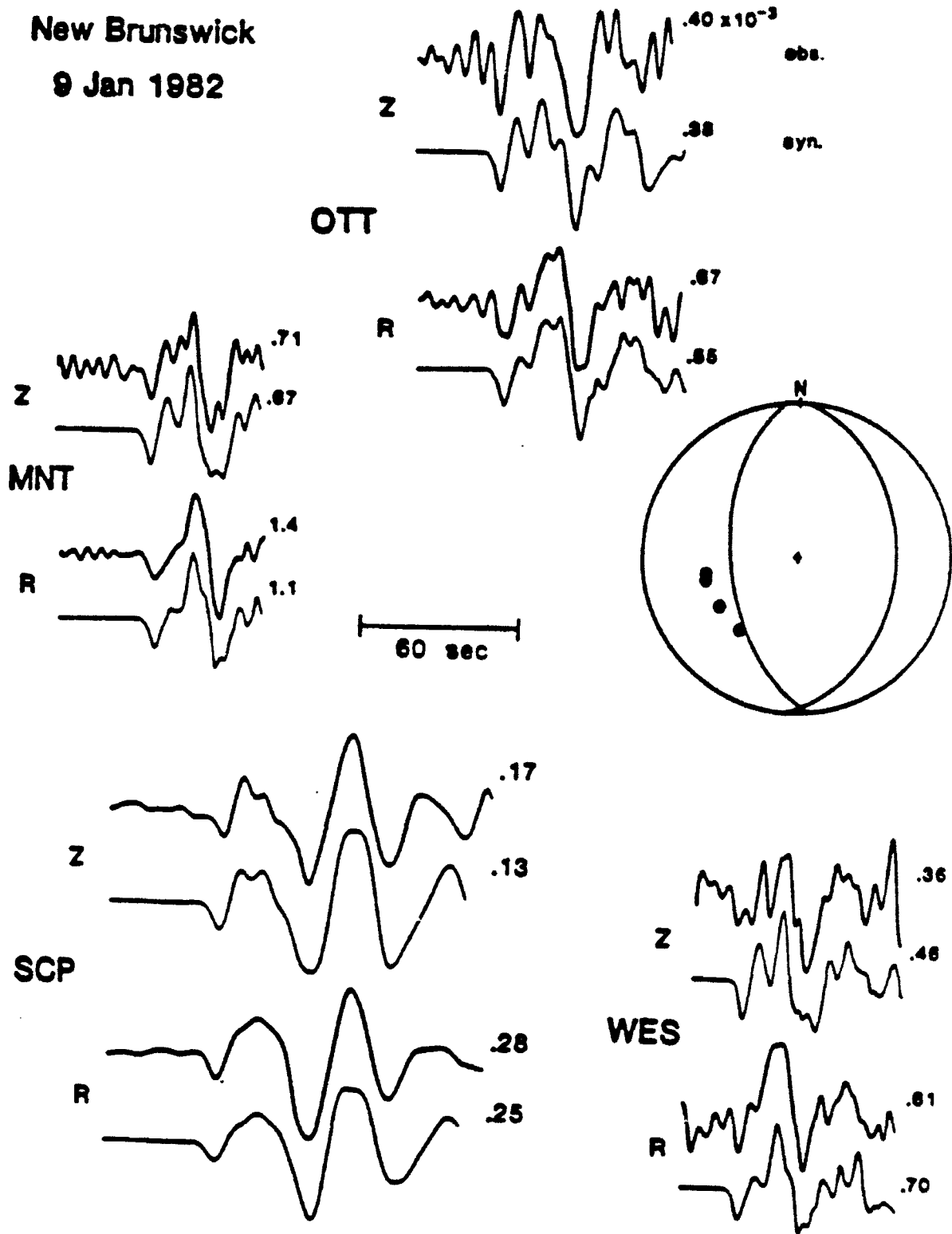


Figure 5

KENTUCKY

27 July 1980

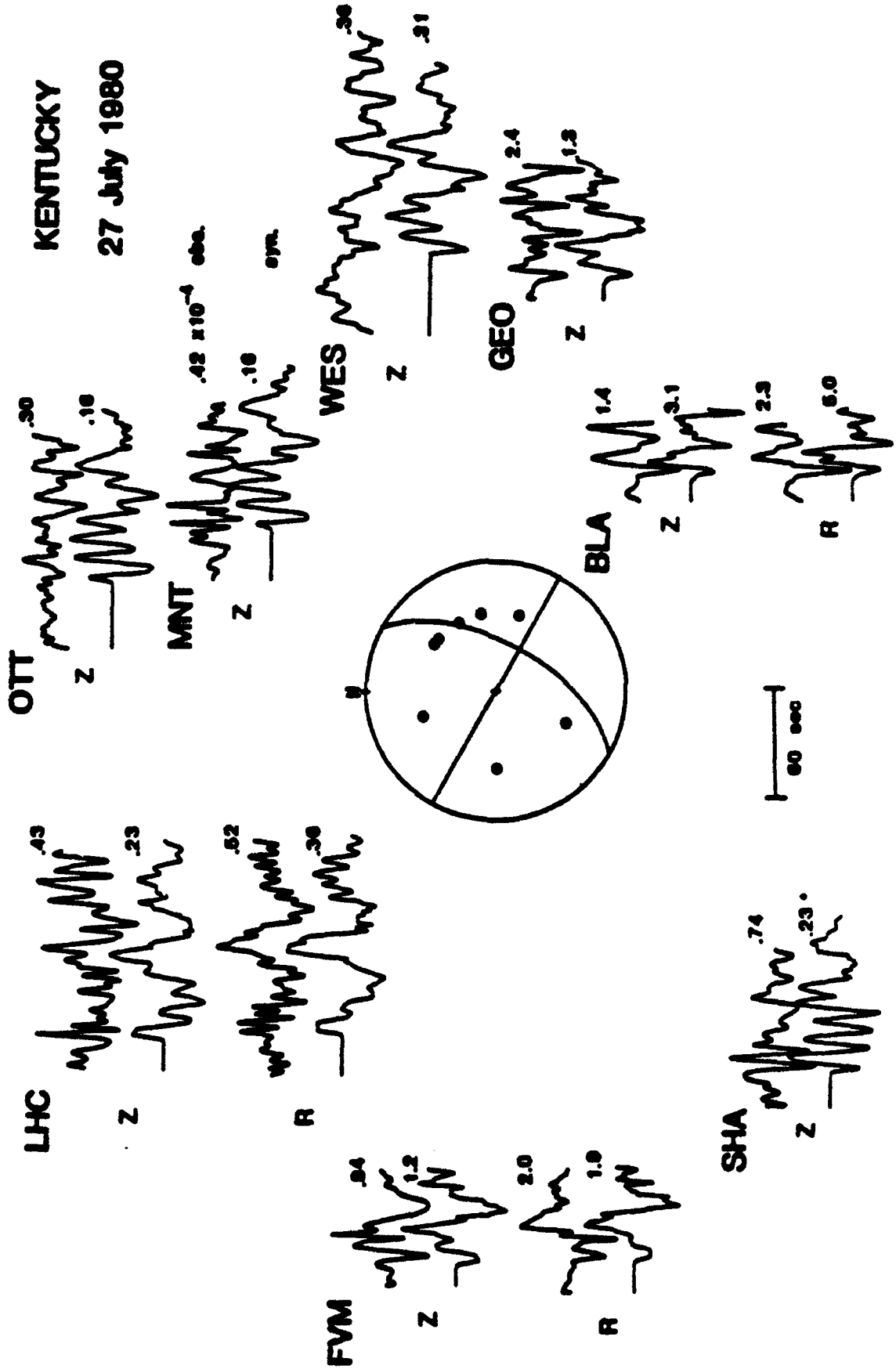
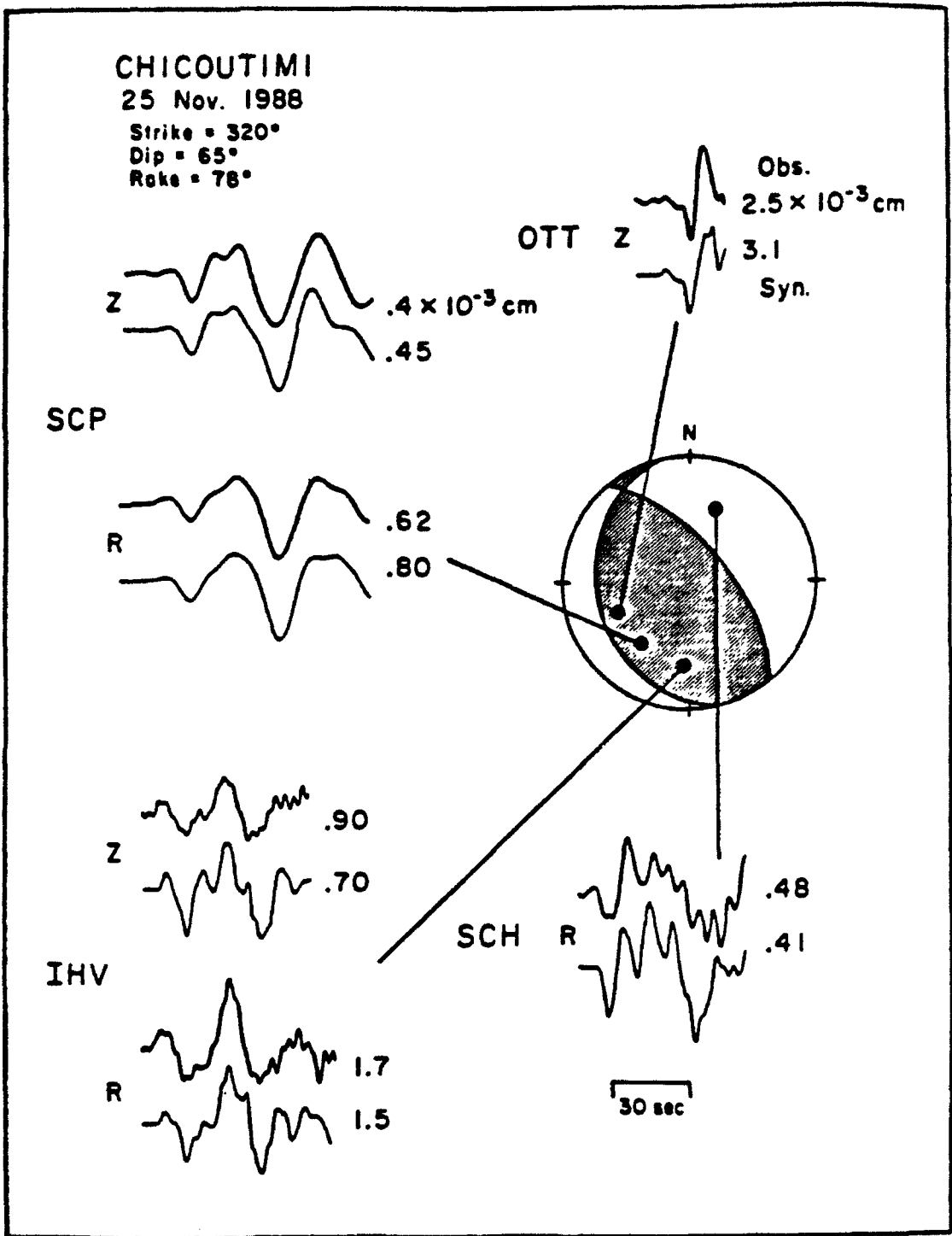


Figure 6



**Figure 7**

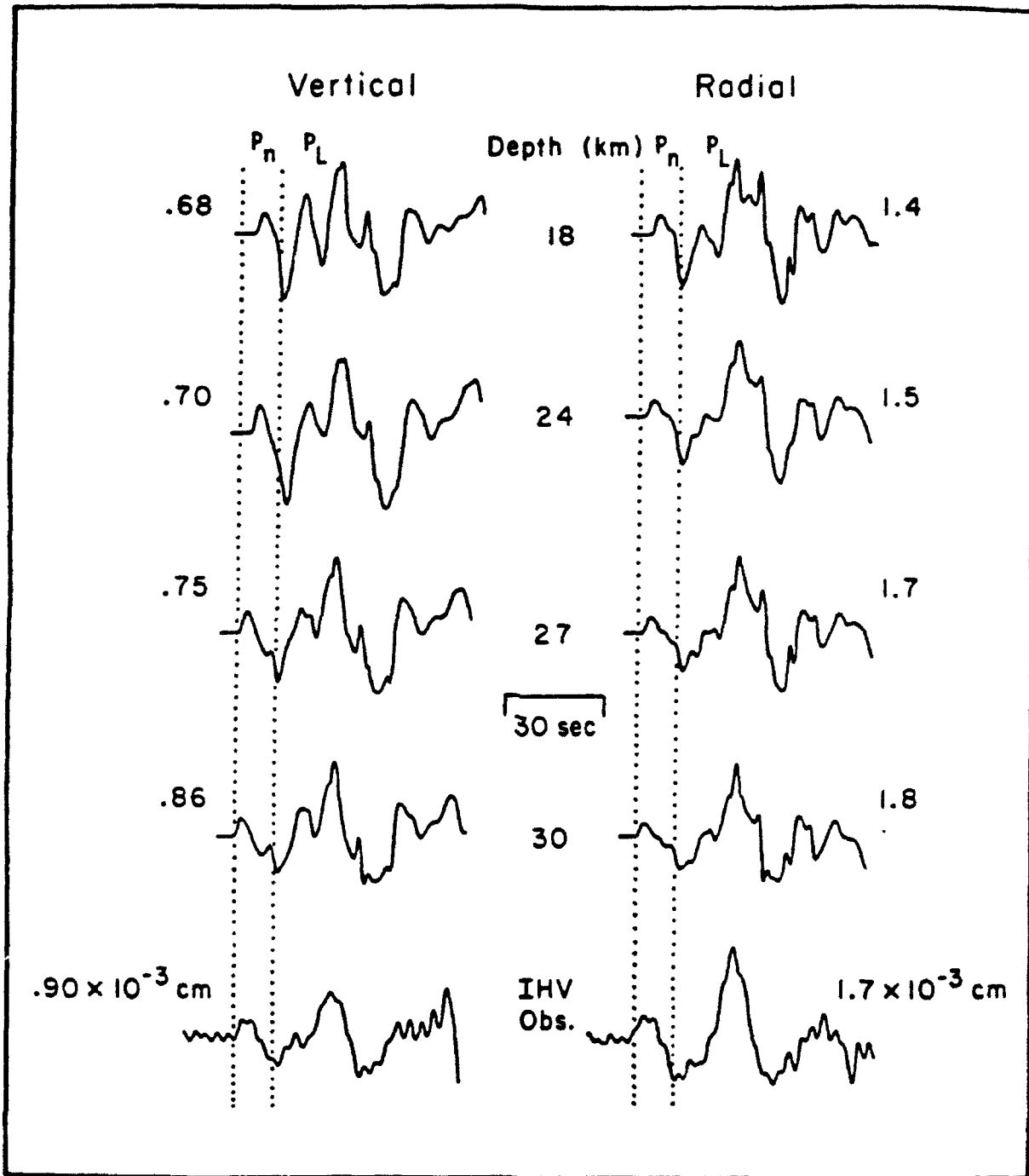


Figure 8a

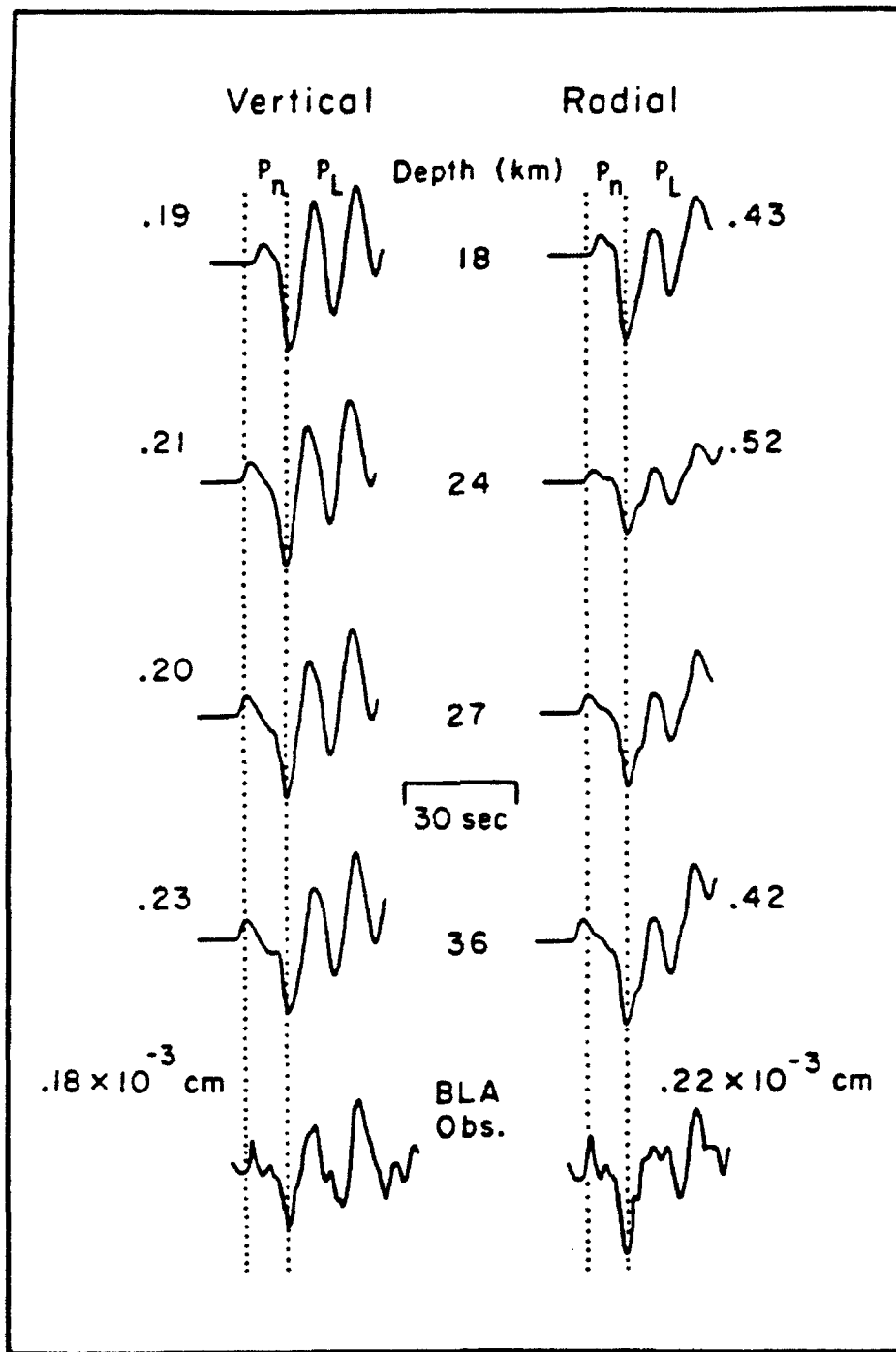
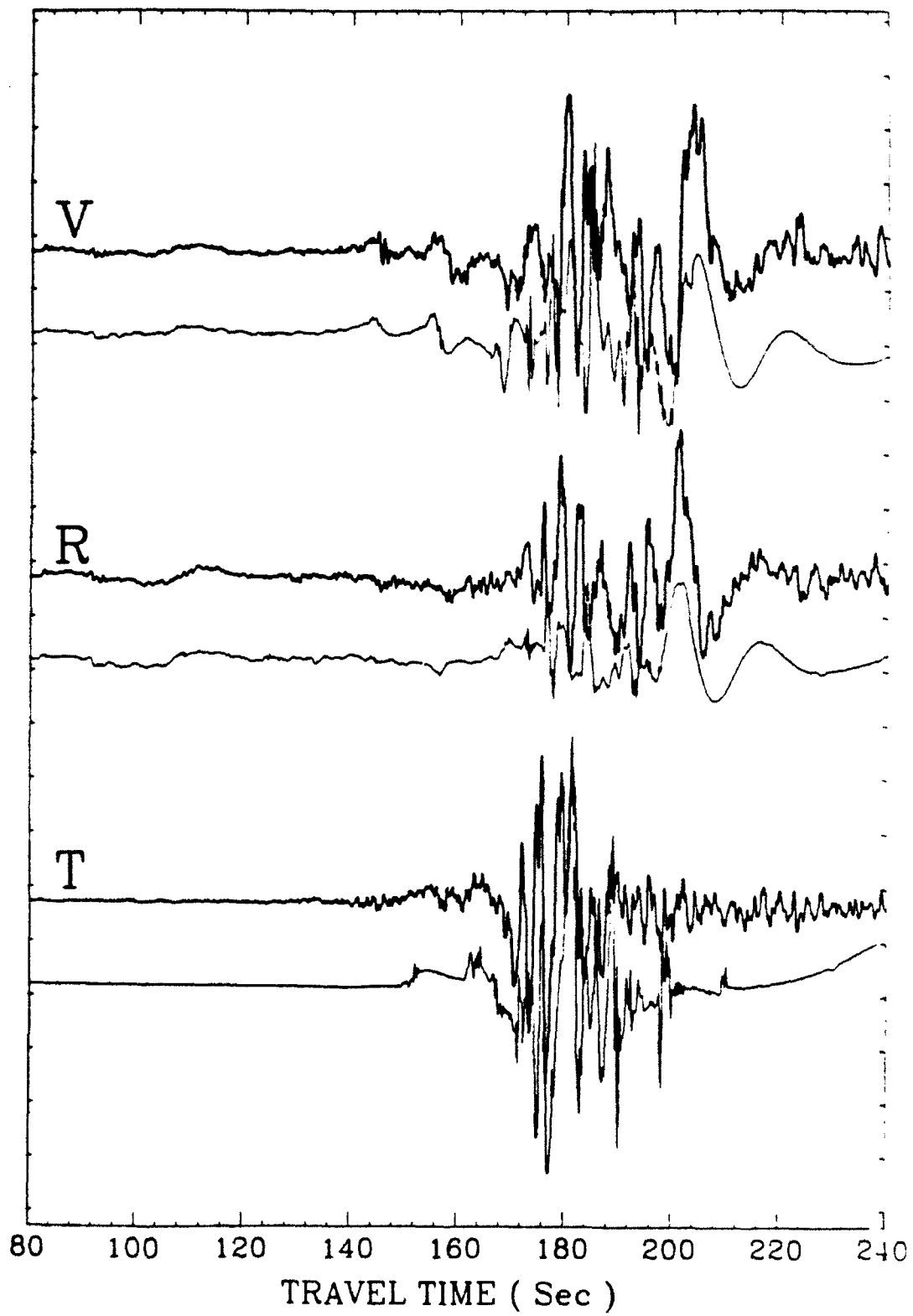
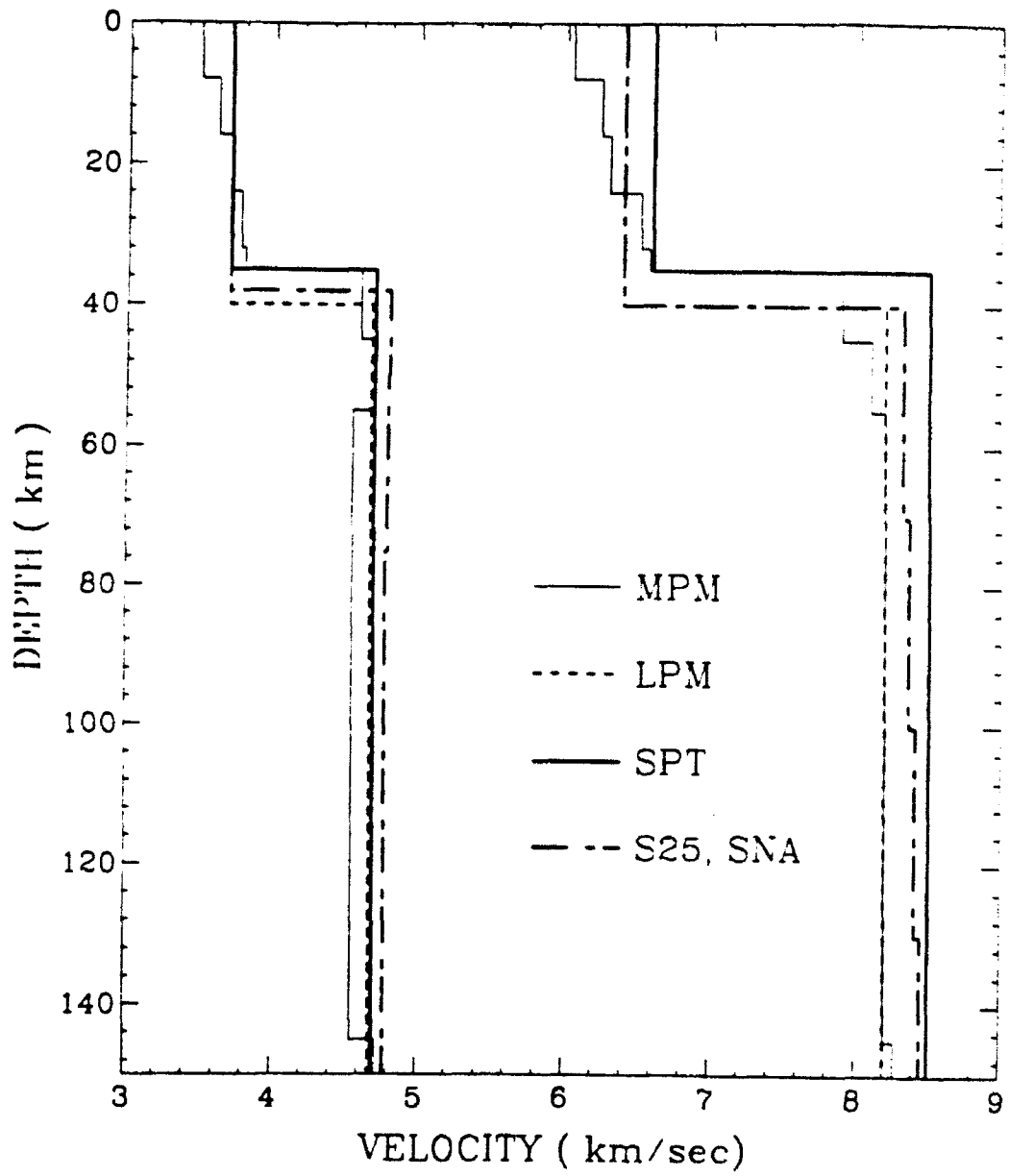


Figure 8b



**Figure 9**



**Figure 10**

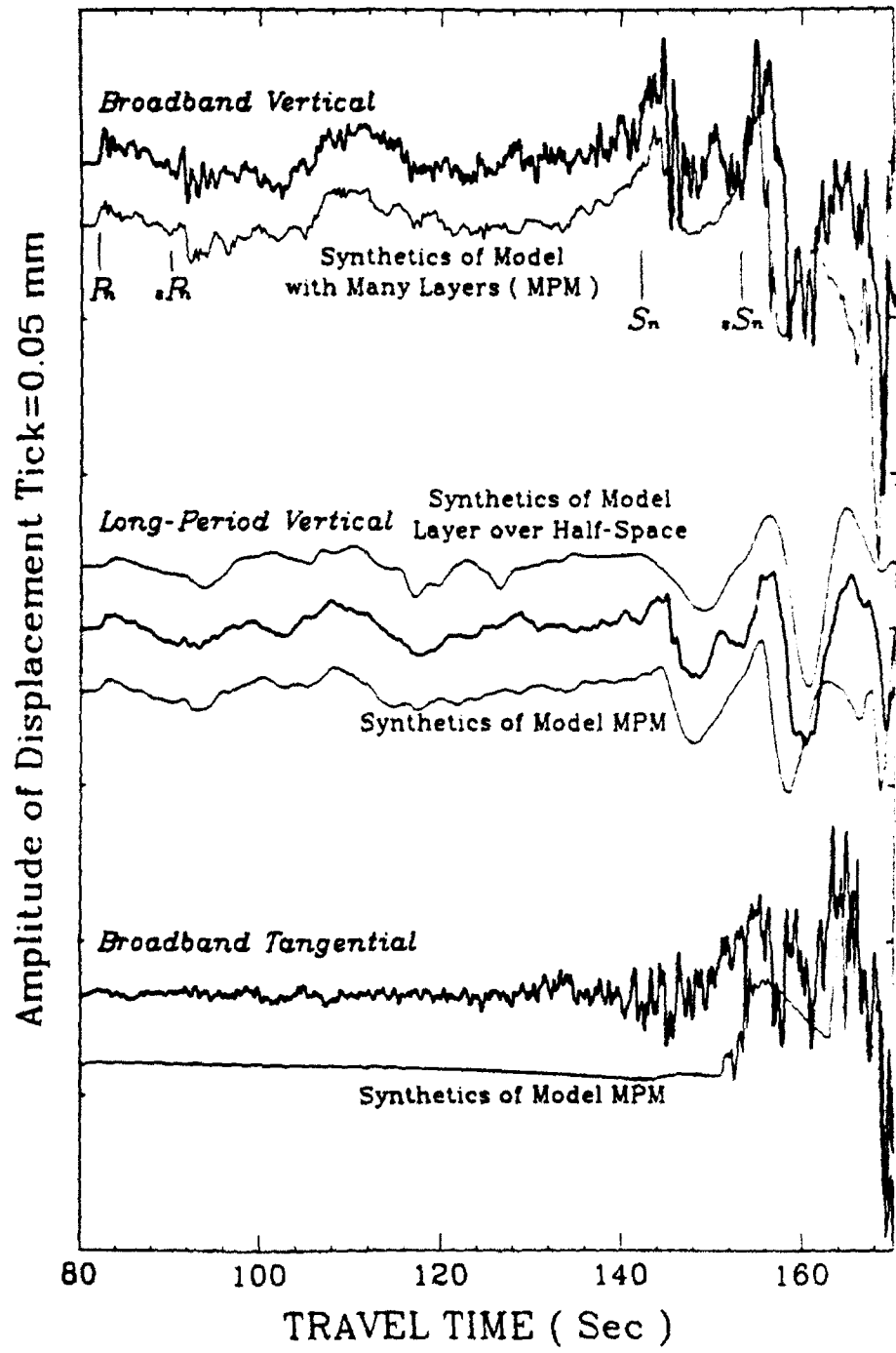


**Figure 11**  
28



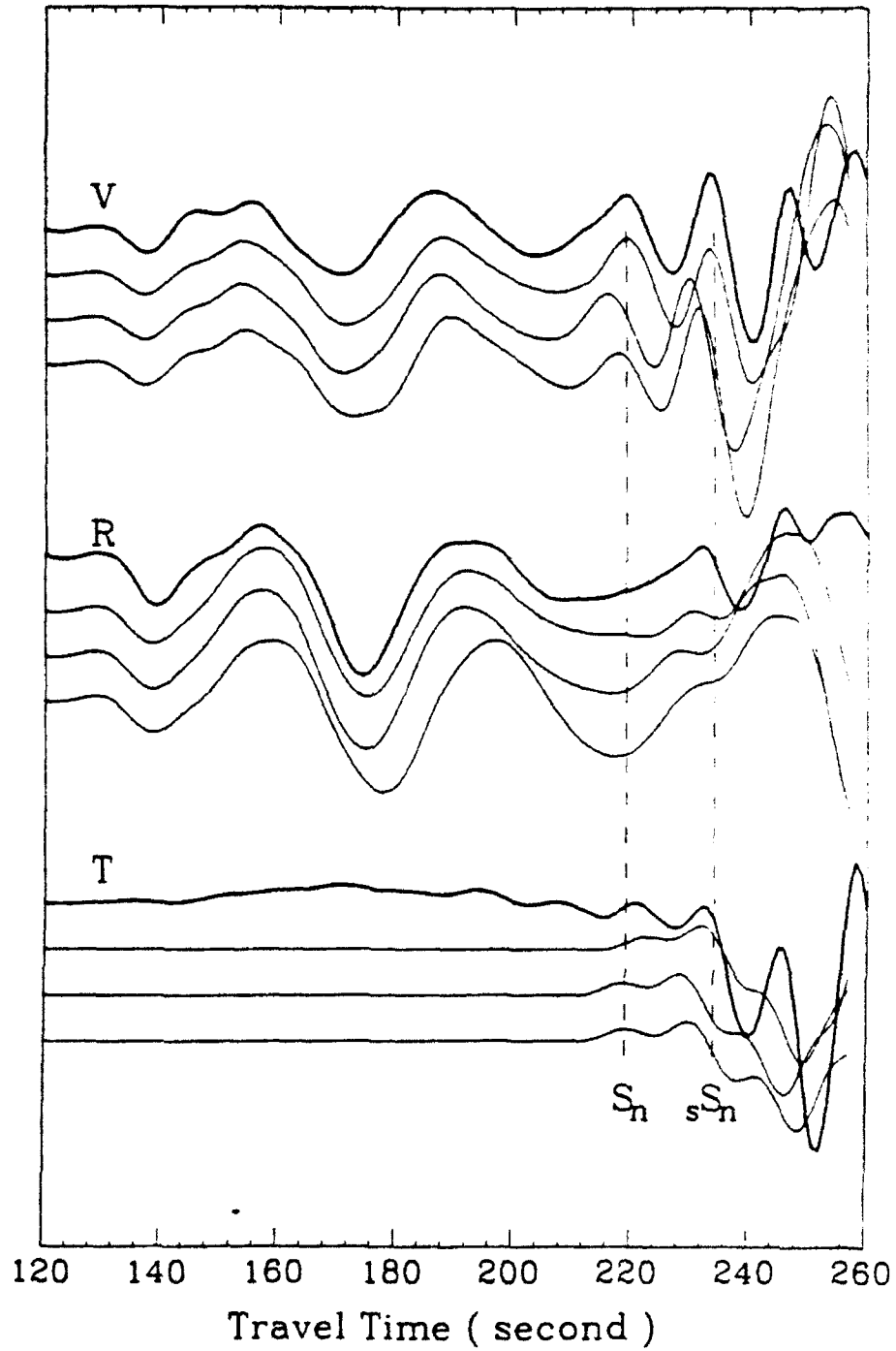


**Figure 13**

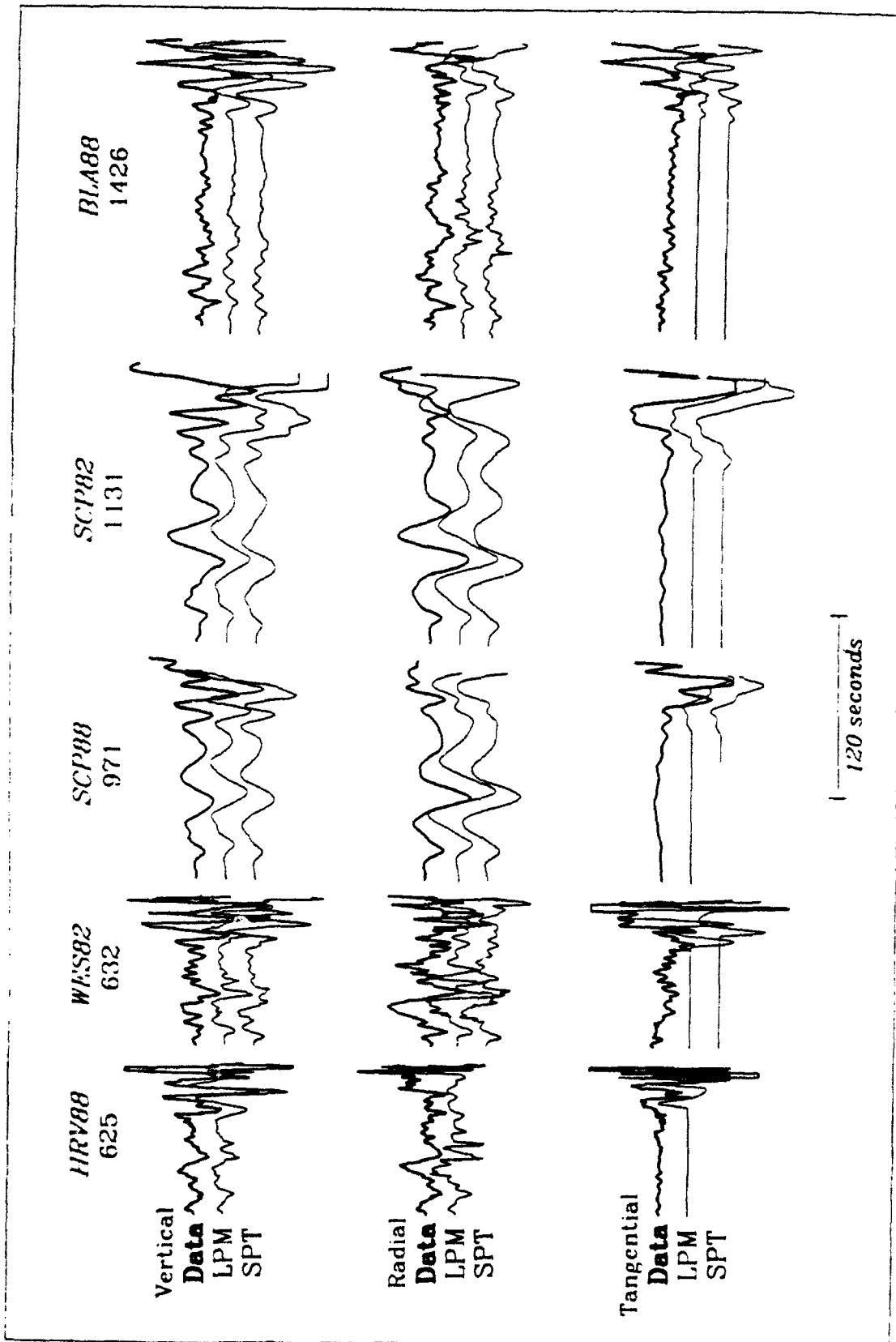


**Figure 14**

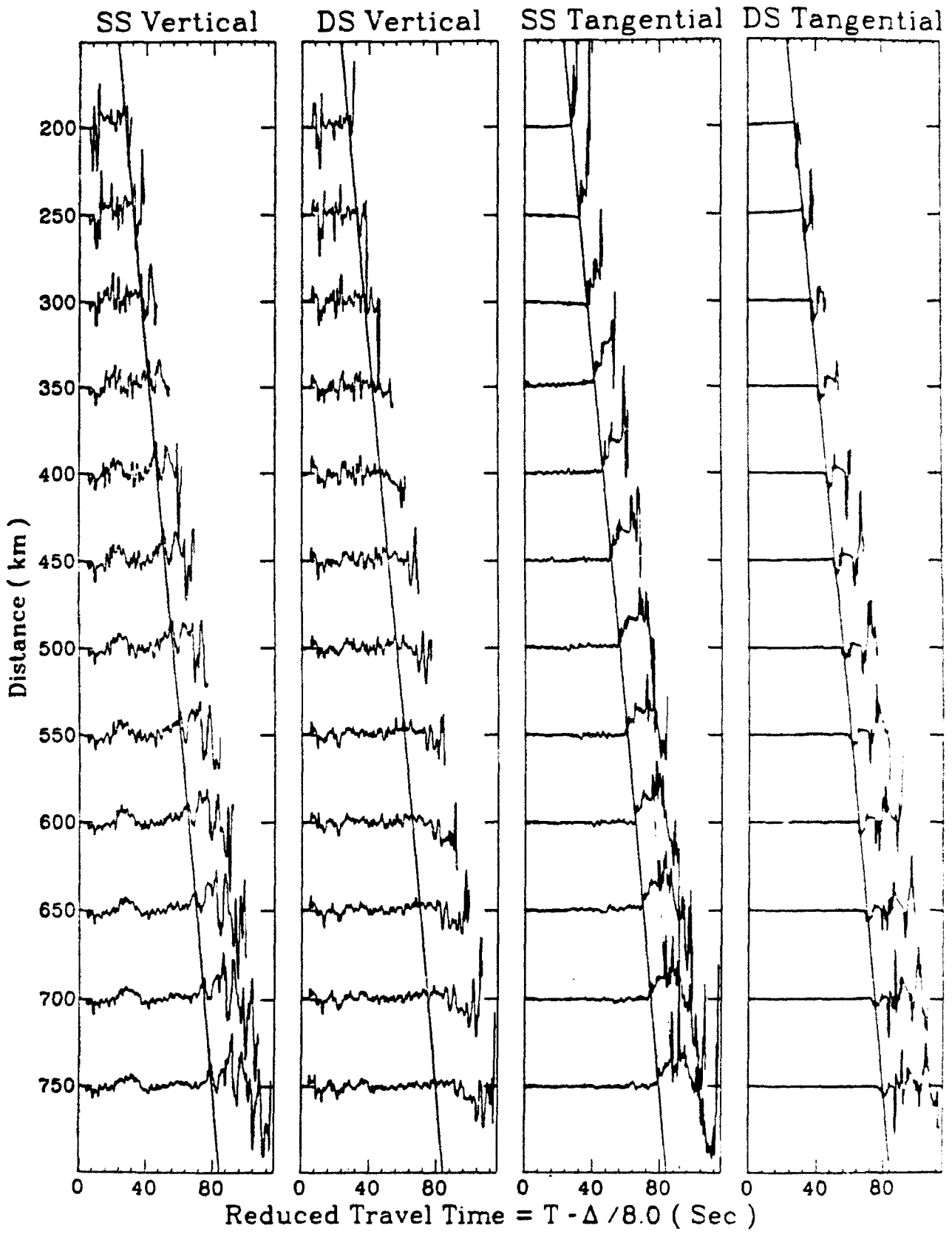


**Figure 15**

Inversion Results Saguenay

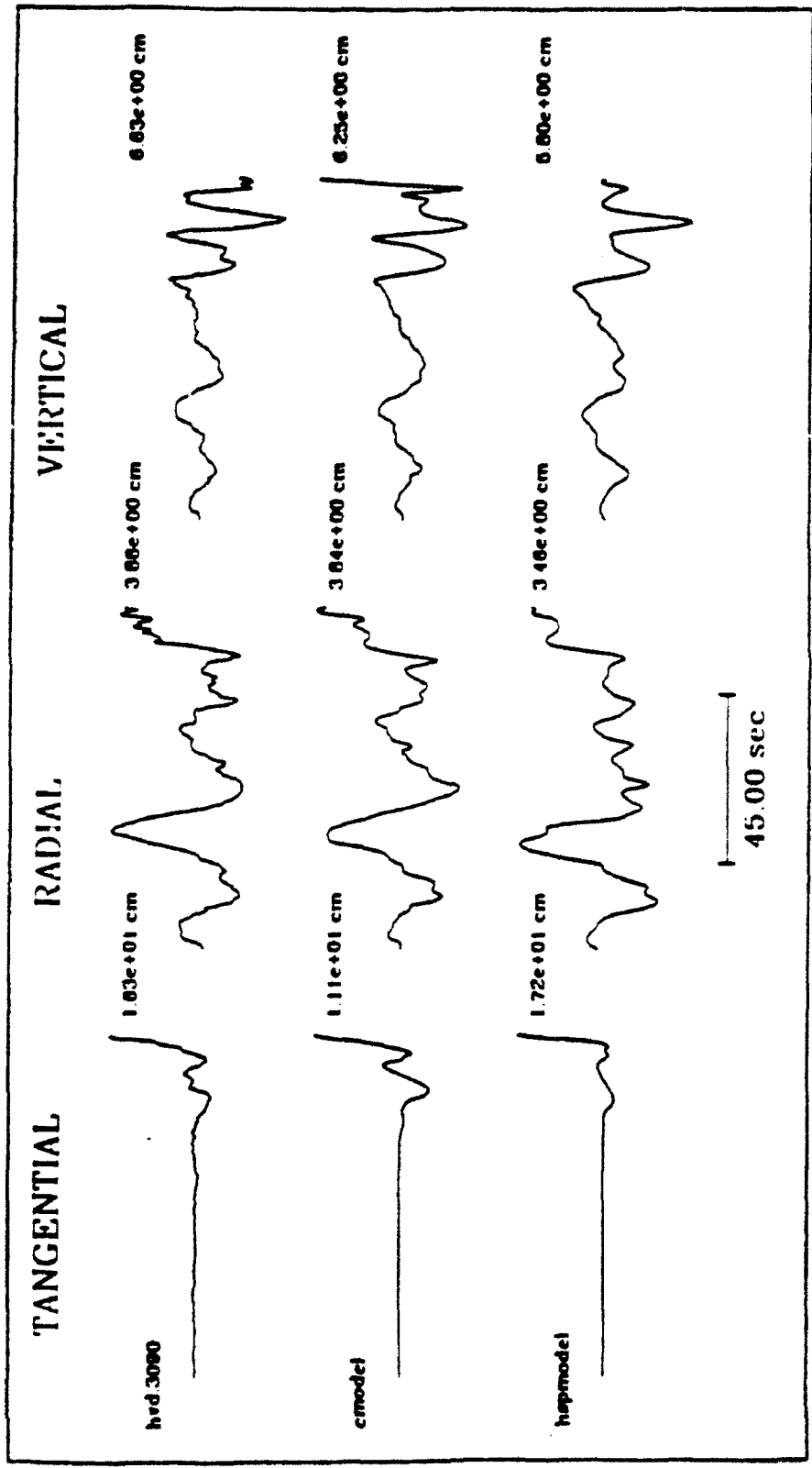


Figure 16

### Comparison of Various Focal Mechanisms

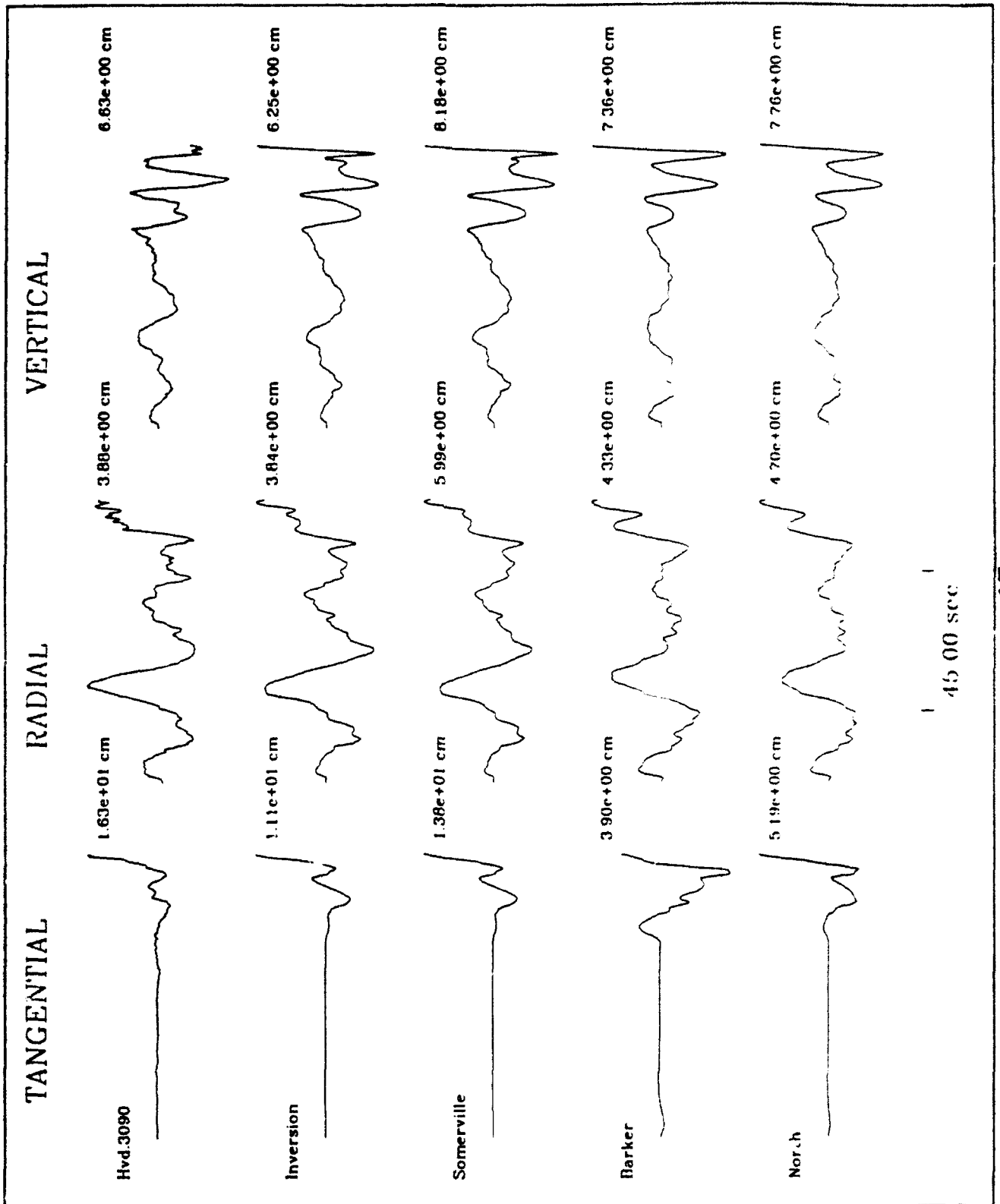


Figure 17

Inversion Results Saguenay

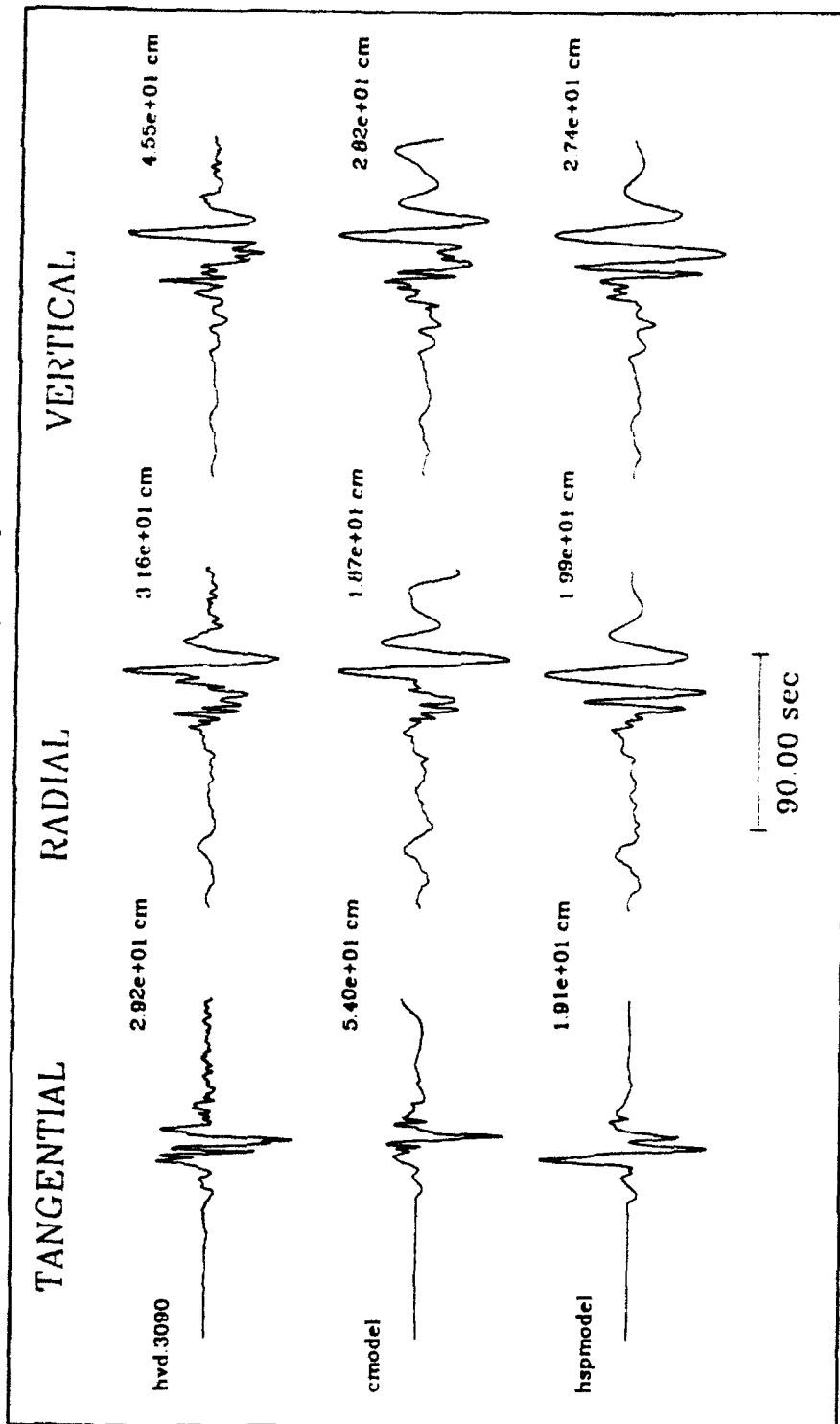


Figure 18

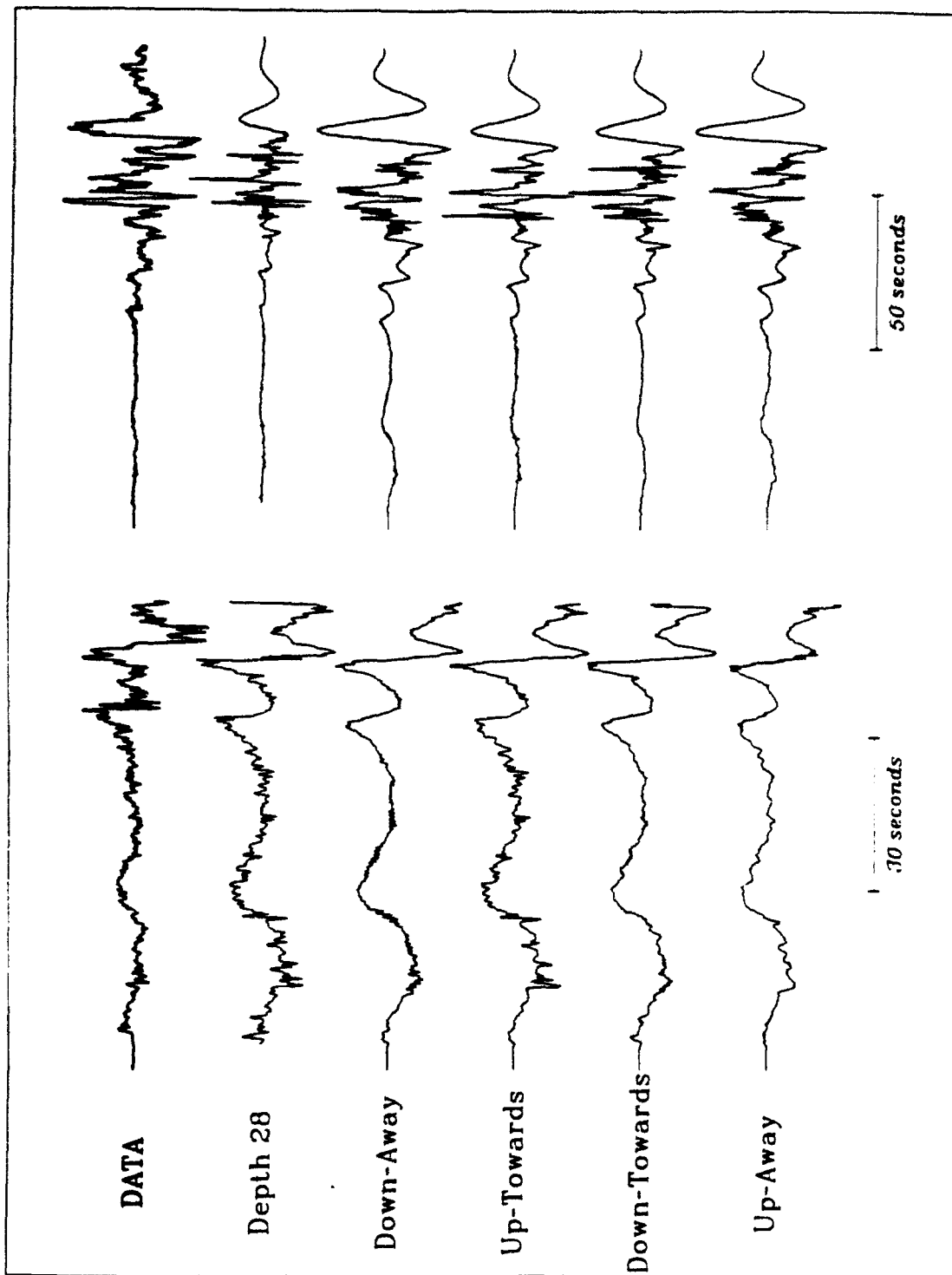


Figure 19

## SECTION 2

Determining Surface Wave Magnitudes from Regional NTS Data

## Determining Surface Wave Magnitudes

### from Regional NTS Data

BRADLEY B. WOODS AND DAVID G. HARKRIDER

*Seismological Laboratory 252-21,*

*California Institute of Technology*

We re-examine the use of surface wave magnitudes as a determination of yield of underground explosions and the associated magnitude-yield scaling relationship. We have calculated surface wave magnitudes for 190 Nevada Test Site (NTS) underground nuclear explosions from a data set of regional long-period seismograms from a combined super-network of 55 North American stations. Great effort went towards making the data set comprehensive and diverse in terms of yield, source location and shot medium in order to determine the portability of surface wave magnitude scales. In particular, we examine Pahute Mesa, Rainier Mesa and Yucca Flat explosions detonated above and below the water table that range in yield over three orders of magnitude. By observation we find a low-yield measure threshold of approximately one kiloton for (assumedly) moderately well-coupled explosions recorded at near regional ( $< 500$  km), seismically "reasonably quiet" stations. In order to utilize the nearer regional stations ( $\Delta < 20^\circ$ ), we have developed several related methods for determining time domain surface wave magnitudes or scalar moments from regional Rayleigh waves, thus enhancing the utility of surface wave information for seismic event magnitude quantifying and discrimination purposes. One technique employs synthetic seismograms to establish a relationship between the amplitude of the regional Airy phase, or Rayleigh pulse of the Rayleigh wave-train and an associated surface wave magnitude, based on conventional  $M_s$  determinations, calculated from a synthetic seismogram propagated to  $40^\circ$ . The

other method uses synthetic seismograms in a similar fashion, but the relationship used is a more straight forward one between scalar moment and peak Rayleigh wave amplitude. Path corrections are readily implemented to both methods. The inclusion of path corrections decreases the  $M_s$  variance by a factor of two and affects the absolute scaling relationship by up to a factor of 0.1 magnitude units. This latter effect is attributed to the particular station network used and the Green's function used to obtain the  $40^\circ M_s$  values. Using a generic structure for the distance traveled past the actual source receiver path minimizes the difference between magnitudes determined with and without path corrections. The method gives stable  $M_s$  values that correlate well with other magnitude scale values over a range of three orders of magnitude in source yield. Our most refined  $M_s$  values give the relationship  $M_s = 1.00 \times \log(\text{yield}) + B$ , where B is dependent upon source region and shot medium. This yield exponent of unity holds for events of all sizes and is in line with  $M_s$ -yield scaling relations found by other studies. When events are grouped with respect to source region, significantly better fits to these individual site linear regression curves are obtained compared to the fits obtained using a single, all inclusive model. This observation implies that shot site parameters and source structure affect surface wave magnitude measurements, although event yield-site distribution also may be in part responsible.

Since our magnitude values are based on a theoretical continental structure, we regressed our values with more standard teleseismic  $M_s$  values from several other studies. For all comparisons, our  $M_s$  values scaled favorably with the others, however absolute magnitude curves varied by  $\pm 0.5$  magnitude units. These differences are due in part to the choice of  $M_s$  formula used. It is also possibly due to differences in network station distribution between the studies, with this study using more nearer stations, as well as a wider range of station

azimuths.

## INTRODUCTION

We re-examine the use of surface-waves for underground nuclear explosion magnitude determinations, particularly for smaller yield ( $Y < 20\text{Kt}$ ) events. The surface wave magnitude-yield scaling law for such low-yield events, until now, was not known well. Even for larger-yield explosions there is some debate as to the scaling relation between yield and the long-period energy radiation, as well as the relationship between  $M_s$  and  $m_b$ . Evernden and Filson (1971) found that  $M_s = 1.4 + 1.3 \times \log(\text{yield})$  for hard rock sites in North America. Marshall *et al* (1971) found that  $M_s$  scales with yield to the first power, with consolidated rock (tuff, salt, granite, andesite and sandstone) coupling ten times more efficiently than detonations in alluvium. More recently Marshall *et al* (1979) found that for events detonated in hard rock (salt or granite) or below the water table that  $M_s = 2.16 + 0.97 \times \log(Y)$ ; for explosions above the water table,  $M_s = 1.88 + 1.06 \times \log(Y)$ . Taken together these two populations yield the relationship  $M_s = 2.05 + \log(Y)$  (Bache, 1982). Basham and Horner (1973) found the scaling relationship for explosions in consolidated rock at sites throughout the world (a majority of the events being from NTS) to be  $M_s = 1.56 + 1.24 \times \log(Y)$ . Sykes and Cifuentes (1984) found an empirical relationship of  $M_s = 2.16 + 0.95 \times \log(Y)$  for events detonated in different regions of the earth. Murphy (1977) found that the scaling law varied between events larger than 100 Kt ( $M_s = 1.2 + 1.33 \times \log(Y)$ ) and smaller events ( $M_s = 2.14 + 0.84 \times \log(Y)$ ).

The above studies utilized data from a suite of sites to determine yield - magnitude relationships. Doing so is likely to add scatter to the results, for the shot medium, the

source region, and regional propagation effects may all affect surface amplitudes. We subgrouped our data set into specific source region data subsets in order to ascertain whether or not the separated explosion populations have different magnitude scaling relationships.

The data for this study are long-period North American station vertical records for 190 Nevada Test Site (NTS) events. The stations used are from several networks. Their respective instruments all have pass bands that lie within the 10 to 60 second range. Surface waves are very useful for yield estimation purposes, for  $M_s$  is determined from relatively long-period seismic waves which are insensitive to high frequency near-source effects, which may be caused by asymmetries in the shot cavity (Zhao and Harkrider, 1991), as well as by other possible mechanisms. These high frequency source effects may cause appreciable bias in magnitudes that are based on higher frequency waves, such as the  $m_b$  and Lg scales.

Evernden and Filson (1971) suggest, based on their observations of body-wave and surface-wave magnitudes of U.S. underground explosions detonated both within and outside of NTS, that the change in  $M_s - m_b$  relationship from site to site is due to abnormal  $m_b$  values, rather than abnormal  $M_s$  values, and that regional crustal and upper mantle attenuation, *i.e.*  $\Delta t^*$ , variations near the source are responsible for the larger scatter in  $m_b$ -yield correlations.  $M_s$  measurements are also less sensitive to source depth effects than are body wave measured magnitudes (Marshall and Basham, 1972). If it weren't for contamination due to tectonic release, which has a more pronounced effect on long period surface waves than body waves, and lateral inhomogeneity along the surface wave propagation path near the earth's surface, the long-period energy measured from surface waves might be a more stable measure of seismic yield than teleseismic body-wave measurements. It is the purpose of this paper to develop and apply a technique for reducing the contaminating effect of lateral propagation

on  $M_s$  measurements.

Another advantage of using seismic moment or  $M_s$  is that empirical evidence and theoretical studies show that the scaling relationship between  $M_s$  (or log moment) and yield has an approximate slope of unity, i.e.  $M_s = \text{Log}(\text{yield}) + B$ , whereas the  $m_b$ -yield and  $m_b(L_g)$ -yield relationships have slopes between 0.65 and 0.90. As Evernden and Filson (1971) point out, a 0.3 error in  $m_b$  corresponds to a 3-fold error in yield determination, while an equivalent error in  $M_s$  results in only a 2-fold error in the yield estimate. Thus the error in yield estimation is inherently larger when obtained from higher frequency magnitude measurements.

For the lower yield events it becomes necessary to include the data from regional stations ( $\Delta < 25^\circ$ ), for teleseismic surface wave recordings have too low a signal to noise ratio, which makes them unusable. At regional distances surface waves are not well dispersed, having a prominent Airy phase pulse with a period between 6 and 20 seconds (Alewine, 1972), so that it is not possible to measure  $M_s$  conventionally (that is measuring the amplitude of the 20 sec. wave). For North America in general, there is minimum in the group velocity curve near 12 seconds for the fundamental Rayleigh wave (Marshall *et al* , 1979). To make accurate surface wave magnitude measurements, this energy bandwidth ought to be modeled as well as possible, for it represents the predominant signal of the wavetrain.

To measure  $M_s$  we employ a technique whereby theoretical seismograms in conjunction with the surface wave data are employed to indirectly calculate the magnitude. In using this procedure several propagation path models were tested to determine the effect of attenuation and seismic velocity structure upon the  $M_s$  values. These calculated  $M_s$  values remain stable, have reasonably small errors and correlate well with associated  $m_b$  magnitudes and log yield for the event data set. The  $M_s - m_b$  relationships are determined by a weighted least-squares

linear regression; both free and fixed slope curves were fit to the data.

We also determine time-domain moment measurements from the same data. The moment is determined from the ratio of the maximum peak to peak amplitude of the surface wave train to that of a synthetic, with a given input step moment, propagated to the same distance as the data. These two time domain magnitude measurements give very similar results.

Besides comparing the  $M_s$  results with several different independent magnitude scales, the data have also been separated with respect to source region and shot material.  $M_s$  values at Yucca Flat tend to be larger than those at Rainer Mesa by 0.08 magnitude units for a given  $m_b$ . There also appears to be some difference in waveforms between events of these two source regions. Pahute Mesa events are 0.39 magnitude units larger than those at Yucca flat for explosions set-off below the water table and with the same  $m_b$ .

No corrections were made in magnitude for shot medium coupling effects, although such affects can be considerable, even for long-period energy (Werth and Herbst, 1963), because such shot-site information would not necessarily be available for events detonated in other countries. This study is meant to test the effectiveness and portability of a surface-wave magnitude scale in the most general case.

We do not account for tectonic release effects upon the magnitude measurements. Such effects are best accounted for with moment tensor inversions of sources which involves more sophisticated data analysis. Standard  $M_s$  measurement techniques ignore this factor as well. The effects of tectonic release are considered in a sequel paper.

## DATA

The data are long-period vertical seismograms recorded at North America stations for 190 explosions at NTS and consist of digitized World Wide Seismic Network (WWSN)

and Canadian Seismographic Network (CSN) records, Digital World Wide Seismic Network (DWWSN), Lawrence Livermore Regional Seismic Network (LNN) and Regional Test Seismic Network (RSTN) digital data. The analog WWSN and Canadian station data were digitized by ENSCO Inc. Fifty-eight stations comprise the network, although fewer than 60 percent of the stations had data available for any single event. Fig. 1 shows a map of the station network. Epicentral distances range from 220 km for NTS to GSC (Goldstone, California), to 4350 km for NTS to MBC (Mould Bay, Northwest Territories). For the smaller events, particularly Rainer Mesa explosions, only the nearer stations (distance < 1000 km) had either data available or reasonable signal to noise ratios. Station coverage varies widely between events. Twenty-two of the smaller events (or very early events) only had one viable station seismogram each, while some events had over 30. The average number of stations reporting per event is approximately ten. For current and future geographical areas of monitoring interest it is reasonable to assume that only sparse networks will be able to record any given event, particularly explosions below 10 Kt and as well those explosions that are intentionally "muffled" to evade detection. So it is important to see how well an explosion magnitude can be estimated with only one to five observations.

Because our methods for determining magnitudes are done by means of time domain measurements, analog records can be readily used as well. We took advantage of this fact to acquire several events (72 of the 190) to add to our sample population. The events were chosen with a mind to filling-out the data set with respect to yield, depth to water table and geographic location.

Surface waves that propagate across oceanic-continental margins undergo significant modification in their waveforms because of the great lateral variation in crustal and upper mantle

structure at such boundaries. These propagation effects are not straight forward to model, hence meaningful Green's functions, or transfer functions, are difficult to obtain. Without robust Green's functions it is hard to infer accurate source information from the data. Smaller events also are not likely to be observed at the distant stations, which often include oceanic structure along their propagation path, and make these longer paths even less attractive to include in the monitoring network. Hence, we chose to confine our study to surface waves traveling solely along continental paths, *i.e.* within North America.

Of the 190 events, 48 are from Pahute Mesa, 30 are from Rainer Mesa, 105 from Yucca Flat and seven others from other sites in or around NTS, but outside of the three major test sites. Of these seven events, Piledriver (detonated at Climax stock) was the only one for which we had digital data.

For some specific stations, waveforms varied somewhat between events, depending upon source location. The Piledriver data from a given station look appreciably different from that of any other events recorded at that same station. This was true for every station recording Piledriver and probably is caused by differences in the source region for this explosion. Piledriver was detonated in a granitic source region, north of the other sites. The source to receiver geometries for this event are approximately the same as those as the other NTS events, so the difference in waveforms doesn't appear to be attributable to dispersive effects caused by differences in propagation path length. Piledriver was the only Climax Stock event with readily available data, so no further examination of this site was carried out.

At some of the nearer regional stations (distance  $< 9^\circ$ ), there are also subtle differences between the Yucca Flat and Rainer Mesa event waveforms. At DUG (Dugway, Utah), for example, the Rainer event waveforms look as if the Airy phase has been Hilbert transformed

(equivalent to a  $90^\circ$  phase shift) relative to the Yucca Flat waveforms. The DUG Rainer waveforms also contain more high frequency coda energy than those from Yucca Flat. Pahute events are similar in waveform to Rainier events and have less high frequency content than Yucca events.

Fig. 2 shows representative observed seismograms at each station for several NTS events. More than one event was used since no one event was observed at every station. The darker traces are the observations and the lighter trace below each is a synthetic seismogram made with the fundamental mode Rayleigh wave only. The seismograms were band-passed filtered between 10 and 100 seconds to suppress the long period and short period noise which would otherwise affect the peak to peak measurement of the Rayleigh pulse. The absolute amplitudes of the observed digital data were verified by choosing several different stations and comparing the peak to peak amplitude of the digitized record to that measured directly from the respective analog WWSSN film chip. From this step we ascertained that the station gain factor had been correctly factored out of the seismograms.

#### MAGNITUDE CALCULATION TECHNIQUE

We have developed a method to measure surface magnitudes indirectly. Because a large portion of the data for low yield events is from stations recording at regional distances ( $\Delta < 25^\circ$ ), it is not possible to calculate  $M_s$  conventionally, for the Rayleigh wave is pulse-like which precludes measuring a well dispersed 20 sec. phase (Alwine, 1972). We address this problem with the use of synthetic seismograms of the fundamental Rayleigh wave using an asymptotic relation for mixed path surface waves.

For our mixed path expressions, we follow Levshin (1985) and write the spectral Rayleigh wave vertical displacement for approximate propagation in a slowly varying laterally inho-

homogeneous media (e.g. Burridge & Veinberg, 1977, Babich *et al*, 1976, Woodhouse, 1974, and Yomogida, 1985) as

$$w_0 = \frac{\exp(-i3\pi/4)}{\sqrt{8\pi\omega}} \frac{\exp\left[-i\omega \int_{P_0}^P ds/c\right]}{\sqrt{|J|}_P} \exp\left[-\int_{P_0}^P \gamma ds\right] \left[\frac{1}{\sqrt{UI}}\right]_P \left[\frac{W}{\sqrt{UI}c}\right]_{P_0} \quad (1)$$

where the energy integral is

$$I = \int_0^\infty \rho(z)[y_1^2 + y_3^2]dz, \quad (2)$$

$\rho(z)$  is the local density distribution in the medium and we have used Saito's (1967) Rayleigh wave eigenfunction notation,  $y_i(z)$ . The eigenfunctions are normalized in such away that the vertical displacement eigenfunction,  $y_1(z)$  is equal to 1 at the free surface,  $z = 0$ . This results in the horizontal displacement eigenfunction,  $y_3(z)$ , being equal to the Rayleigh mode surface ellipticity at this boundary.  $U$  and  $c$  are respectively the local group and phase velocities. By *local* we mean the eigenvalues and eigenfunctions that one would obtain for a laterally homogeneous half-space consisting of the vertical elastic and density distribution at that location.  $P$  is the receiver location and  $P_0$  is the point source location and quantities within the  $P$  or  $P_0$  subscripted square brackets are evaluated at these locations. The integrals are taken along the ray path between the two surface locations.  $J$  describes the geometrical spreading of the surface wave energy.  $\gamma$  is the frequency dependent attenuation coefficient due to the anelastic structure of the path. The above expression is applicable in the absence of foci or shadow zones in the vicinity of the receiver. If there are foci along the path an additional phase factor of  $\exp(i\pi/2)$  should be included for each foci. For an explosion,  $W$  is

$$W = M(\omega) \left[ \frac{dy_1}{dz} - \frac{\omega}{c} y_3 \right] \quad (3)$$

where  $M(\omega)$  is the isotropic or explosion spectral seismic moment. We also assume a step

for our explosion history, ie.  $M(\omega) = M_0/(i\omega)$ .

Since we will assume that the directions of the horizontal gradients of the material properties are approximately aligned in the direction of the source to receiver, the ray path is a straight line and  $J = r$ , which is the distance between the two locations. We further assume that the lateral inhomogeneity can be considered to be made up of  $n$  homogeneous segments of radius  $r_i$ , ie.  $\sum r_j = r$ . For comparison with Stevens(1986), who used a similar expression to estimate seismic moments for explosions, and earlier works on which his expressions were based (eg. Bache *et al* 1976 and Harkrider 1981), we write  $W$  in terms of  $K$  where

$$K = y_3(z) - \frac{c}{2\mu\omega} y_2(z) \quad (4)$$

and  $y_2$  is the normalized vertical normal stress eigenfunction. The relation between  $K$  and  $W$  is obtained by substituting

$$\frac{dy_1}{dz} = \frac{1}{(\lambda + 2\mu)} \left[ y_2 + \frac{\omega}{c} \lambda y_3 \right] \quad (5)$$

into the previous  $W$  expression.

Now we can write the multipath displacement as

$$w_0 = -\frac{\exp(-i3\pi/4) \beta_1^2 M_0 \exp[-i\omega(r_j/c_j)]}{\sqrt{2\pi\omega} \alpha_1^2 c_1} \exp(-\gamma_j r_j) \left[ \frac{1}{\sqrt{UI}} \right]_n \left[ \frac{K}{\sqrt{UI}c} \right]_1 \quad (6)$$

where the summation convention of repeated subscripts is used. The 1 subscript denotes the local quantities for the source medium and the  $n$  subscript the local quantities at the receiver. The shear velocity is denoted by  $\beta$  and the compressional velocity by  $\alpha$ . For a given moment,  $M_0$ , the ratio of the square of these two quantities plays a key role in determining the amplitude effect of various shot media. To this order of approximation the spectral amplitude neglecting attenuation is only dependent on the local properties at the source and receiver. The attenuation and phase are dependent on the local properties along the whole

path.

With the substitution

$$\mathbf{A} = \frac{1}{2cUI} \quad (7)$$

(Harkrider & Anderson, 1966, Harkrider, 1981) and multiplying by  $-\sqrt{c_n/c_1}$ , we obtain the same expression as used by Stevens (1986) to obtain his path corrections from NTS to 24 WWSSN station in United States and Canada and to 12 SRO stations. For his models he used  $n = 2$ . The negative sign results from the differences in our sign criteria for vertical displacement. In Stevens (1986) vertical displacement is positive up while in this article it is positive down. The phase velocity factor is due to the use of wavenumber spreading by Bache *et al* (1976), Harkrider (1981), and Stevens (1986) compared to geometric spreading by the others. Bache *et al* (1976) based their expressions on the conservation of lateral energy flux while these expressions are from the main term in an asymptotic expansion.

Glover & Harkrider (1986) performed numerical tests in order to estimate the frequency range for which these approximations were valid for Rayleigh waves generated at NTS where the source region may be limited by sharp boundaries such as in the low velocity basin at Yucca Flat. Rayleigh wave seismograms were calculated for explosive sources at depth in a finite vertical cylinder with contrasting elastic properties representative of the various test areas at NTS embedded in a vertically stratified propagation media. The technique couples laterally inhomogeneous finite-element calculations of the source region with Green's functions for teleseismic Rayleigh waves using the elastodynamic representation theorem. The details of the technique can be found in Harkrider (1981) and Bache *et al* (1982). The spectra for these Rayleigh waves were then compared with those, which used the two approximations to cross the sharp boundary. It is surprising that both approximations

worked as well as they did since they based on theories which assume gradual transition zones. It was found that both approximations worked equally well for periods greater than four seconds and that for shorter periods the asymptotic approximation used in this paper is better. The period range is dependent on the material contrast and the vertical extent of the contrast but this mixed path approximation is certainly adequate for the determination of long period moments and surface wave magnitudes from NTS Rayleigh wave observations at continental stations.

It is interesting to note that for this geometry, ie.  $n = 2$  the Rayleigh wave transmission coefficient,  $T(\omega)$ , of Bache *et al* (1976)

$$T(\omega) = \left( \frac{c_2 \mathbf{A}_2}{c_1 \mathbf{A}_1} \right)^{1/2} = \left( \frac{U_1 I_1}{U_2 I_2} \right)^{1/2} \quad (8)$$

is identical to the factor  $R$  of Levshin(1986) and was used in both articles to illustrate the effect of mixed paths on the amplitude of Rayleigh waves.

For each source to receiver path a theoretical Rayleigh wave is generated. The Earth model used to create this synthetic is meant to reflect the average Earth structure between NTS and the given station. The Earth models used in this study were determined from inversions of dispersion and attenuation data as well as forward modeling of the waveform to fine tune the models. The criteria for determining the goodness of fit of the synthetic to the data are dispersion, absolute travel time and waveform fit (relative amplitude of different dispersed phases). Hence the synthetic seismogram displays the same spectral and time domain waveform characteristics as the data which it simulates. This was done for all paths. The paths to WWSN and Canadian stations were taken from the explosion moment study by Stevens (Stevens, 1986). The RSTN, LLN and DWWSN path composite structures were determined by us.

To determine  $M_s$  for a particular source-receiver geometry two synthetics are generated. One which is propagated the actual path distance that is meant to simulate the data and one which is propagated to  $40^\circ$ . At  $40^\circ$  the surface wave train is well dispersed and stable, so that a conventional  $M_s$  value can be calculated.

Fig. 3 illustrates this method. The upper set of seismograms are a comparison of data to its corresponding synthetic seismogram. For this particular example the station COR (Corvallis, Oregon) and the event Stilton are used. The data is the solid line and the dashed line is the synthetic time series. Note that the waveform fit (dispersion and relative amplitude) is exceptional. This feature is important in order to make maximum peak to peak amplitude comparisons. The middle figure schematically shows the propagation paths for the synthetic seismograms. The path of length  $R$  is the actual source to receiver distance. The longer path is of length  $40^\circ$ . The bottom figures are of the two synthetic seismograms. The left one is calculated for the distance  $R$  ( $9.3^\circ$  in this case) and the right seismogram is the one propagated out to  $40^\circ$ . They are plotted to the same time scale. Note the much better dispersed wave train in the  $40^\circ$  case. The arrows in the right-hand figure mark the cycle or phase of the record which is used to obtain a  $M_s$  value.

To calculate  $M_s$  we use a modified version of the Von Seggern formula (Von Seggern, 1977):

$$M_s = \log_{10}(A/T) + 1.08 \times \log_{10}(\Delta) + 4.38, \quad (9)$$

where  $A$  is one-half the maximum peak to peak amplitude (in microns) for periods between 17 and 23 seconds of a well dispersed wavetrain measured from the vertical record,  $T$  is the period of the arrival measured in seconds, and  $\Delta$  is the propagation distance in degrees. This formula was chosen because the distance coefficient (1.08) more closely approximates the effect of attenuation along continental paths (Basham, 1971, and Marshall & Basham,

1972). Evernden (1971) found the distance coefficient to be 0.92 for  $M_s$  measurements at less than 25° and 1.66 for measurements at greater distances.

A vertical component measurement has two advantages over horizontal component measurements. The horizontal components usually have lower signal to noise ratios than the vertical component and generally are more likely to be contaminated by Love wave signals which may be generated by tectonic release, source effects, or scattering due to lateral variations in the Earth's structure.

Both the regional and teleseismic synthetics are generated with the same site and source function, so that the peak to peak amplitude of the Rayleigh pulse of the regional synthetic can be directly related to the  $M_s$  value determined for a theoretical Rayleigh wave train propagated out to 40°. The relationship between the data peak to peak amplitude and its indirect  $M_s$  is:

$$M_s(data) = M_s(synth|_{40^\circ}) + \log_{10}[(PPA|_{data})/(PPA|_{synth})], \quad (10)$$

where PPA is the peak to peak amplitude of the Rayleigh pulse. A path correction may be included on the right side of this expression.

This path correction is the difference between the individual path synthetic derived  $M_s$  and the average theoretical  $M_s$  for the entire network. For each source-receiver pair, a  $M_s$  is calculated from a synthetic seismogram propagated to 40°. Each such synthetic has the same size source, so ideally one would want each  $M_s$  value so measured to be equal in value. Yet this is not so, for each path's dispersion and effective attenuation at the periods of interest may be different. The difference between the mean synthetic network  $M_s$  and a particular receiver  $M_s$  is the path correction. A negative path correction value implies that the theoretical 40° station  $M_s$  is larger than the network average. Table 1 lists the network

path corrections used.

The question arises, whether or not it is valid to use the average Earth structure for a particular path to propagate a surface wave to  $40^\circ$  when the Earth model is only meant to reflect the seismic properties of the Earth for a path that may only be a small fraction of this distance. This is particularly true of the shortest paths for which the seismic waves traverse only western, North America, an area of relatively high attenuation compared to the continental craton and shield areas. A surface wave propagated  $40^\circ$  along a characteristic tectonic North American crust and mantle model (NTS to DUG, for example) for  $40^\circ$  will be much more attenuated than a wave propagated the same distance through an average structure from NTS to the eastern seaboard (NTS to SCP, for example). Hence the calculated  $M_s$  for the NTS to DUG structure would be smaller than the NTS to SCP  $M_s$ .

There are several methods to correct for this path dependent effect. As explained above one may implement path corrections which account for the theoretical difference in attenuation between paths. Another means is to make a mixed path structure which has the appropriate path structure from the source to the actual station distance, with the rest of the path out to  $40^\circ$  being a generic seismic velocity and attenuation model. For the cases in this study where the structures which comprise the mixed path are both continental structures (*i.e.* not too dissimilar) the approximation is robust enough for the synthetic seismogram calculations.

We have implemented both procedures individually and in conjunction to see what their effects are. Another method would be to include empirical station corrections (Yacoub, 1983, Given & Mellman, 1986). The findings concerning the path corrections are discussed in the results section.

Besides the  $M_s$  determination, we also calculated a time domain moment for the same

data. This time domain, scalar moment is determined as follows:

$$M_O(data) = M_O(synth) \times [(PPA|_{data}) / (PPA|_{synth})], \quad (11)$$

where PPA is the peak to peak amplitude of the Rayleigh pulse or Airy phase. This method is simpler than the  $M_s$  method and has the added advantage that the synthetic involves only two structures; the source region and the propagation path to the station. Path corrections were not incorporated into the time domain  $M_O$  determinations since the propagation path synthetic takes the place of a path correction and we are not correcting to a generic structure. Making a correction based on the difference between the average station value and some mean for a collection of events is a form of the classical empirical station correction and is most useful when there are only a few stations reporting since a zero sum of the corrections is the usual constraint (Given & Mellman, 1986). The mean moment can then be converted to an  $M_s$  using the moment- $M_s$  relation for the generic structure propagated to  $40^\circ$ , *i.e.*

$$M_s(ptpk) = \log M_O(ptpk) - 11.38 \quad (12)$$

Fig. 4 plots  $M_s$  vs.  $M_O(ptpk)$  for the entire data set. The correlation between the two types of magnitude measurements is extremely good, with only a few slight outlying points. The regression constant 11.42 is very close to the theoretical value 11.38 given above. Thus the difference between our best mixed path  $M_s$  regression with moment and the  $M_s$  relation to moment for a pure path of the generic RSSD model is only .04 magnitude units. This indicates our  $M_s$  values are relatively insensitive as to whether we use the RSSD model for the last part of the propagation path from the station to  $40^\circ$  or for all of the path. On first glance it might appear that both techniques are identical. This would be true if we didn't make the additional correction to a mean of the theoretical values for all stations

in the mixed path evaluation. These observations imply that the RSSD model is a good average model for the network and that our  $M_s$  calculations are sound and result in robust measurements of surface wave magnitude, which are not too dependent on which of the two techniques we use. In our analysis of the data we will use only  $M_s$  measurements. A table of the log  $M_O$  and their standard deviations will be given in Woods & Harkrider (1992b).

Before going on to spectral estimates, we should mention the effect of source structure. For all of the techniques, we use the Stevens (1986) and Given & Mellman (1986) NTS source elastic structure, which is basically a Pahute Mesa velocity structure. By numerical simulations using a variety of different NTS structures, we found that for the frequencies of interest and sources in the upper 6 kilometers, the primary effect was due the difference in shot point velocity ratios. The size of the effect can be predicted extremely well from their explicit presence in the mixed path expression, equation (6). As an example, our Green's functions are for an explosive source at a depth of 600 meters. In the Stevens (1986) source structure, the second layer starts at a depth of 500 meters. There is a significant difference in the Poisson's ratio of the surface and second layers. The log difference between the square of their compressional to shear velocities would predict from equation (6) an  $M_s$  difference of 0.17. The actual difference between the  $M_s$  of a surface explosion and our Green's function is 0.16 with the near surface explosion smaller as predicted. In order to reduce the effect of differing shot point velocity ratios, Stevens (1986) suggested a new explosion moment,  $M'_O$ , defined by

$$M'_O = 3 \frac{\beta^2}{\alpha^2} M_O \quad (13)$$

For a shot point medium with Poisson's ratio of 0.25 or a square velocity ratio of 3, the value of the moment is unchanged.

In Fig. 2, we see that for the WWSSN stations, denoted by three letters, the dominant period is much lower than the recommended lower cutoff of 17 seconds for the standard  $M_s$  formula. By dominant period we mean the apparent period of the maximum amplitude. This was determined by using twice the time difference between the arrival of the largest peak and trough. We also calculated the 'instantaneous period' of this arrival but because of low pass filtering it was essentially the same. The dominant period at each station is given in Table 1. For the WWSSN stations, the periods are between 10 and 15 seconds. Most are near 11 seconds. For the digital stations, denoted by four letters, the dominant period is between 15 and 19.5 seconds. Most are near 16 second. An alternate approach for using the maximum amplitude of Rayleigh wave observations where the dominant period is significantly different than 20 second was developed by Marshall & Basham (1972). Using the stationary phase approximation they determined a path correction, which corrected for the dispersive characteristics of the path. Using observed dispersion curves for North America, Eurasia, mixed ocean-continent, and pure ocean paths, they were able to determine an  $M_s$  correction based on the period of an observed Airy phase to the 20 second period arrival in North America or Eurasia. Their North American dispersion correction for our network stations based on our dominant period determinations is also given in Table 1 (column 2). An advantage of our technique is that our path corrections are independent of recording instrument whereas Marshall & Basham's correction depends on the dominant period, which depends not only on dispersion but also instrument response. As an example, the station ALQ has a dominant period of 12 seconds and ALQD has a dominant period of 19.5 seconds.

Another advantage that time domain estimates of  $M_s$  or  $M_0$  have over spectral estimates can be seen in Fig. 2. Except for the work of Patton (eg. Patton, 1991), the Green's functions

used for spectral estimates of explosions have been fundamental Rayleigh and Love waves. As can be seen from the figure, it is very important to isolate the fundamental surface wave in the data before taking its spectra for moment estimates. The Rayleigh waves at almost every station show the additional presence of higher modes. The higher modes are primarily due to constructive interference of multiple reflected shear waves and are therefore very sensitive to lateral variations in crust and upper mantle structure. This is especially true for non parallel layers with sharp contrasts. Therefore in the presence of nearby signals or noise, it makes more sense to use the larger time domain amplitudes of the fundamental mode Airy phases at regional distances. Because of the possibility of tectonic release, it is also necessary to determine the polarity of the surface wave. Again this is best done in the time domain especially for Love waves.

If a spectral estimate is desired, comparing the Green's function with the data in the time domain should allow one to determine time windows and tapers so as reduce the contamination of spectral amplitude estimates with higher modes and spurious scattered arrivals at intermediate ranges. And at close ranges where this may not be possible, it should help in deciding which time domain amplitude measurements best represent the spectral amplitudes of the fundamental modes.

The question remains how well do either of these two measurements compare to spectral moment estimates. For the events for which digital data were available, spectral-domain moments were determined. Spectral moments were calculated using the method of Stevens (1986), with the exception that station corrections were not included in our moment calculations. Spectral moments were calculated in the band-width between 10 and 60 seconds. These spectral moments will be referred to as  $M_O$ . Moments were also obtained by inverting

for a isotropic moment (explosion)  $M_I$ , and a deviatoric moment (tectonic release or asymmetric source cavity). Details of these moments are the subject of another paper by these authors (Woods & Harkrider, 1992b).

We compare the time-domain moments with these two types of spectral-domain moments in Fig. 5a and 5b. The top figure compares  $M_O(ptpk)$  to  $M_O(\omega)$  and the bottom figure compares  $M_O(ptpk)$  to  $M_I(\omega)$ .  $M_O(\omega)$  refers to an average spectral scalar moment and  $M_I(\omega)$  refers to the isotropic moment determined from a moment tensor inversion scheme (Woods & Harkrider, 1992b). The correlation of  $M_O(ptpk)$  to either spectral moment is consistent. In the top figure there are several events with significant scatter in the lower moment range, with the time-domain moments being significantly larger than the spectral-domain moments. Most of these events are Rainier events, the one outlier which is below the water table is the event Rex, which has an anomalously large component of deviatoric moment (double couple) moment (Woods & Harkrider, 1992b). These outlying Rainier events can be explained in two ways. First, these events are relatively small and are only measured at very few stations (sometimes only one to three stations), thus the scatter, or error, in the moment measurement is larger. One problem with this explanation is that there are other small events recorded at Pahute Mesa and Yucca Flat that lie right on the moment scaling curve (Fig. 5a) and these events have moment measurements at no more stations than the Rainier events. The other possibility is that these outlying events reflect differences in source spectra. As discussed previously the time-domain moments measure energy predominantly in the 10-14 second range, the period range of the continental Airy phase, whereas the spectral moment is an average of the spectral ratio between 10 and 60 seconds. So, it is possible that the Rainier test sites excite more high frequency energy than do either the Pahute or Yucca

sites.

## DATA ANALYSIS AND RESULTS

The seismograms were band-passed filtered between 6 and 100 seconds to minimize contaminating noise as described previously. The vertical records were visually inspected to insure that the correct time window was used and that their signal to noise ratio was above (approximately) 2.0.  $M_s$  values were then calculated for the data as per the method described above (equation 9) with several variations. The synthetic seismograms were also band-passed filtered between 6 and 100 seconds for consistency. The  $M_s$  values are plotted against seismic magnitudes of several scales for the same set of events. It should be noted that complete magnitude lists were not available for all 190 events.

We chose to compare or plot our data primarily with body wave magnitudes determined by Lilwall & McNeary (1985). The Lilwall-McNeary (LM) data set contains 143 of the 190 events examined by us and is believed to be a well determined and self-consistent list of  $m_b$  values that have small errors due to, among other things, the inclusion of network station corrections. Fig. 6 shows the  $m_b$ -yield relationship for events in this study for which  $m_b$  and yield information were available. It is important to notice that events above and below the water table separate into two distinct populations. For this data set this separation is only apparent near the cluster of events with  $m_b$ 's around 5.4. Also notice the very small error bars for this data; for many events the error bars are smaller than the symbols demarking a data point. The solid line is the best-fitting, least squares curve, with the dashed curves being the two sigma confidence interval of this regression. The correlation between  $m_b$  and yield is good, with the scatter mostly being due to the above water table shots. The slope of the regression curve is 0.67.

This value is slightly lower than that found in other studies of teleseismic  $m_b$ -yield scaling relationships. Marshall *et al* (1979) found that  $m_b$  was proportional to  $Y^{0.74}$  for well-coupled Yucca flat explosions, and proportional to  $Y^{0.78}$  for explosions throughout NTS and Amchitka. Longer period teleseismic body-wave magnitudes  $m_{LPP}$  introduced by Basham and Horner (1973) show that for events in tuff and rhyolite the amplitude of the arrivals is proportional to  $Y^{0.72}$ . Murphy (1977) compared theoretical  $m_b$ -yield scaling relations for cube-root scaling models and the modified Mueller and Murphy (1971) source model. He found that the yield exponent varies between 0.6 and 1.0 for the cube-root model in the yield range of interest, whereas the exponent is a constant 0.85 for the modified model. Schlittenhardt (1988) found  $m_b$  to be proportional to  $Y^{0.82}$  for NTS explosions. The empirically derived curves have errors in their slopes on the order of 0.05 to 0.1 units and are based on small sampling populations. The LM  $m_b$ -yield scaling relationship is determined from a significantly larger data set, making it at least as reliable a scaling curve.

The same scaling law slope ( $\sim 0.67$ ) holds for the LM data when they were separated with respect to test site and shot medium coupling (whether detonated above or below the water table). There is consensus in the literature that that seismic coupling is a function of the percentage dry (or gaseous) porosity of a material. In a study of small scale, high explosive experiments with 15 rock-types, Larson (1981) found for a given size explosion that a porous material's (such as tuff) elastic radius increased with increasing water content. The dominant non-linear mechanism (within the plastic radius) working at low yields appears to be pore crushing of the surrounding material (Stevens *et al* , 1991). Non-linear finite difference calculations (Bache, 1982) also indicate that porosity is the most important characteristic of NTS tuff. In the same study, source functions for Yucca Flat wet and dry tuff are

significantly different, with the wet tuff's long-period amplitude being larger by 50 percent and its corner frequency being lower. Springer (1966) has observed this effect for teleseismic P-wave amplitudes. Gupta *et al* (1989), Patton (1988), and Vergino & Mensing (1989) have observed this coupling effect in regional phases such as Lg,  $P_n$  and  $P_g$ .

Several sets of synthetic Rayleigh waves were calculated at the 40° distance. One set was propagated along the single structure model (hereafter referred to as the single path case) which reflects the average Earth structure between NTS and a given station. We also constructed mixed-path synthetics for which, that part of the path beyond the actual source-receiver distance, out to 40°, the surface wave is propagated along a generic earth structure. The NTS-RSSD Earth structure was chosen for this generic path section, as it is a relatively simple structure which generates stable surface waves and it is roughly an intermediate range station (distance < 1900 km), so that its structure can be considered to be an "average" structure for the network.

Surface magnitudes were first calculated from the 40° synthetics generated with a single structure propagation path. Fig. 8a and 8b display single path  $M_s$  values, calculated as described above, versus body-wave magnitude ( $m_b$ ). These  $m_b$ 's are those of Lilwall and McNeary (1985). In the upper left-hand figure on the right, the  $M_s$ 's are calculated without path corrections, whereas path corrections are included in the figure below. The solid line is the best fitting weighted least-squares regression of the data, with the weighting factor being inversely proportional to individual event standard deviations. The dashed lines represent the two standard deviation error of the fit of the line to the data. Solid black circles are shots below the water table, shots above the water table are open circles, and open squares are shots for which this information is not known. Note the error bars are approximately 50

percent larger for the uncorrected  $M_s$ 's (Fig. 8a) than for the case of path-corrected  $M_s$ 's (Fig. 8b). The scatter in the data is also significantly less for the path corrected  $M_s$ 's, so it appears that the path corrections do improve  $M_s$  measurements.

There are two significant effects of including path corrections. One is the reduction in variance of individual magnitudes. Without path corrections the individual station magnitudes have a bi-modal distribution reflecting the two generic earth models of North America: the tectonic western and cratonic eastern crust and upper mantle structures. The path corrections bring-in the outlying station magnitudes values towards the mean value. Including path corrections for the single-path derived  $M_s$ 's increases the average value by 0.14 units (or 32%). This effect can be attributed to the smaller events which are brought more in line with the curve containing larger events. This in turn is due to the fact that the smaller events are only observed at nearer stations in tectonic western North America, for which path structures exhibit higher attenuation, so that surface waves propagated along such a path for 40° will significantly more attenuation than models reflecting more cratonic or shield paths. Path corrections reduce this effect significantly for the single-path derived magnitudes.

Table 1 lists these network path corrections. The third column lists the corrections for single path synthetics. A positive value denotes that the  $M_s$  for a station is smaller than the network theoretical average.

We next explored the effect of mixed path transfer functions upon the  $M_s$  calculations. As described above, we chose the path to RSSD as a generic structure for the second portion of the mixed path synthetic seismogram calculations. We generated two sets of these synthetics. The difference between these two mixed path earth structures is in their spectral attenuation coefficients, with  $\gamma_\beta$  being twice as large, at a given frequency, for the mixed path 2 case as

for the mixed path 1 case. Fig. 7 shows the attenuation factors (*gamma*) as a function of period. The line labeled RSSDx2 is that of the increased attenuation structure. It is referred to as "mixed path 2" throughout this study. The lower, dashed curve is the attenuation curve for the RSSD structure. Synthetics made with this RSSD generic structure for the latter portion of the 40° travel path will be referred to as "mixed path 1". Table 1 gives the path corrections for each station for these two cases, also.

In Fig. 8c and 8d the  $M_s$  magnitudes were calculated using synthetic seismograms using the mixed path 1 model. In Fig. 8c the  $M_s$ 's are calculated without path correction terms, while in Fig. 8d path corrections are included. The addition of the path correction terms cuts the data variance, but by no more than 25%, and then not in all cases. Assuming a fixed slope regression ( $m=1.50$ ), there is no off-set in the intercept between the uncorrected and path-corrected  $M_s$ 's. So using a generic structure for the remainder of the 40° path acts a path correction effect as well.

Fig. 8e and 8f are  $M_s$  vs.  $m_b$  plots for the mixed path 2 case without and with path corrections, respectively. What is most striking is that the slope of the regression line is nearly the same (1.50 vs. 1.54) for the two, mixed-path, path-corrected cases (Fig. 8d and 8f). We will then take the  $M_s$ - $m_b$  scaling relationship to be:

$$M_s = 1.50 \times m_b + B. \quad (14)$$

For this fixed-slope scaling relationship, the uncorrected and path-corrected mixed path 1  $M_s$  curves have the same intercept, whereas for the mixed path 2 case the intercept is 0.10 units larger for the path-corrected curve than for the uncorrected curve. The intercept off-set between path-corrected mixed-path 1 and mixed-path 2 curves is 0.2 units and follows from the fact that the attenuation for the second portion of the path is twice as large for the

mixed path 2 case as that for the mixed path 1 case.

For the single path case, path corrected  $M_s$  values give nearly the same relationship (slope=1.54), but the slope is significantly larger (1.64) for the uncorrected magnitudes, although the difference lies within the errors bounds. It would seem that both path corrections and mixed path Green's functions improve  $M_s$  determinations for the method used here.

To obtain stable, robust  $M_s$  values with this method it is best then to use mixed path generated synthetics in conjunction with path corrections for the  $40^\circ$   $M_s$  measurements. The variance among the mixed path based  $M_s$  values for the network is smaller than that when  $M_s$  is derived from single path synthetics, so that magnitude measurements will be more consistent when they are determined from mixed path synthetics. This is particularly important for events with few reporting stations. All further plots of  $M_s$  in this study use values obtained from the mixed path 1 case with path corrections, unless stated otherwise.

How well the final  $M_s$  values reflect the actual seismic magnitude of these events necessitates having another measure of their size. In the event of anomalously high or low seismic source coupling, for example, both body waves and surface waves should be affected similarly by coupling effects. A magnitude parameter independent of seismic observations would be useful to plot the  $M_s$  against, so we have also fitted our results to estimated log yields. Fig. 8 shows the relationship. Yield values are estimated to be within 10 percent of the actual yield (Springer & Kinnaman, 1971). Yield information was available for 174 of the events, thus yields make-up the most comprehensive data set to compare our results to as well. The yields for this data set range over three orders of magnitude in size. The greatest scatter, as in the case of  $M_b$  vs. log yield, is due to shots above the water table. It should also be

be kept in mind that the scatter would be further reduced if the data were separated into populations based on their location at NTS, (*i.e.* Pahute Mesa, Rainier Mesa and Yucca Flat).

Since our magnitude values are based on theoretical continental structures, as well as the particular network used, we wanted to compare our  $M_s$  values to those obtained from more standard  $M_s$  methods. Fig. 9 shows our  $M_s$  values (y axis) versus those from six other studies (x axis) (Basham, 1969, Marshall & Basham, 1972, Marshall, Springer & Rodean, 1979, Basham & Horner, 1973, Yacoub, 1983 and Von Seggern, 1973). The overlap in data sets varies between 8 and 16 events. We performed a fixed-slope (slope=1.0), linear regression of our  $M_s$  values to those of the six outside studies; in general the correlation is very good. It's important to note that with our method we are able to measure  $M_s$  for events 0.75 units smaller than the smallest events of the other studies, *i.e.* events down to  $M_s = 1.75$ . We are able to measure  $M_s$  for these smaller events, because we are able to make use of near-regional (< 500 km) records with the method described in this paper.

The offset in  $M_s$  values between ours and the other scales varies considerably. This offset is due in part to the difference in definition of  $M_s$  for each study, in particular the distance term. As discussed earlier, we chose the distance correction term ( $1.08 \times \log_{10}(\Delta)$ ), whereas the other studies use a variety of ones. Yacoub (1983) and Basham (1972) use variations of the Prague formula: ( $1.66 \times \log_{10}(\Delta)$ ) (Båth *et al*, 1967). Von Seggern (1973) used a slightly smaller distance factor ( $0.9 \times \log_{10}(\Delta)$ ) than that of his later study which we use. The other three studies use distance corrections developed by Marshall & Basham (1972) and all have offsets of approximately 0.45 magnitude units. The difference in distance correction factor is believed to be the primary cause of the offset in magnitude between their results

and ours. These three studies, as well as that of Basham (1969) use mostly, if not all, data recorded at Canadian stations, thus their networks have strong azimuthal and distance biases as well, which may also affect magnitude measurements. It should be noted that the method described in this study to calculate  $M_s$ , also is based upon a theoretical network average  $M_s$ , so it will have a bias attached to it which is dependent upon the network used. This network bias may be responsible for part of the offset, as well.

Our network does have considerably better azimuthal coverage than these other studies, so that tectonic release effects upon the long-period radiation, assuming strike-slip faulting, should be mitigated, thus giving more accurate  $M_s$  measurements. In the next paper we show that the network of all useable stations causes a variable bias if tectonic release is not corrected. These stations were not included in this study but are important in determining the size of tectonic release in Woods & Harkrider (1992b).

A significant difference between our  $M_s$  calculations and those of the other studies is that we include data from close-in stations. Whether or not our  $M_s$  values have some functional dependence upon distance is an important point to consider. Fig. 10a plots relative event  $M_s$  vs. distance for the entire data set. No apparent distance dependence is observed. We also examined this relation for individual events and found the evidence more compelling that there is no distance dependence for the  $M_s$  values. This fact makes this  $M_s$  method very attractive, particularly for small events, for which Rayleigh wave amplitudes are measurable only at near distances, because there will be no bias in magnitude values between large and small events. Fig. 10b shows the relative event  $M_s$  vs. azimuth. There is some variation with azimuth. This is to be expected for we do not take into account tectonic release in our  $M_s$  calculations. Azimuthal variations in propagation paths, caused, perhaps, by different

tectonic regions may also be a source of this effect.

Table 2 lists the final mixed-path, path-corrected  $M_s$  values for the 190 events of this study. The first column lists the number of stations recording the event. Next are given the surface wave magnitude and associated error for the event are given. Next is a three letter shot information code. The first letter denotes its geographic location: Yucca (Y), Pahute (P), Rainier (R), or Climax Stock (C). The second is whether its shot depth was above (A) or below (B) the water table. The last letter describes the shot site rock as tuff (T), rhyolite (R), granite (G), or alluvium (A). An underscore means that the information is not known. The final two columns are the event's name and Julian data, respectively. The events are listed in chronological order.

To determine the portability of this  $M_s$  calculation method the events need to be separated into groups based on their source regions and then compared, one group to another, in order to see if there are systematic differences in  $M_s$  values relative to any other magnitude scale. Three main geographic source regions comprise the event data set: Pahute Mesa, Rainier Mesa and Yucca Flat.

Whether or not a shot occurs within saturated material is another criterion by which to separate events in order to look for systematic differences in  $M_s$  values. Other studies have found significant seismic coupling differences between explosions detonated above and below the water table (Gupta, 1989, Marshall *et al* , 1979 and Vergino & Mensing, 1989), so it would seem to be a reasonable parameter to study. Reviewing Fig. 6, it is also apparent that for shots fired-off below the water table have a larger seismic magnitude than those detonated above the water table.

Fig. 11a shows the relationship between  $M_s$  vs. Lilwall  $m_b$  for all NTS events. The surface-

wave magnitudes were all calculated using mixed-path Green's functions (with the RSSD-1 structure for the generic path part) and path corrections. The vertical error bars represent the one standard deviation confidence interval for each  $M_s$  value. A linear least squares regression was performed to determine the scaling relationship. The solid line represents this curve and the dashed lines represent the two sigma confidence level of this curve. Fig. 11b and 11c divide the data populations into above and below the water table, respectively; shots for which water table information was not available were left out. Although all but one Rainier Mesa event were detonated above the water level, we found that their coupling ( $M_s$  vs. log yield) was diagnostic of explosions detonated below the water table. Taylor (1983) notes that Rainier Mesa sports a perched aquifer. We believe that the Rainier Mesa events are detonated within this zone, hence they are assumed to be well-coupled events, i.e. the pore space of the shot medium is filled with water and thus pore space crushing will not be a strong effect.

The bottom three figures (11d,e,f) plot the same data, but a constrained least squares fit was performed with the slope=1.50. The off-set in curves between events detonated above and below the water table is 0.10. This amount is within the scatter of the data, thus statistically insignificant, so it would appear that shot medium coupling effects associated with pore-filling phenomena are similar for surface waves and P-waves.

Fig. 15a-c are  $M_s$  vs. log-yield plots analogous to Fig 11a-c. It is important to note that the individual explosion variances are about the same size for the entire range of yields, so that our predicted yield values for small events should be as accurate as for the larger events. The scaling relation between  $M_s$  and log yield (assuming the scaling relationship has a slope of 1) is such that for a given yield an explosion below the water table couples more

strongly by 0.52 units - a substantial amount. For  $m_b$ -yield scaling the coupling effect is 0.28 units. For individual source regions, the off-set in the  $M_s$ -yield and  $m_b$ -yield scaling curves for events above and below the water table vary slightly from these values determined from the entire data set. Although there is some scatter in the data of, which is not surprising considering the diversity of the sampled populations, the best-fitting  $M_s$ - $m_b$  curves are well constrained, for the population covers a wide range of magnitudes.

Fig. 12a gives the  $M_s$ - $m_b$  relationship for all Yucca events. The regression curve is not significantly different from that of Fig. 11a. The scatter in the data is reduced by 25 percent over that of the general population. Separating the events with respect their relation to the water table yields Fig. 12b and 12c. There is no significant difference in the  $M_s$ - $m_b$  relationship between the two data sets. The free-slope regression curves are not as well constrained as those of Fig. 11 because the yield range for Yucca explosions is smaller than that of the entire data set, however the fixed-slope curve for the entire Yucca data set does lie within the two-standard deviation confidence interval of the two free-slope regression curves for the separated populations. Fig. 12e and 12f show that the  $M_s$ - $m_b$  ratio is not appreciably different between explosions detonated above and below the water table. When the Yucca  $M_s$  data are regressed vs. log yield, as shown Fig. 15d-e, it is found that events below the water table couple more efficiently by 0.61 log units or a factor of four. This is a significant amount and the data set on which it is based is more extensive than that of the  $M_s$ - $m_b$  regression. Springer (1966) found that high dry porosity (60 effectively than in saturated alluvium.

Fig. 13a plots all Pahute event  $M_s$ 's vs. their respective  $m_b$ 's. The relationship is essentially the same as for the Yucca data above. The unconstrained below and above water table curves

(Fig.'s 13b,c) are close to their Yucca counterparts (Fig.'s 12b and c). The slope of these curves are nearly the same as that for Yucca below water table shots, although the intercept differs appreciably. This result implies that for a given  $m_b$ , surface wave magnitudes for events at Pahute Mesa are larger than those at Yucca Flat by 0.39  $M_s$  units. Fig.'s 13b and 13c (constrained fits) bare out this fact, so that for a given  $m_b$ ,  $M_s$  values at Pahute Mesa will be larger than those at Yucca Flat. For the  $M_s$ -log yield relationship, there is also an appreciable difference between Yucca and Pahute events detonated in water-saturated material (0.23 units). The Pahute data are plotted in Fig.'s 16d-ef. For the case of events exploded in dry material there is a significant difference with Yucca events having a  $M_s$  0.44 units smaller than Pahute events. These coupling factors are determined from intercept offsets of fixed slope regressions.

Fig.'s 14a-f display the  $M_s$ - $m_b$  regression curves and data for Rainier Mesa events in combination with and without Pahute Mesa data. Fig.'s 16a-c are analogous figures for the  $M_s$  vs. log-yield data. Although the clustering of Rainier data near  $m_b = 5.0$  causes the curve to be poorly constrained, a slope close to that for Pahute events and Yucca (below the water table) is obtained. Comparison of the equations at the bottom of Fig.'s 13e and 14e give an off-set of 0.47 between  $M_s$  estimates at Pahute and Rainier (for a given  $m_b$ ). Either the Pahute site is more efficient at producing surface waves or the Rainier site is more efficient at coupling body-wave energy. Rainier events are tunnel shots. The immediate source region ( $R < 200$  m) may behave like an asymmetric cavity, resulting in a source that is non-isotropic (Zhao and Harkrider, 1991) and/or seismic coupling that has strong frequency dependence. Either of these effects may account for this difference. The difference in  $M_s$ -log yield scaling relationship is somewhat less (0.31 units), implying that Rainier more efficiently couples

short-period energy than Pahute.

### CONCLUSION

The method described herein to calculate surface wave magnitudes allows the measuring of  $M_s$  for nuclear explosions over a wide magnitude distribution. Using this technique, it is now possible to use near-regional ( $\Delta < 15^\circ$ ), long-period records in conjunction with the far-regional ( $\Delta < 15^\circ$ ) and teleseismic records, that have previously been used to make conventional  $M_s$  measurements, in order to measure surface wave magnitudes. This increase in observations has several advantages. First, for any event the station network coverage is enhanced in terms of overall numbers as well as in azimuthal coverage, in particular stations only several hundred miles away from NTS in California, Nevada and Utah can be included in a network that otherwise would have no coverage to the west or southwest. These improvements make the network  $M_s$ 's more stable and statistically robust. Secondly, smaller events with surface waves that haven't been analyzed will now have such observations available, so that their surface wave magnitudes now can be calculated. For other potential study areas there may well be similar geographical constraints requiring the use of a similar type of near-regional ( $< 500$  km) seismic network. The methods described herein also produce stable  $M_s$  values that are consistent with other seismic magnitude scales. Thirdly, the effect of inaccuracies in estimating  $Q$  are negligible for very near-regional recordings. With the  $M_s$  calculation technique used here, one can take advantage of such nearby recordings. Lastly this method makes it very easy to use historical analog data sets more easily, for it is not necessary to use digitized data if only the maximum peak to peak amplitude needed to calculate  $M_s$ 's in this fashion.

From the results obtained with the data set used here, there does appear to be significant

differences in seismic coupling between NTS sub-sites, with events at Pahute Mesa producing larger surface-wave magnitudes for a given  $m_b$  than at Rainier Mesa or Yucca Flat. For well-coupled events this discrepancy is largest for Rainier Mesa events.

As stated earlier the method used here to obtain  $M_s$  values lends itself to such a diverse data set, for the measurement of the smallest events is facilitated with near-regional observations. Fig. 17 illustrates this point. It shows the unrotated three-component data for Floydata (8/15/91,  $m_b = 4.2$  ( $Y < 5$  Kt if detonated below the water table or  $Y < 10$  Kt if detonated above the water table) at Yucca Flat recorded by three of the TERRAscope stations and played out with a Press-Ewing 30-90 filter. The source to receive distances are between 210 and 390 km. The maximum peak to peak amplitudes are quite small ( $< 0.5$  mm). On the actual analog instrument it would not be possible to measure the surface wave amplitude. Because of the low signal to noise ratio a spectral moment would be of dubious value. However the  $M_s$  method described in this paper would furnish an accurate surface wave magnitude with which to estimate its yield. These small surface wave magnitudes, based on near-regional data would also be of considerable value for discrimination purposes.

Although Lg measurements with a calibration shot give more accurate estimates of explosion yields, there may be cases where Lg "blockage", caused by strong lateral variations in the propagation path, may occur and one must use other methods, such as surface wave magnitudes, instead to estimate yields or for discriminating the event.

Discrimination methods primarily use the difference in spectral content between earthquakes and explosions as a discriminant. Using surface wave magnitudes in conjunction with higher frequency body-waves takes advantage of the large discrepancy in long-period/short-period ratio between explosions and earthquakes. With the  $M_s$  method detailed herein, it is

possible to lower the threshold of this discrimination technique.

*Acknowledgments.* This research was supported by the Defense Advanced Research Projects Agency (DOD), Nuclear Monitoring Research Office and was monitored by Air Force Geophysics Laboratory under Contract F19628-89-K-0028 and also was supported by Phillips Laboratory of the Air Force Systems Command under Contract F19628-90-K-0049. Contribution No. 5187, Division of Geological and Planetary Sciences, California Institute of Technology, Pasadena, California.

## REFERENCES

- Alewine, R. W., 1972. Theoretical and observed distance corrections for Rayleigh-wave magnitude, *Bull. Seism. Soc. Am.*, *62*, 6133-6142.
- Babich, V. M., Chikhachev, B. A. & Yanovskaya, T. B., 1976. Surface waves in a vertically inhomogeneous halfspace with a weak lateral inhomogeneity. *Izv. AN SSSR, Fizika Zemli*, *4*, 24-31.
- Bache, T. C., Rodi, W. L., & Harkrider, D. G., 1978. Crustal structures inferred from Rayleigh-wave signatures of NTS explosions, *Bull. Seism. Soc. Am.*, *68*, 1399-1413.
- Bache, T. C., Day, S. M., & Swanger, H. J., 1982. Rayleigh wave synthetic seismograms from multidimensional simulations of underground explosions. *Bull. Seism. Soc. Am.*, *72*, 15-28.
- Bache, T. C., 1982. Estimating the yield of underground nuclear explosions, *Bull. Seism. Soc. Am.*, *72*, s131-s168.
- Båth, M., 1967. Recommendations of the IASPEI committee on magnitudes, *Seismological Bull.*, May, Seismological Institute, Uppsala.
- Basham, P.W., 1969. Canadian magnitudes of earthquakes and nuclear explosions in south-western North America, *Geophys. J. R. astr. Soc.*, *17*, 1-13.
- Basham, P. W. & Horner, R. B., 1973. Seismic magnitudes of underground nuclear explosions, *Bull. Seism. Soc. Am.*, *63*, 105-131.
- Burridge, R. & Weinberg, H., 1977. Horizontal rays and vertical modes, *Wave Propagation and underwater acoustics*, Springer-Verlag, Berlin, Heidelberg, New York.
- Douglas, A., 1966. Redetermination of earthquake body-wave magnitudes using ISC Bulletin data, United Kingdom Atomic Energy Authority, *AWRE Rept. No. O54-66*. H.M.S.O. London.
- Evernden, J. F. & Filson, J., 1971. Regional dependence of surface-waves versus body-wave magnitudes, *J. Geophys. Res.*, *76*, 3303-3308.
- Evernden, J. F., 1971. Variation of Rayleigh-wave amplitude with distance, *Bull. Seism. Soc. Am.*, *67*, 405-411.
- Given, J. W. & Mellman, G. R., 1986. Estimating explosion and tectonic release source parameters of underground nuclear explosions from Rayleigh and Love wave observations, *Sierra Geophysics Inc. Rept. No. SGI-R-86-126*, AFGL-TR-86-0171, Kirkland, WA. ADB110040

- Glover, P. & Harkrider, D. G., 1986. Numerical tests of surface wave path corrections, *Science Applications International Corp. Rept. No. C86-05*, MDA903-84-C-0020, McLean, VA.
- Gupta, I. N., C. S. Lynnes, W. W. Chan and R. A. Wagner, 1989. A Comparison of the Spectral Characteristics of Nuclear Explosions Detonated Below and Above the Water Table, *Teledyne Geotech Rept. No. TGAL-89-04*, GL-TR-89-0151, Alexandria, VA. ADA214595
- Harkrider, D. G., 1964. Surface waves in multilayered media I. Rayleigh and Love waves from buried sources in a multilayered elastic half-space, *Bull. Seism. Soc. Am.*, *54*, 627-679.
- Harkrider, D. G. & Anderson, D. L., 1966. Surface wave energy from point sources in plane layered earth models. *J. Geophys. Res.*, *71*, 2967-2980.
- Harkrider, D. G., 1981. Coupling near source phenomena into surface wave generation, *Identification of Seismic Sources - Earthquake or Underground Explosion*, editors: Husebye and Mykkeltveit, D. Reidel, Dordrecht, Boston, London. 277-326.
- Larson, D. B., 1981. Explosive energy coupling in geologic materials, *Lawrence Livermore National Laboratory, Report UCID-85662*,.
- Levshin, A. L., 1985. Effects of lateral inhomogeneities on surface wave amplitude measurements, *Annales Geophysicae*, *3*, 511-518.
- Lilwall, R. C. & Neary, J. M., 1985. Redetermination of earthquake body-wave magnitudes using ISC Bulletin data, United Kingdom Atomic Energy Authority, *AWRE Rept. No. O 21/85*,. H.M.S.O. London.
- Marshall, P. D., Douglas, A. & J. A. Hudson, J. A., 1971. Surface waves from underground nuclear explosions, *Nature*, *234*, 8-9.
- Marshall, P. D. & Basham, P. W., 1972. Discrimination between earthquakes and underground explosions employing an improved Ms scale, *Geophys. J. R. astr. Soc.*, *28*, 431-453.
- Marshall, P. D., Springer, D. L. & H. C. Rodean, 1979. Magnitude corrections for attenuation in the upper mantle, *Geophys. J. R. astr. Soc.*, *57*, 609-638.
- Mueller, R. A. & Murphy, J. R., 1971. Seismic Characteristics of Underground Nuclear Detonations, *Bull. Seism. Soc. Am.*, *61*, 1675-1692.
- Murphy, J. R., 1977. Seismic source functions and magnitude determinations for underground nuclear detonations, *Bull. Seism. Soc. Am.*, *67*, 135-158.

- Patton, H. J., 1988. Application of Nuttli's method to estimate yield of Nevada Test Site explosions recorded on Lawrence Livermore National Laboratory's Digital Seismic System, *Bull. Seism. Soc. Am.*, *78*, 1759-1772.
- Patton, H. J., 1991. Seismic moment estimation and the scaling of the explosion source, *Geophysical Monograph 65: Explosion Source Phenomenology*, editors: S. R. Taylor, H. J. Patton and P. G. Richards; AGU, Washington, D. C., 171-183.
- Saito, M., 1967. Excitation of free oscillations and surface waves by point sources in a vertically heterogeneous earth. *J. Geophys. Res.*, *72*, 3689-3699.
- Schlittenhardt, J., 1988. Seismic Yield Estimation Using Teleseismic P- and PKP-waves Recorded at the GRF-(Graefenberg) array, *Geophys. J.*, *95*, 163-179.
- Springer, D. L., 1966. P-wave coupling of underground explosions, *Bull. Seism. Soc. Am.*, *56*, 861-876.
- Springer, D. L. & Kinnaman, R. L., 1971. Seismic source summary for U. S. underground nuclear explosions, 1961-1970, *Bull. Seism. Soc. Am.*, *61*, 1073-1098.
- Stevens, J. L., 1986. Estimation of scalar moments from explosion-generated surface waves, *Bull. Seism. Soc. Am.*, *76*, 123-151.
- Stevens, J. L., 1991. Seismic source characteristics of cavity decoupled explosions in salt and tuff, *Bull. Seism. Soc. Am.*, *81*, 1272-1291.
- Sykes, L. R. & Cifuentes I. L., 1984. Yields of Soviet underground nuclear explosions from seismic surface waves: compliance with the Threshold Test Ban Treaty, *Proc. natl. Acad. Sci. U.S.A.*, 1922-1925.
- Taylor, S. R., 1983. Three-dimensional crust and upper mantle structure at the Nevada Test Site, *J. Geophys. Res.*, *88*, 2220-2232.
- Vergino, E. S. & Mensing, R. W., 1989. Yield estimation using regional mb(Pn), *Lawrence Livermore National Laboratory Report UCID-101600*.
- Von Seggern, D., 1973. Joint magnitude determination and analysis of variance for explosion magnitude estimates, *Bull. Seism. Soc. Am.*, *63*, 827-845.
- Von Seggern, D., 1977. Amplitude distance relation for 20-Second Rayleigh waves, *Bull. Seism. Soc. Am.*, *67*, 405-511.
- Werth, G. C. & Herbst, R. F., 1963. Comparison of amplitudes of seismic waves from nuclear explosions in four mediums, *J. Geophys. Res.*, *68*, 1463-1475.
- Woodhouse, J. H., 1974. Surface waves in a laterally varying layered structure. *Geophys. J. R. astr. Soc.*, *37*, 461-490.

- Woods, B. B. & Harkrider, D. G., 1992, Isotropic and deviatoric moment inversion for NTS explosions, *to be submitted to Geophys. J. Int.*,
- Yacoub, N. K., 1983. "Instantaneous amplitudes": A new method to measure seismic magnitude, *Bull. Seism. Soc. Am.*, 73, 1345-1355.
- Yomogida, K., 1985. Surface waves in a laterally slowly-varying media. *Geophys. J. R. astr. Soc.*, 82, 511-533.
- Zhao, L. S. & Harkrider, D. G., 1992. Wavefields from an off-center explosion in an imbedded solid sphere, *in press Bull. Seism. Soc. Am.*,

## Figure Captions

**Figure 1.** Map of North American station network used in this study. The "spoked wheel" is the Nevada Test Site.

**Figure 3.** Comparison of vertical component Rayleigh-wave waveforms. The data time series are the upper, thicker traces; the lower trace in each case is the fundamental mode synthetic. All time series band-passed between 60 and 6 seconds.

**Figure 3.** (Schematic of the  $M_s$  Calculation Method) The top figure is a comparison of observed to synthetic seismograms for the event Lowball recorded at the WWSN station COR ( $\Delta=10.4^\circ$  degrees. This record shows a prominent Airy phase with a dominant period that is considerably less than 20 seconds. The solid line is the observed time series and the dashed line is that of the synthetic seismogram. Both time series have been band pass filtered between 60 and 6 seconds.

The middle figure shows the paths for which synthetic Rayleigh waves are calculated. There are two receiver distances. One,  $R$ , is the distance between the actual receiver and the source. The other is distance is  $40^\circ$ . A synthetic generated for the distance  $R$  is made with a structure which best models the regional seismogram.

The bottom two figures show synthetic seismograms calculated for the two receiver distances for the COR path model. The left-hand one is for the actual regional path distance  $R$ ; it is flipped in polarity with respect to the same synthetic in the top figure. The right-hand one is a Rayleigh wave propagated to  $40^\circ$ ; the arrows denote the pulse that is used to calculate  $M_s$ . Notice that the dominant period for this case is 17.5 seconds. This pulse is considerably closer in period to 20 seconds than that of the regional seismogram which has a period near 12 seconds.

**Figure 4.** Time domain  $M_s$  values regressed vs. time domain moments for all the events in this study. Note the extremely good correlation between the two scales. Vertical error bars are the variance for the individual events.

**Figure 5.** Time domain log moments regressed against spectral domain moments. In the top figure spectral moments were determined assuming an isotropic source only, while in the bottom figure the spectral moments were determined by inverting for a isotropic source + a double-couple source. The regressions were constrained to a slope of unity.

**Figure 6.** Lilwall- $m_b$  vs.  $\log$ -Yield for events from this study. The solid line is the best-fitting regression line. The dashed lines show the 95 percent confidence interval of this line. Lines through the data points represent one standard deviation in a datum measurement. Blackened circles represent sources beneath the water table, open circles are events above the water table and open squares are events for which this information is not known. Events detonated below the water table have a larger  $m_b$  for a given yield. Besides this separation of data, there is little scatter to the data. The consistency of the  $m_b$ -yield relationship makes it reasonable to use these  $m_b$  values to plot our  $M_s$  measurements against.

**Figure 7.** The two attenuation models for the generic portion of the hybrid propagation model are plotted versus period. Gamma is the attenuation coefficient at a given period. Model RSSDx2's attenuation is twice that of the RSSD model.  $M_s$  values calculated with synthetics using model RSSD are referred to as mixed path 1, while values determined from synthetics created using attenuation model RSSDx2 are referred to as mixed path 2.

**Figure 8 a-f.** Here  $M_s$  is plotted vs. Lilwall  $m_b$ 's. For the left figures  $M_s$  is calculated with single path Green's functions, without path corrections (npc) and with path corrections (pc). The best-fitting regression model is the solid line running through the data points. The dashed lines are the two sigma confidence intervals of the line. The  $M_s$ - $m_b$  relationship and the r.m.s. error of the data are at the bottom of each figure. The middle figure  $M_s$  values are determined using the mixed path 1 synthetics and in the right two figures mixed path 2 Green's functions were used.

**Figure 9 a-f.**  $M_s$  of this study regressed against those determined by other studies.

**Figure 10.** Relative  $M_s$  (individual station - network average) vs. distance (top figure) and azimuth (bottom figure).  $M_s$  values do not appear to be a function of distance. There also is no apparent functional relationship between azimuth and  $M_s$ ; some azimuths are not covered, however.

**Figure 11.a-f**  $M_s$  regressed vs. Lilwall  $m_b$  for all NTS events. The data are also separated with respect to shot point being above and below the water table. The bottom figures are constrained least-square regressions assuming a slope of 1.53.

**Figure 12. a-f**  $M_s$  regressed vs. Lilwall  $m_b$  for Yucca events. The data are also separated with respect to shot point being above and below the water table. The bottom figures are constrained least-square regressions assuming a slope of 1.53.

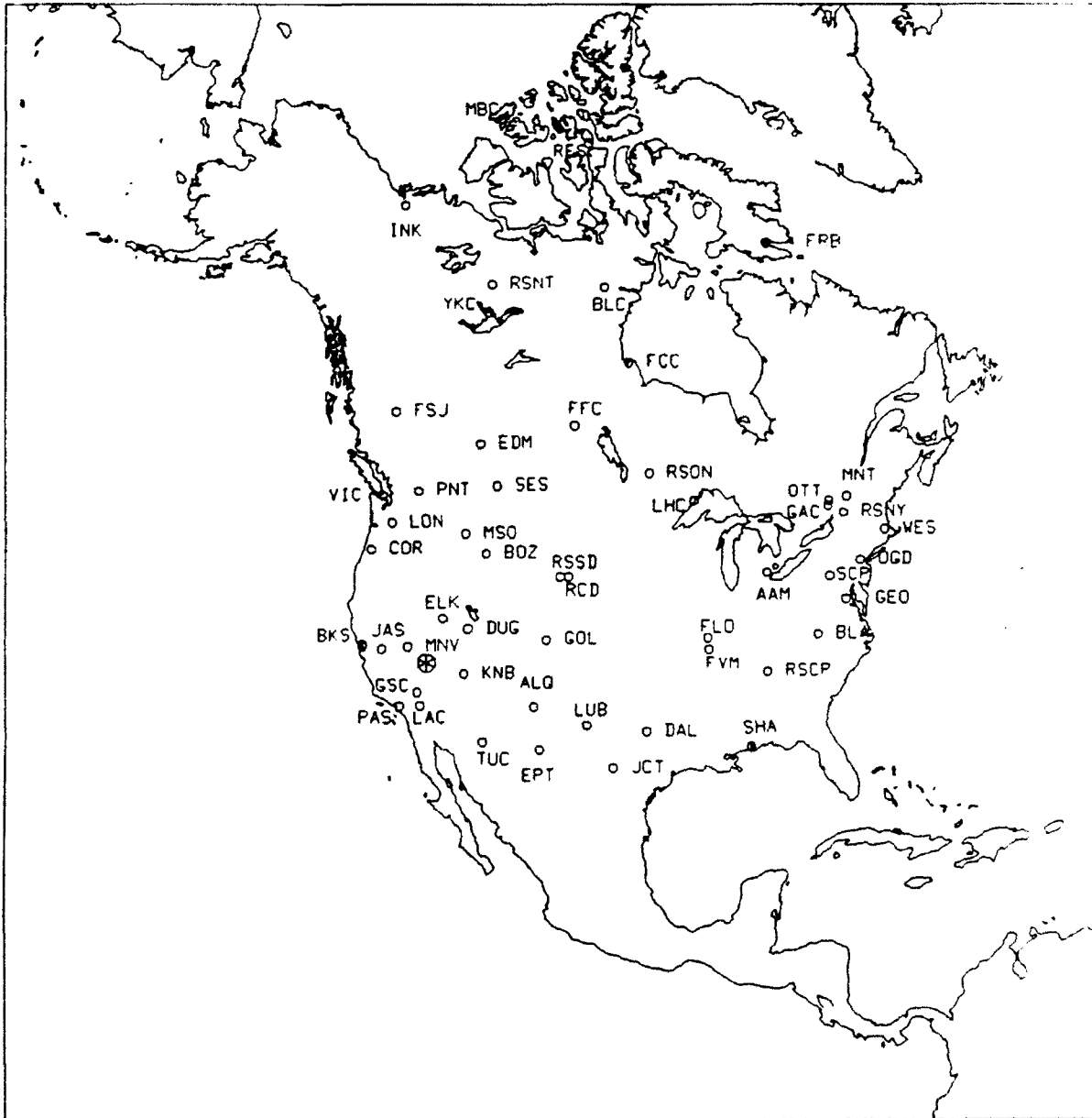
**Figure 13.a-f**  $M_s$  regressed vs. Lilwall  $m_b$  for Pahute events. The data are also separated with respect to shot point being above and below the water table. The bottom figures are constrained least-square regressions assuming a slope of 1.53.

**Figure 14.a-f**  $M_s$  regressed vs. Lilwall  $m_b$  for Pahute and Rainier events. Regression of Rainier data alone (middle figures), all Rainier and Pahute events (left figures), and all Rainier events with Pahute shots below the water table (right figures) are shown. The bottom figures are constrained least-square regressions assuming a slope of 1.33.

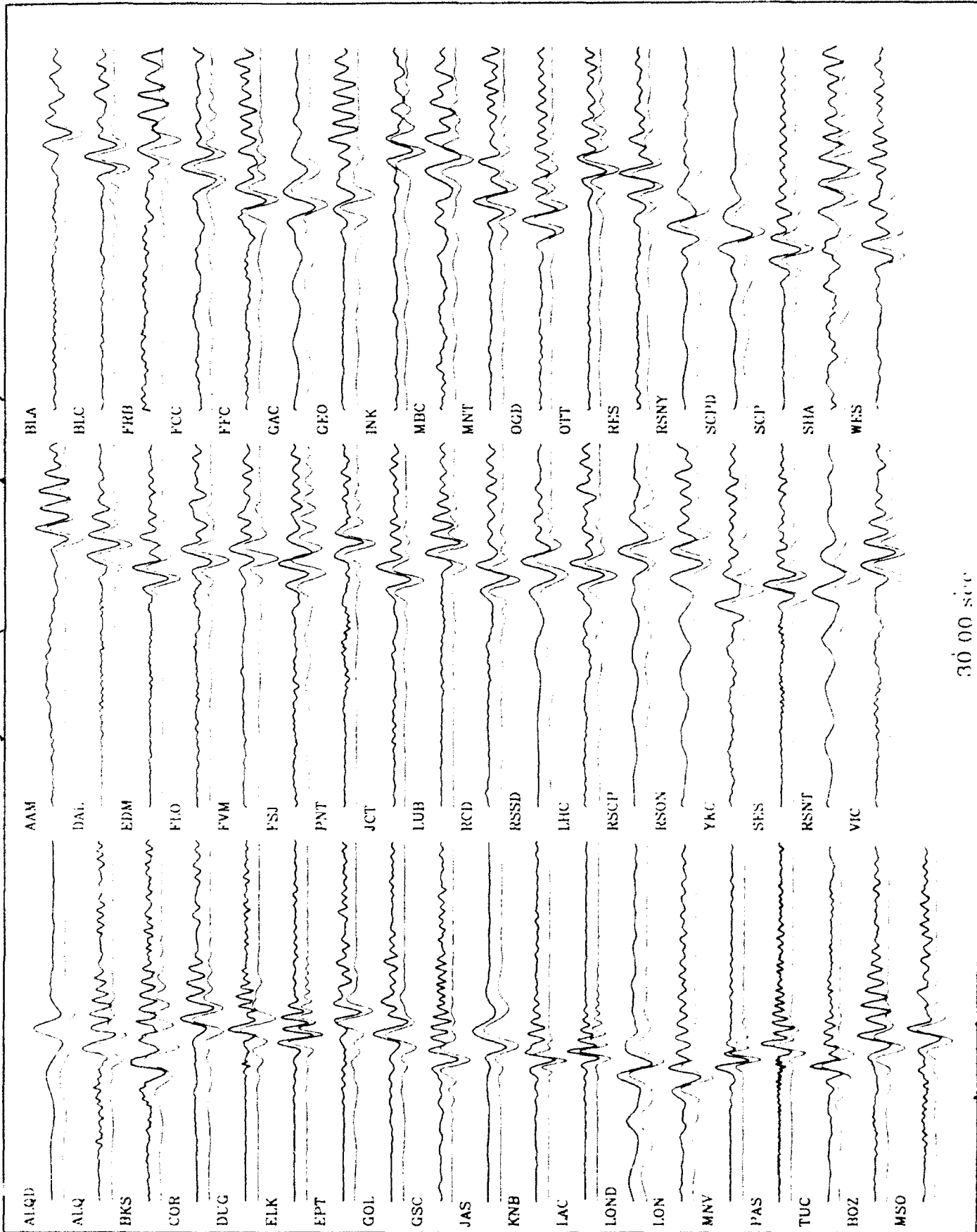
**Figure 15. a-f**  $M_s$  regressed vs. Log Yield for all NTS events (top figures) and for Yucca events (bottom figures). Event populations have also been grouped with respect to shot point water table location.

**Figure 16. a-f**  $M_s$  regressed vs. Log Yield for Pahute and Rainier events (top figures) and for Pahute events alone (bottom figures). Event populations have also been grouped with respect to shot point water table location.

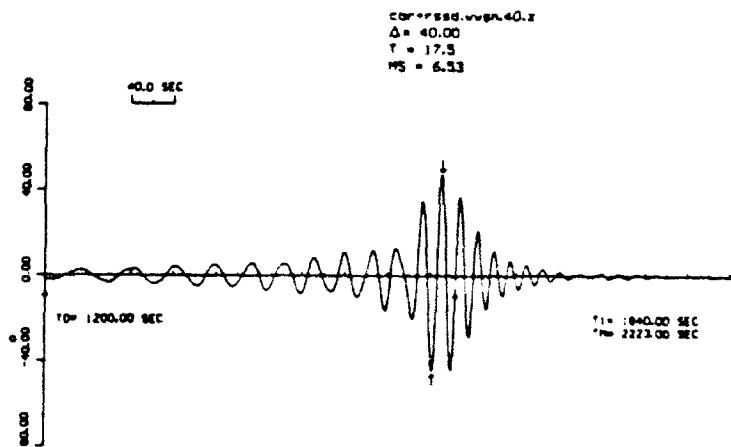
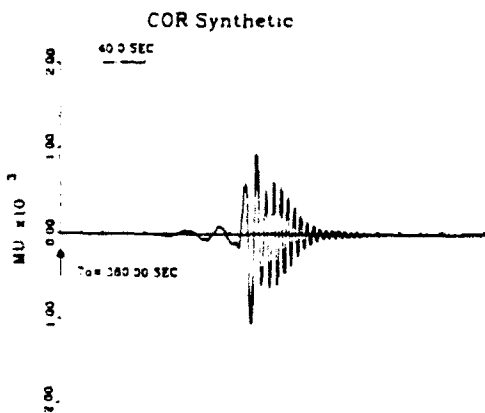
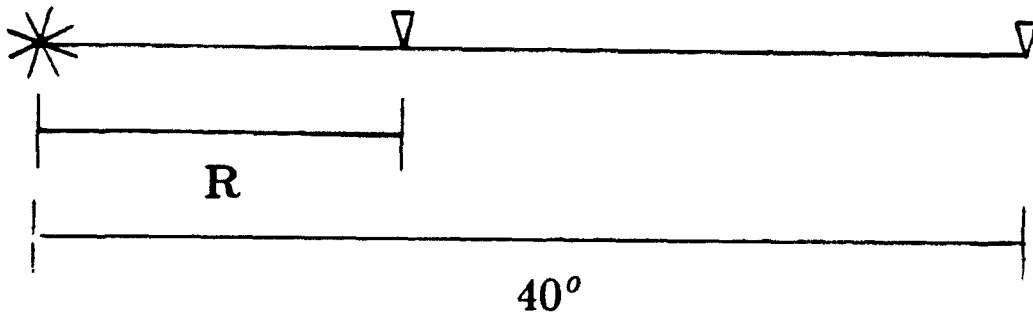
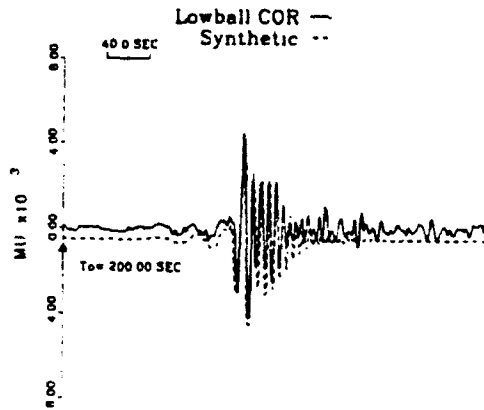
**Figure 17.** TERRAScope streckeisen recordings of a NTS explosion Floyd data at Yucca Flat on 8/15/91 with an estimated yield of  $< 10$  kt. The broad-band records have been convolved with a Press-Ewing 30-90 instrument (top traces), and lower traces have been convolved with a Wood-Anderson short period torsion instrument. All four stations record the surface wavetrain well enough to measure the Airy phase peak amplitudes. Records from an actual 30-90 long-period instrument would be unusable.



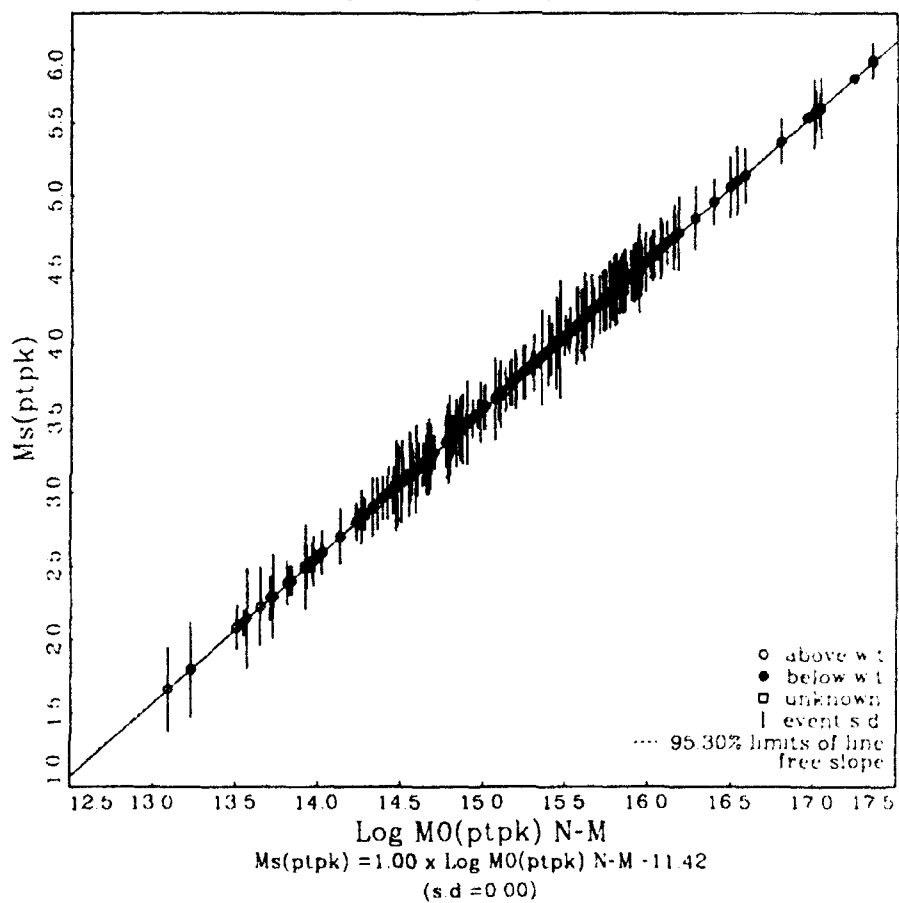
Data vs. Synthetic (vertical component)



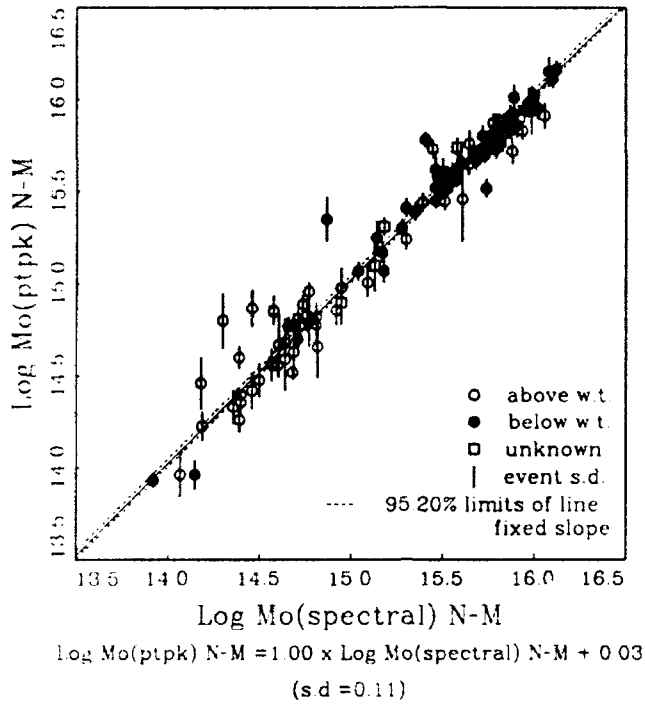
# Schematic of the $M_s$ Calculation Method



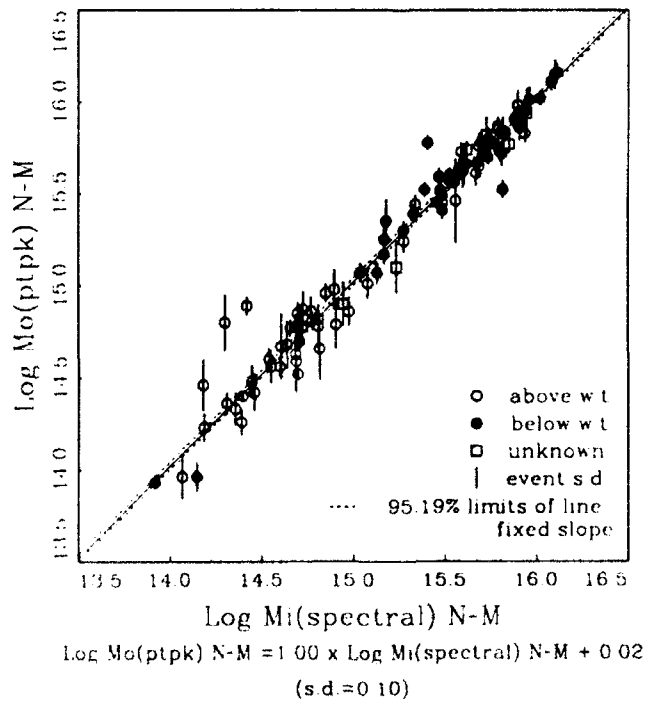
Ms(ptpk) vs log M0(ptpk), NTS



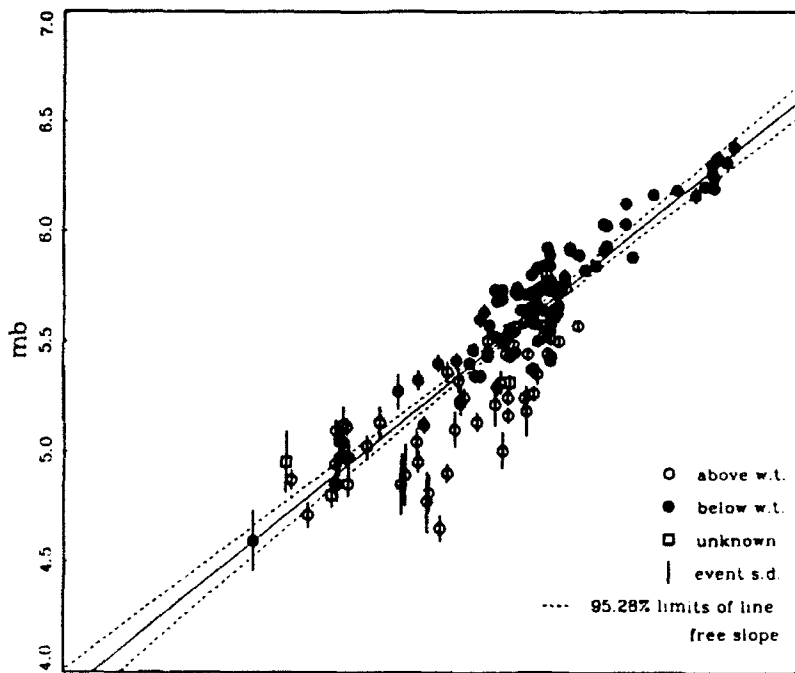
### Mo(ptpk) vs MO(spectral)



### Mo(ptpk) vs Mi(spectral)



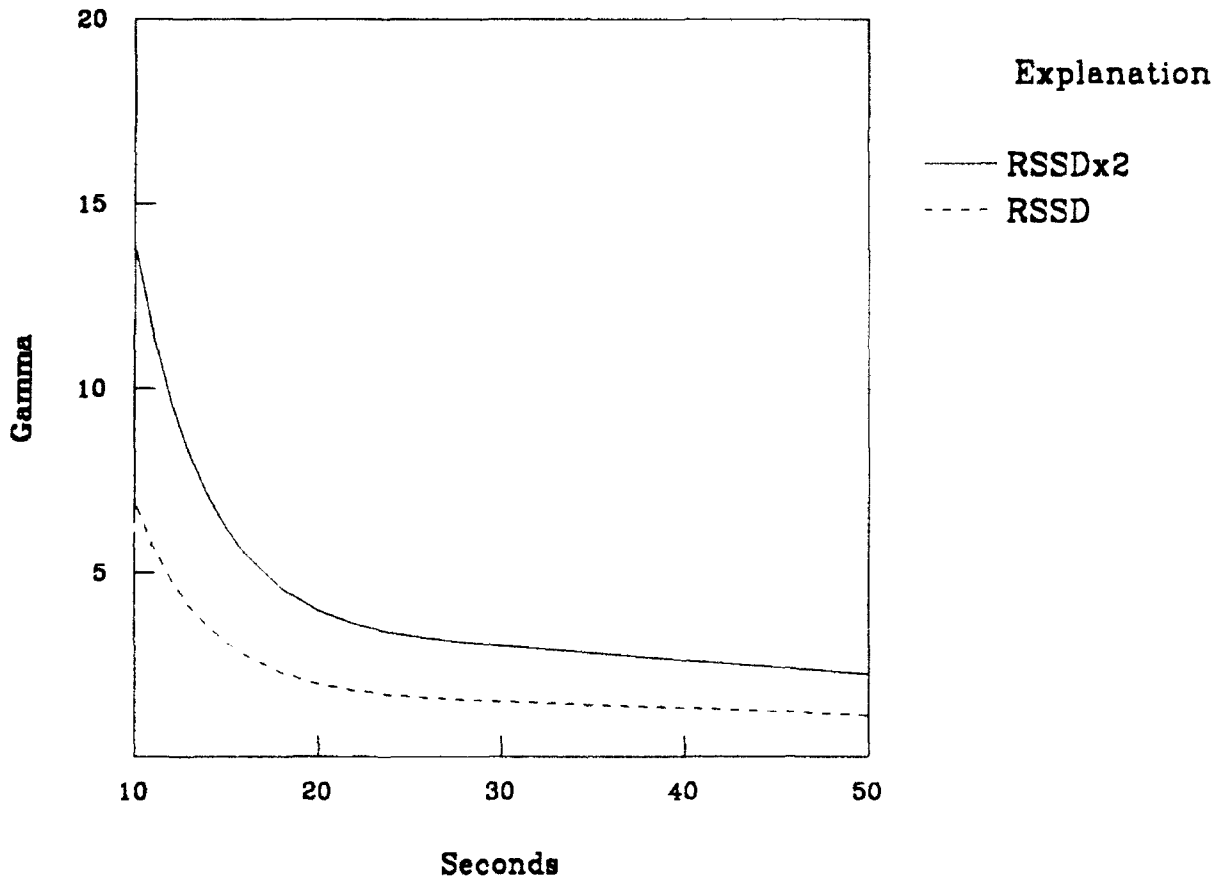
mb(Lilwall) vs. Log Y



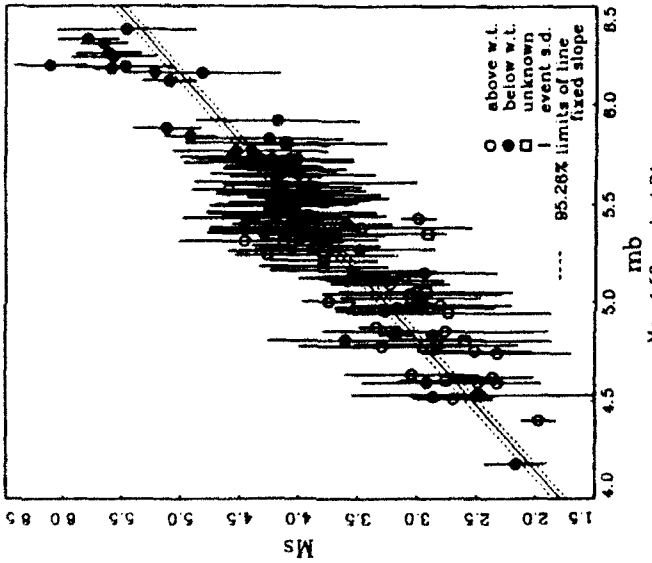
Log Y

(s.d.=0.15)

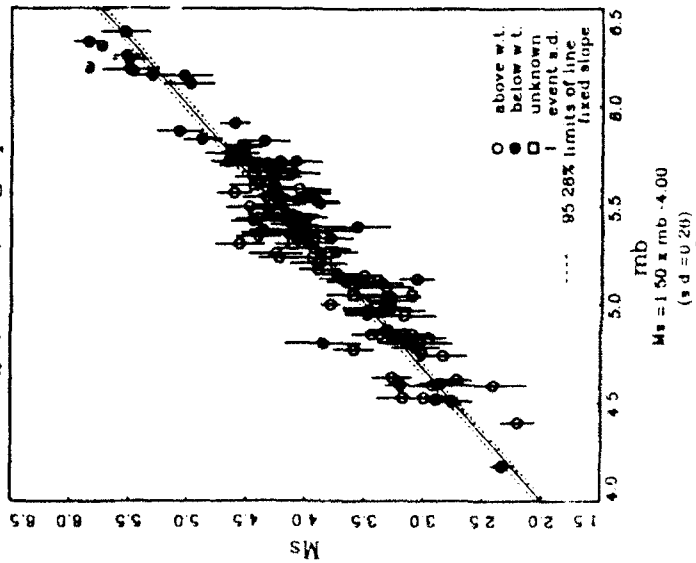
### Attenuation vs Period



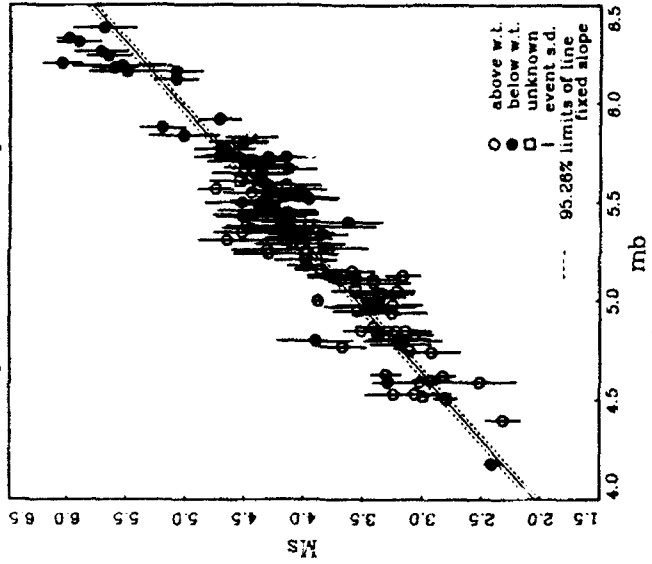
Ms(np) vs mb, single path



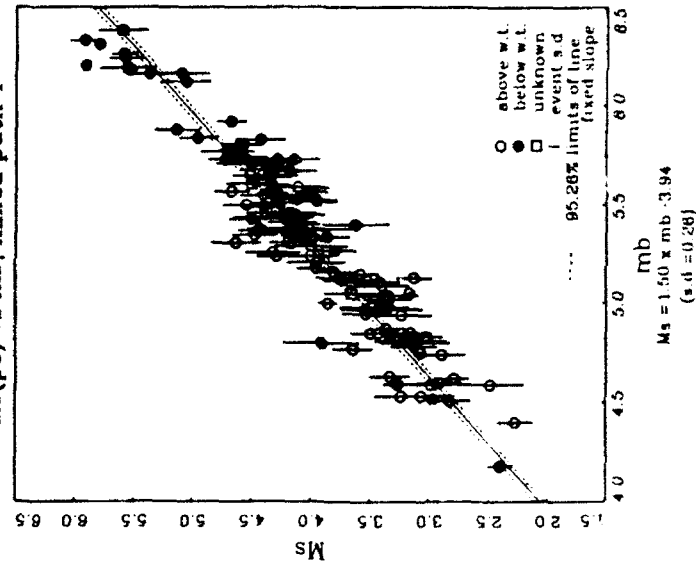
Ms(pc) vs mb, single path



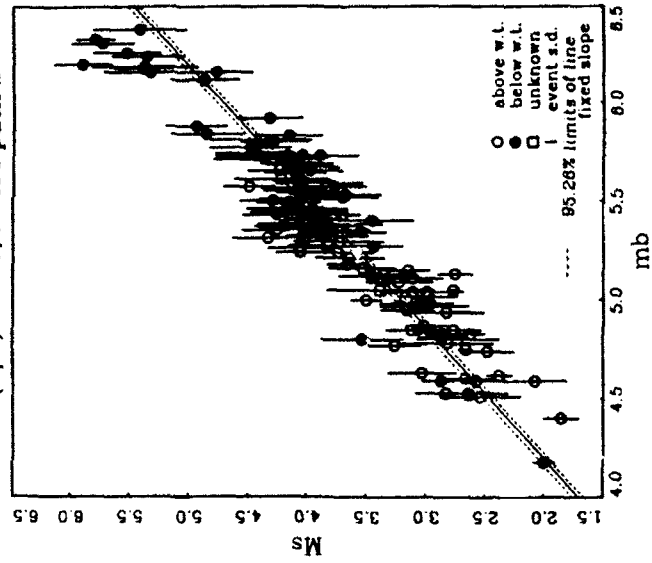
Ms(np) vs mb, mixed path 1



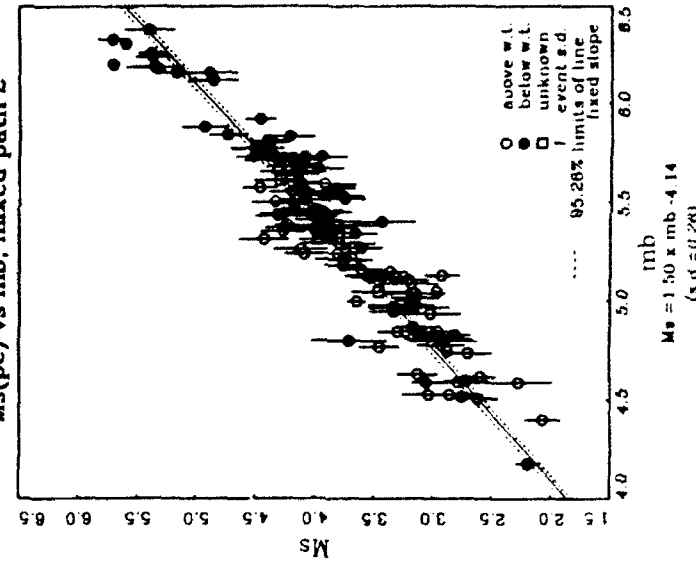
Ms(pc) vs mb, mixed path 1



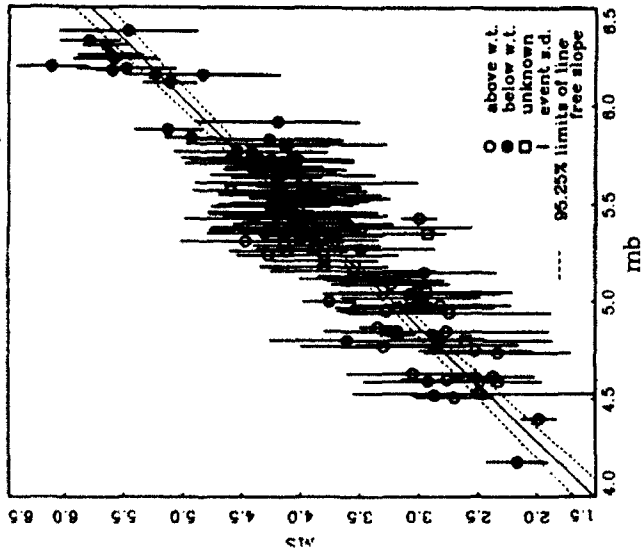
Ms(np) vs mb, mixed path 2



Ms(pc) vs mb, mixed path 2



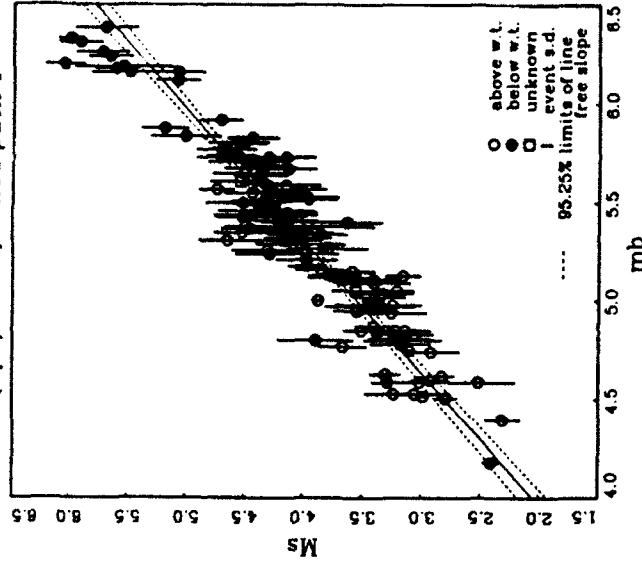
Ms(npc) vs mb, single path



$M_s = 1.71 \times m_b - 5.33$   
(s.d. = 0.32)

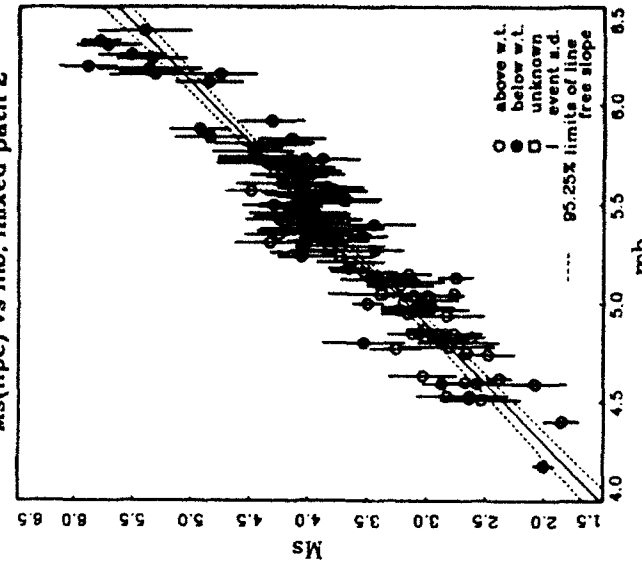
68

Ms(npc) vs mb, mixed path 1



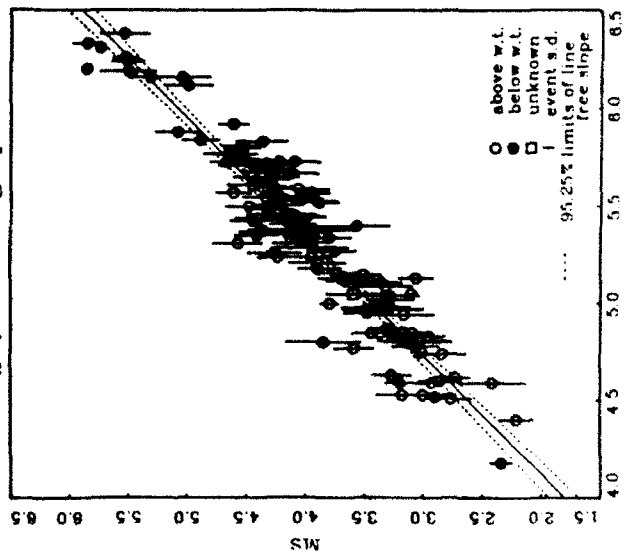
$M_s = 1.49 \times m_b - 3.92$   
(s.d. = 0.24)

Ms(npc) vs mb, mixed path 2



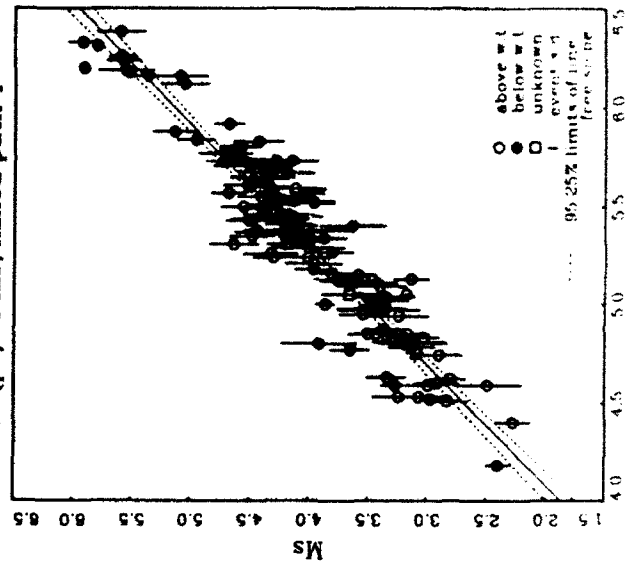
$M_s = 1.65 \times m_b - 5.07$   
(s.d. = 0.27)

Ms(pc) vs mb, single path



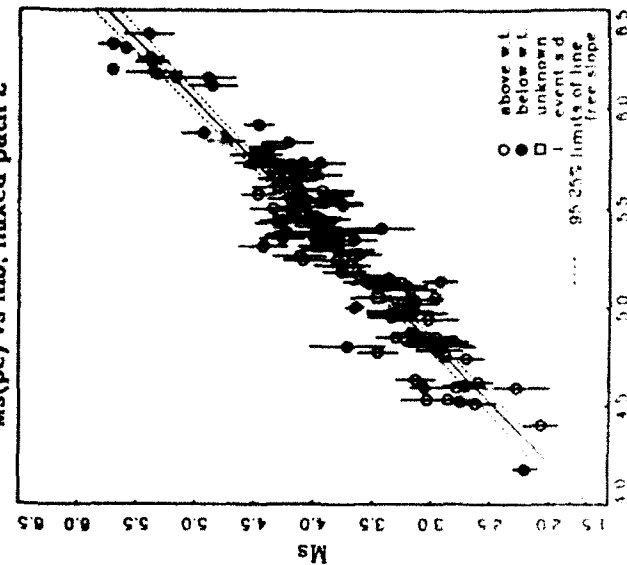
$M_s = 1.64 \times m_b - 4.75$   
(s.d. = 0.24)

Ms(pc) vs mb, mixed path 1



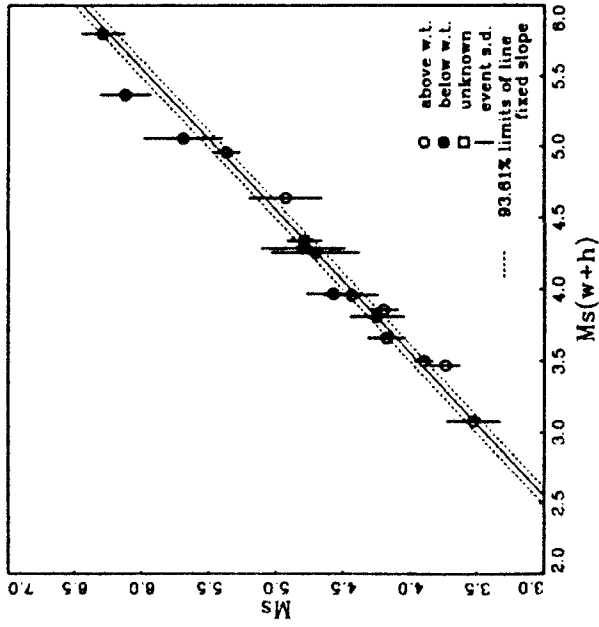
$M_s = 1.64 \times m_b - 4.68$   
(s.d. = 0.24)

Ms(pc) vs mb, mixed path 2

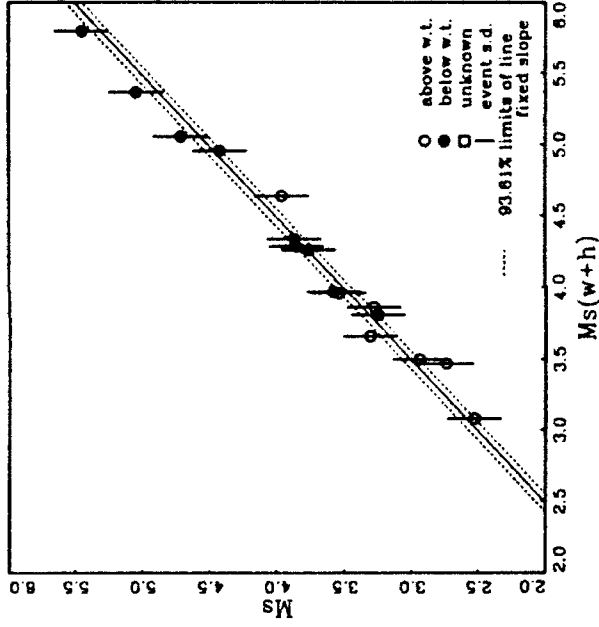


$M_s = 1.64 \times m_b - 4.89$   
(s.d. = 0.24)

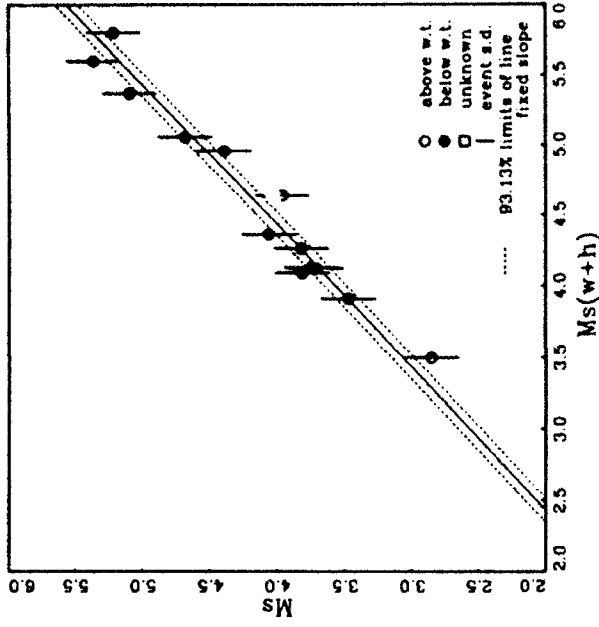
**Ms(W+H) vs. Ms(B), NTS**



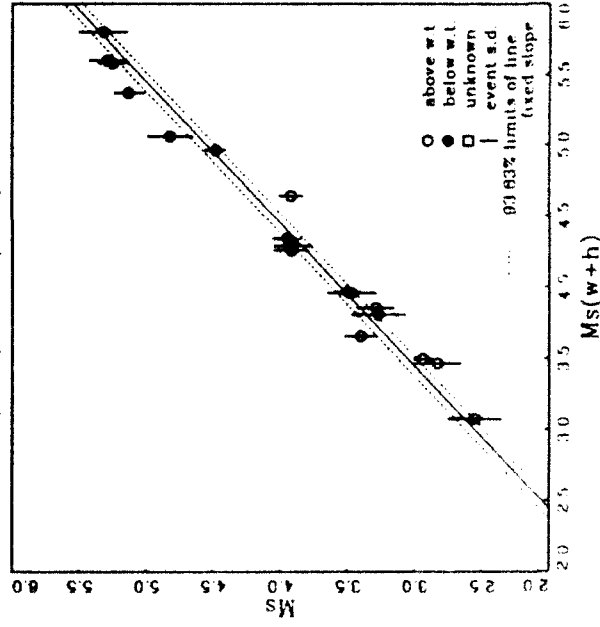
**Ms(W+H) vs. Ms(M+B), NTS**



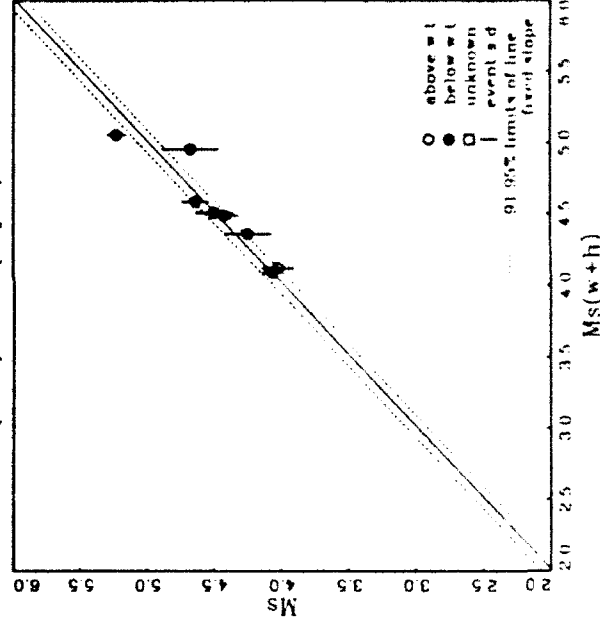
**Ms(W+H) vs. Ms(M+S+R), NTS**



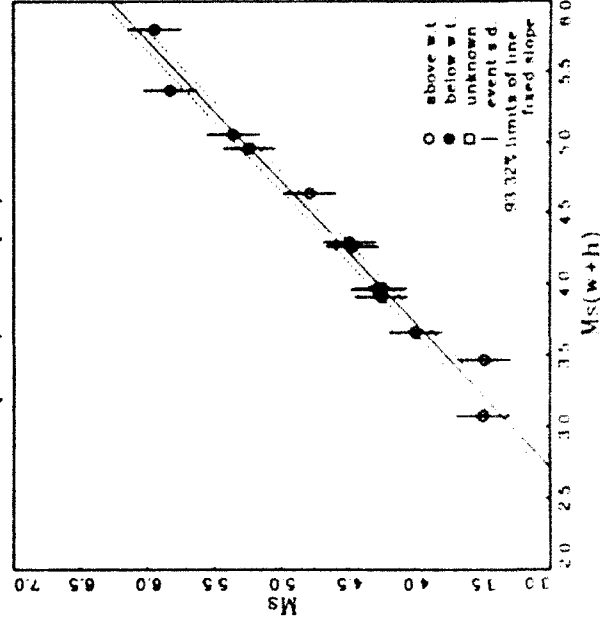
**Ms(W+H) vs. Ms(B+H), NTS**



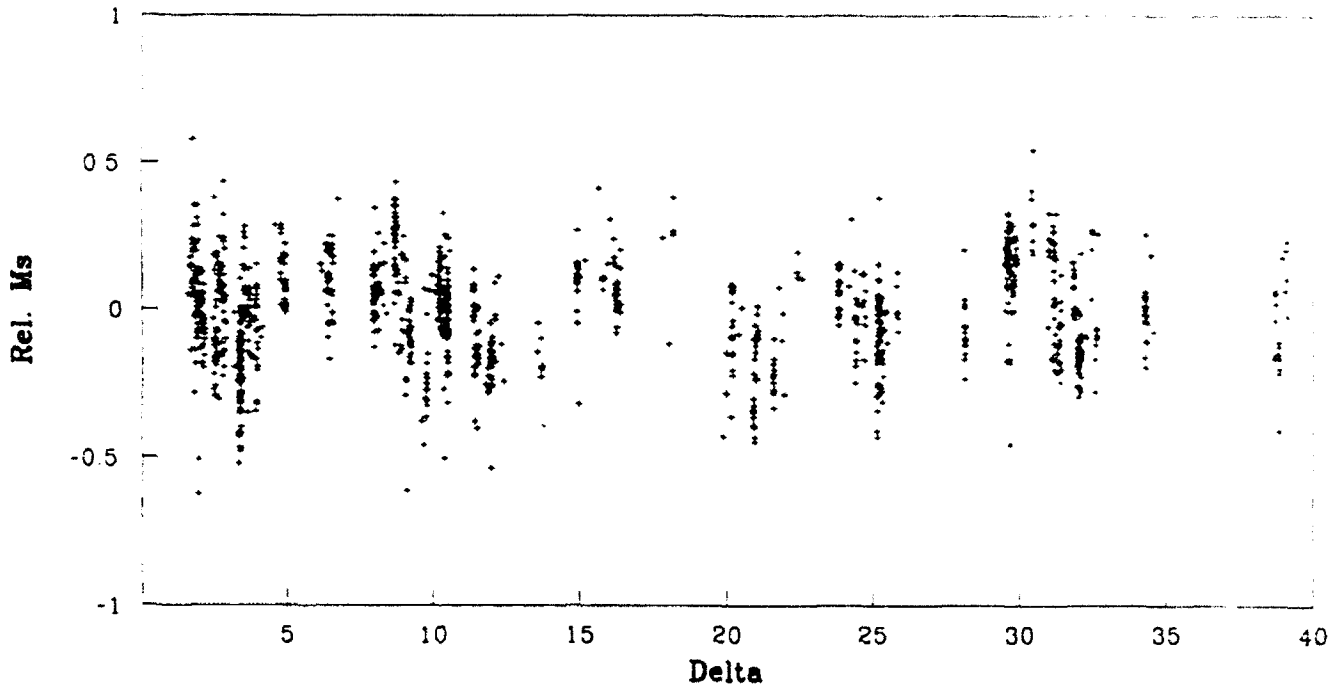
**Ms(W+H) vs. Ms(Yspec), NTS**



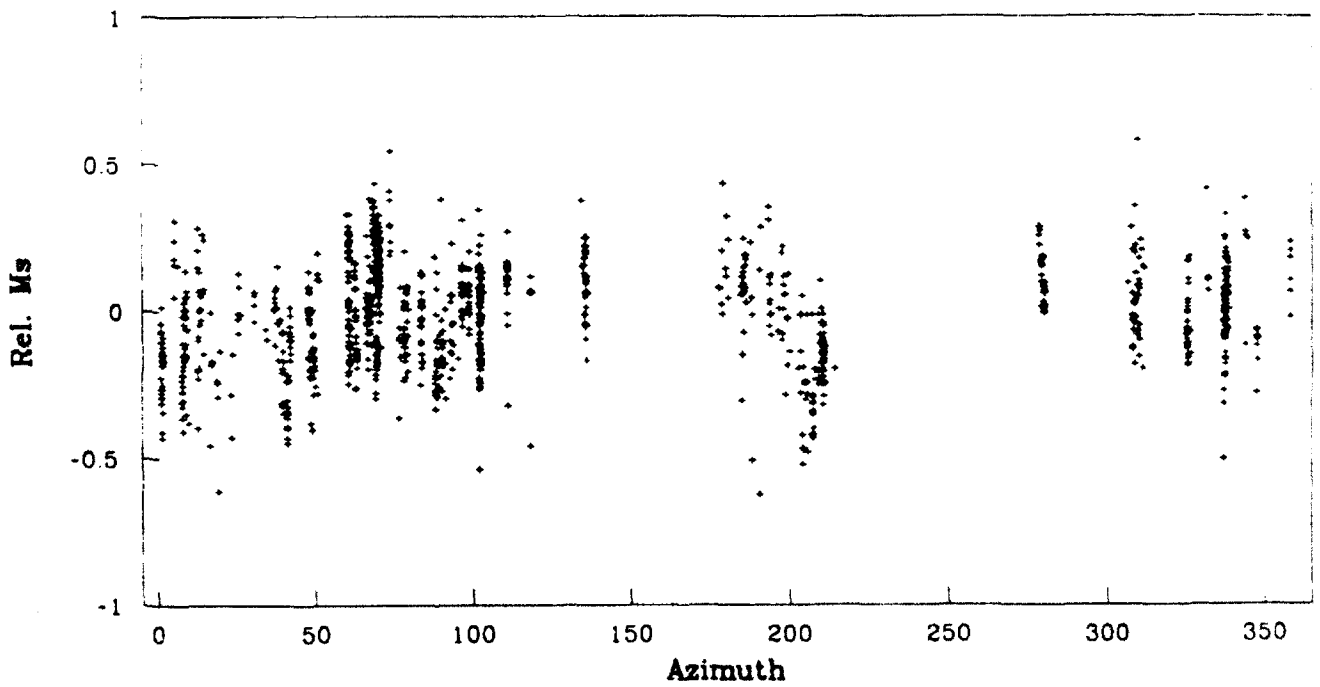
**Ms(W+H) vs. Ms(VS), NTS**

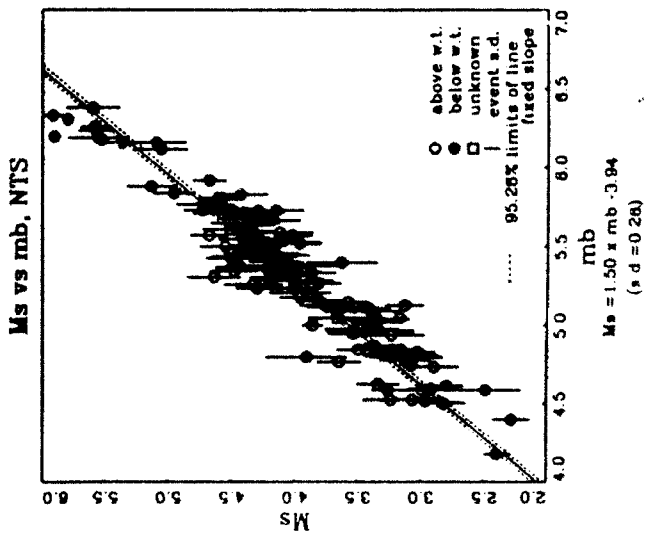
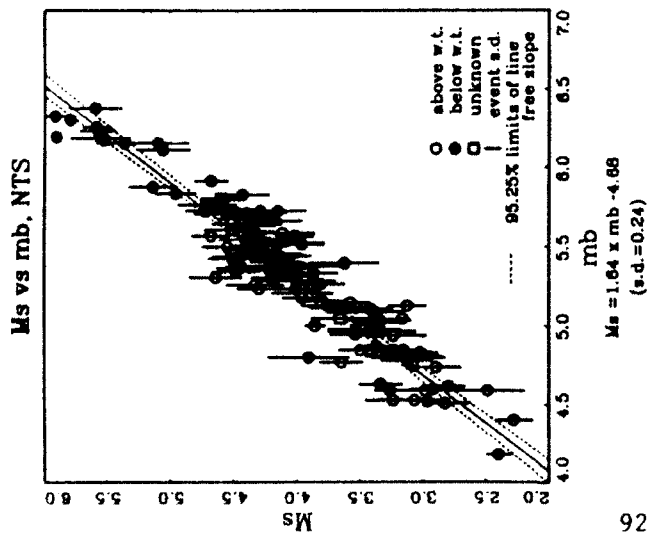
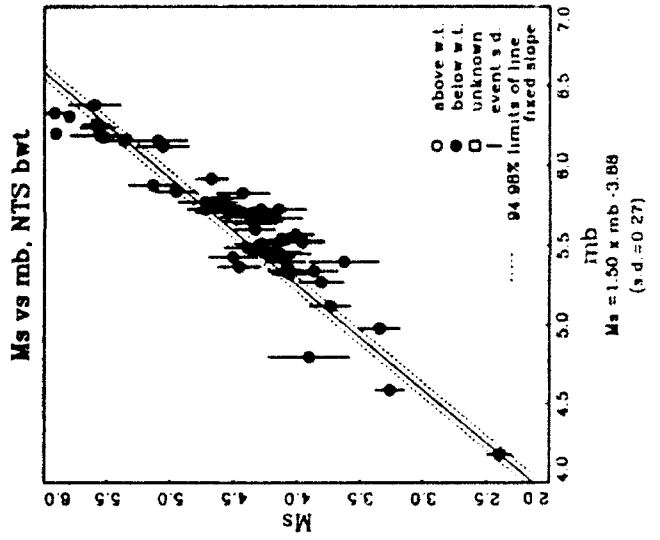
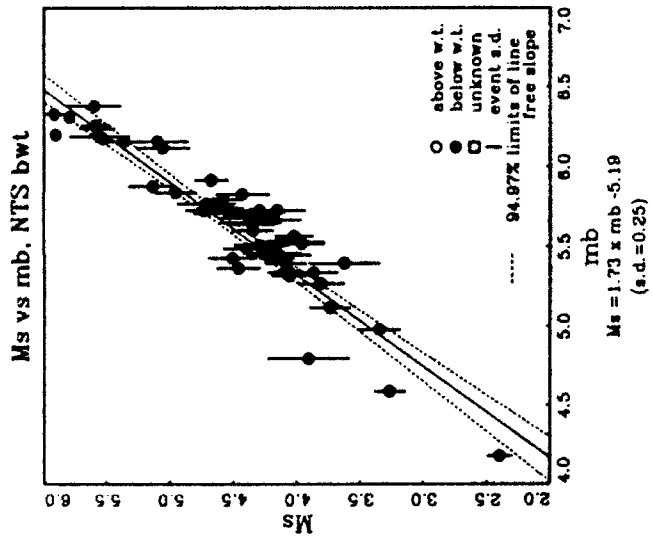
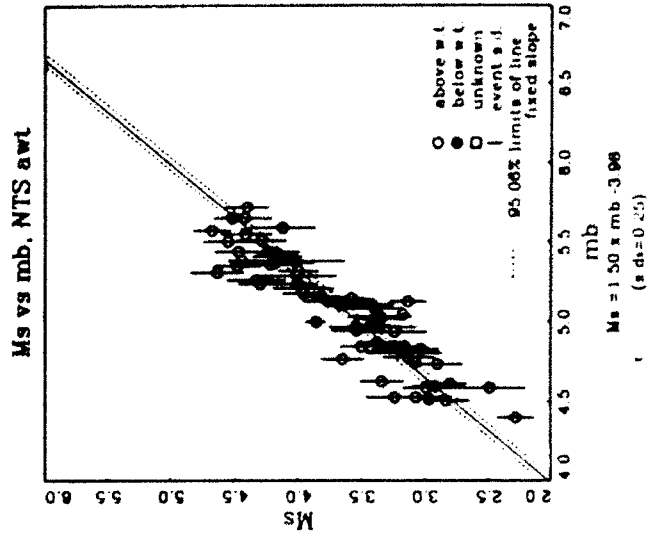
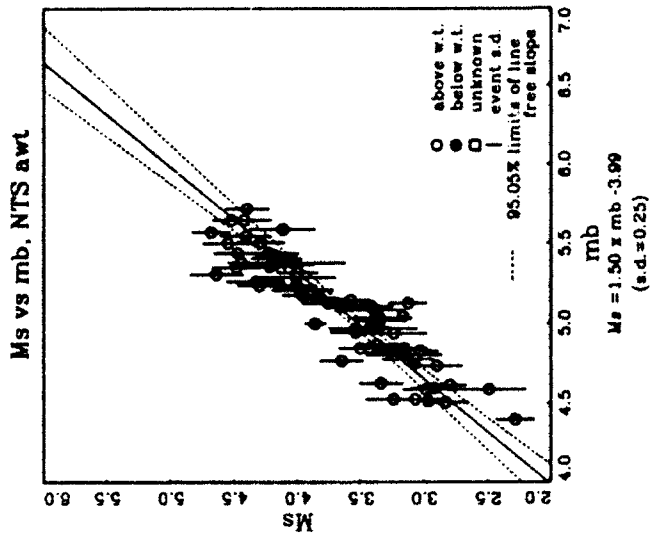


Relative Ms vs. Distance

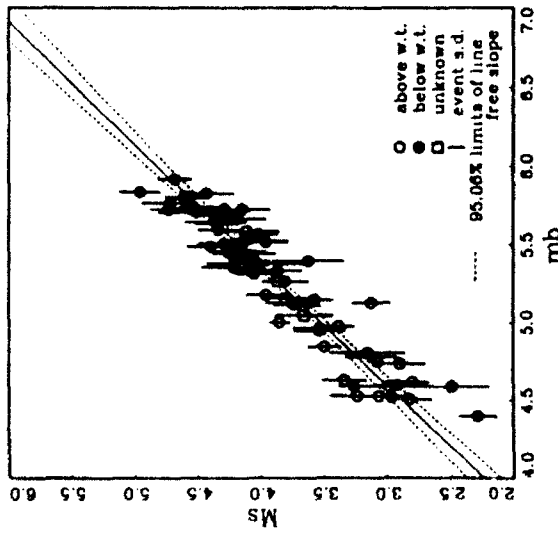


Relative Ms vs. Azimuth

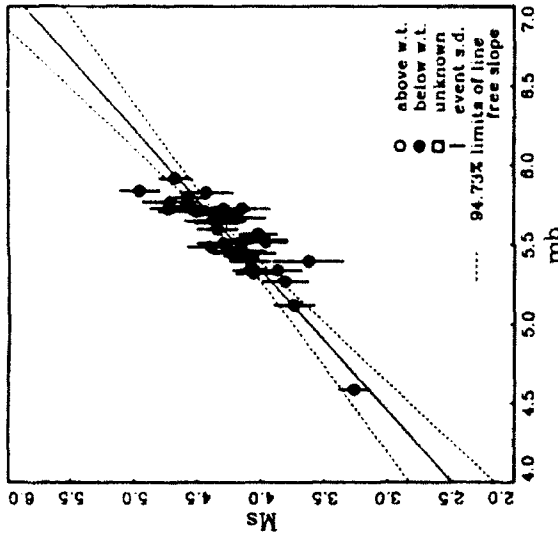




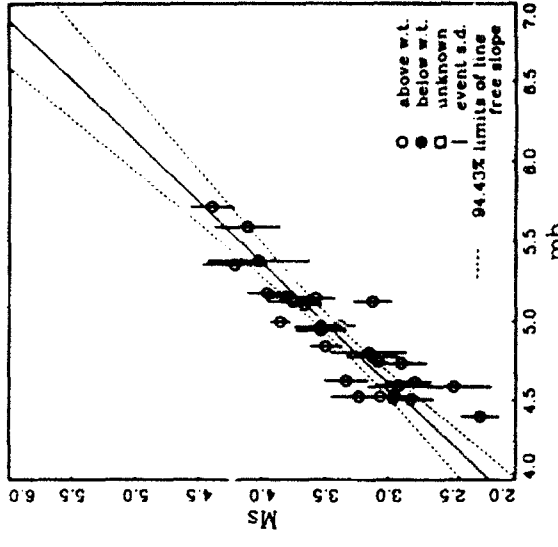
Ms vs mb, Yucca



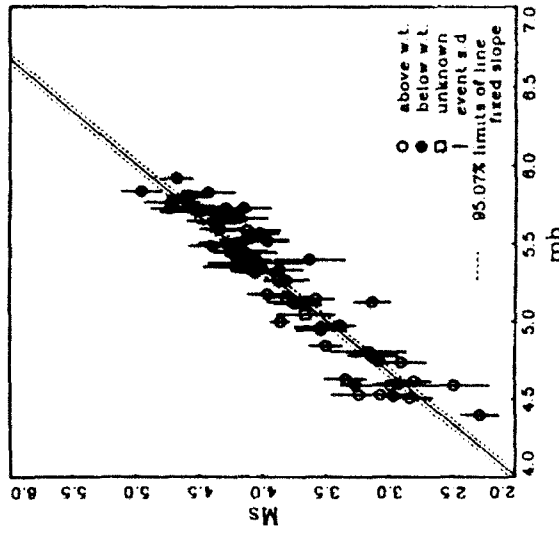
Ms vs mb, Yucca bwt



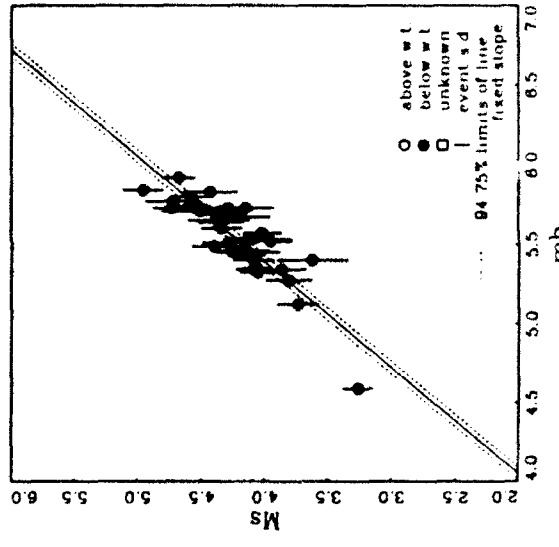
Ms vs mb, Yucca awt



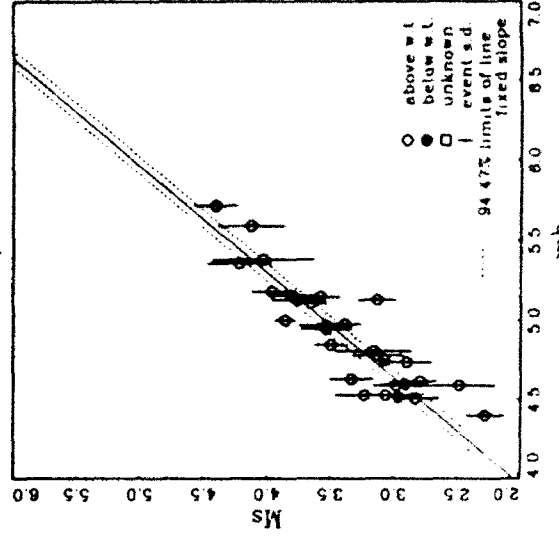
Ms vs mb, Yucca

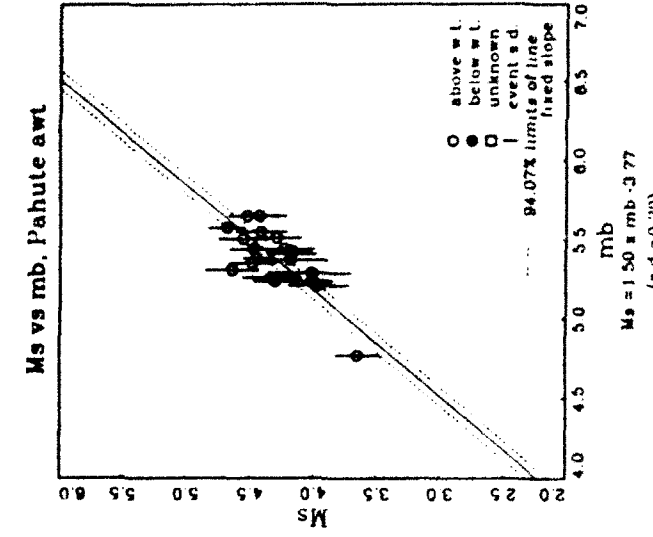
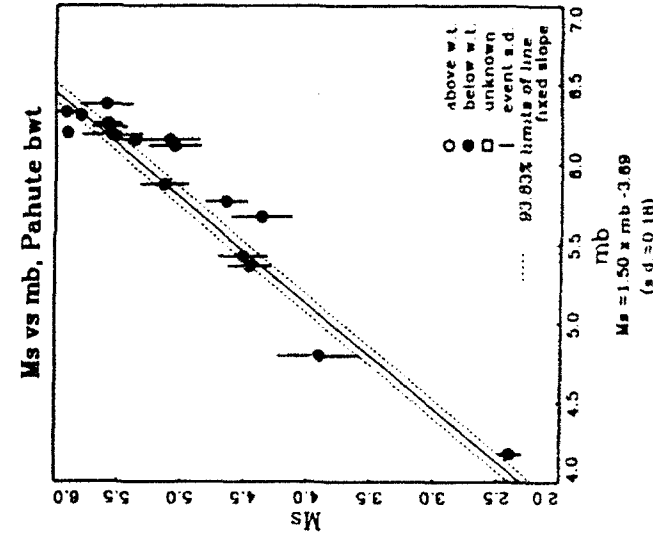
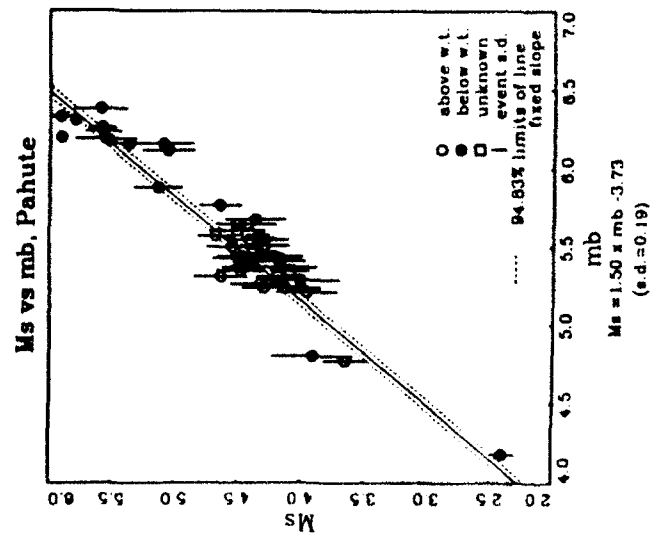
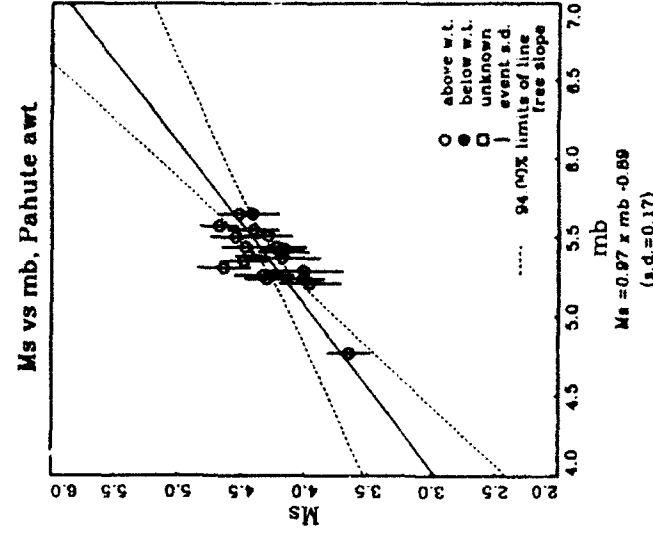
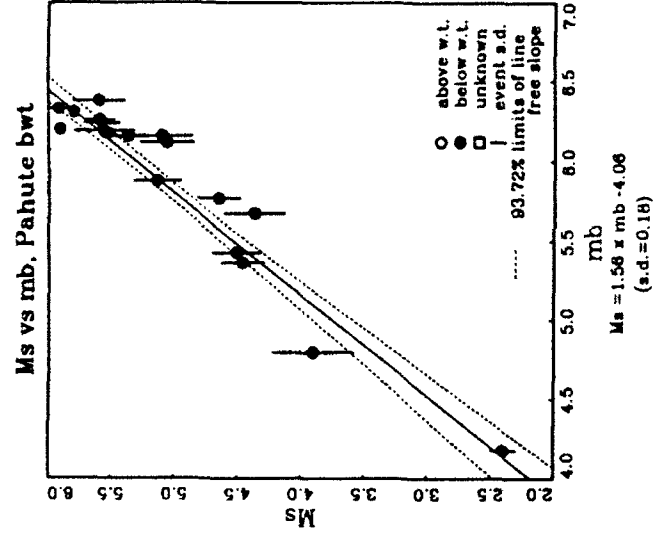
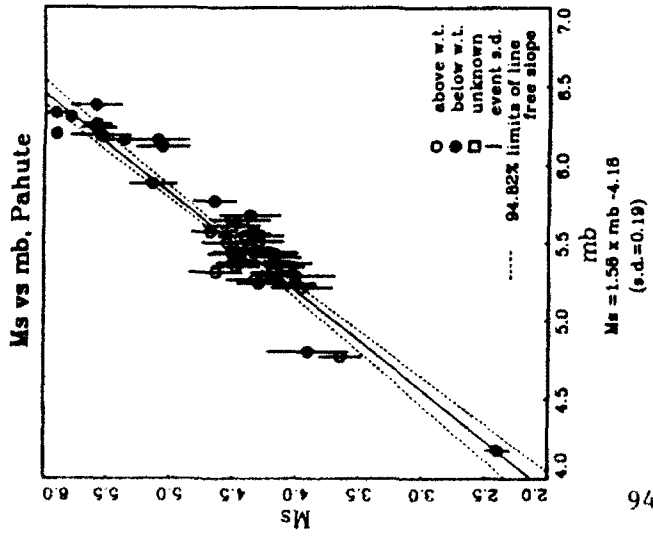


Ms vs mb, Yucca bwt



Ms vs mb, Yucca awt





Floydata, Yucca, Y < 10 Kt, mb=4.2, log-Mo=14.16 N-M

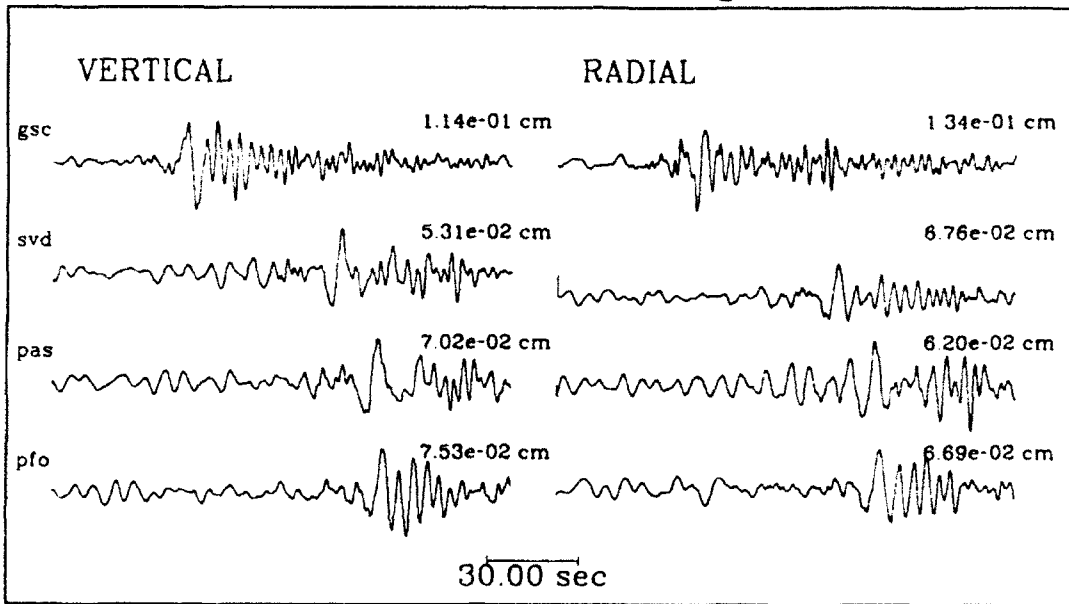


Table 1: Network Path Corrections

Dominant Period	Path Correction Dispersion	Path Correction Single Path	Path Correction Mixed Path 1	Path Correction Mixed Path 2	Station Name
11.5	-0.64	0.20	-0.07	-0.11	AAM
12.0	-0.61	0.18	-0.02	0.17	ALQ
13.5	-0.50	0.57	0.08	0.27	BKS
15.0	-0.38	-0.24	-0.28	-0.32	BLA
10.5	-0.71	0.18	0.00	-0.47	BLC
11.0	-0.67	-0.26	-0.02	0.16	BOZ
11.5	-0.64	-0.12	0.07	0.14	COR
11.0	-0.67	0.35	-0.12	0.09	DAL
12.0	-0.61	-0.03	-0.02	0.19	DUG
11.0	-0.67	-0.26	0.10	0.03	EDM
11.2	-0.66	0.26	-0.03	0.20	ELK
12.0	-0.61	-0.03	-0.03	0.12	EPT
12.0	-0.61	-0.22	0.06	0.01	FCC
12.5	-0.57	-0.22	-0.02	0.01	FFC
12.0	-0.61	-0.24	-0.12	-0.09	FLO
11.5	-0.64	0.18	0.18	-0.02	FRB
13.5	-0.50	0.45	0.20	0.25	FSJ
11.5	-0.64	-0.24	-0.12	-0.09	FVM
16.0	-0.30	0.18	0.40	-0.29	GAC
15.0	-0.38	-0.24	-0.15	-0.47	GEO
11.5	-0.64	-0.11	0.03	0.08	GOL
11.0	-0.67	0.26	-0.04	0.22	GSC
12.0	-0.61	-0.40	-0.11	-0.23	INK
11.0	-0.67	0.18	0.04	0.13	JCT
11.2	-0.66	1.06	0.02	0.26	KNB
11.2	-0.66	0.26	-0.05	0.20	LAC
12.5	-0.57	-0.13	-0.01	0.00	LHC
11.0	-0.67	0.20	0.01	0.17	LON
11.5	-0.64	-0.19	0.06	0.03	LUB
12.5	-0.57	-0.44	0.26	0.06	MBC
11.5	-0.64	0.18	0.37	-0.39	MNT
11.5	-0.64	0.26	-0.04	0.22	MNV
11.0	-0.67	-0.26	-0.03	0.14	MSO
10.5	-0.71	0.16	0.30	0.19	OGD
11.5	-0.64	0.18	0.40	-0.28	OTT
12.5	-0.57	1.12	0.03	0.27	PAS
11.0	-0.67	-0.26	-0.03	0.11	PNT
11.0	-0.67	-0.26	-0.04	0.10	RCD
11.5	-0.64	-0.39	-0.39	-0.59	RES
11.0	-0.67	-0.53	-0.17	-0.31	SCP
11.0	-0.67	-0.26	-0.05	0.07	SES
12.5	-0.57	0.03	0.04	0.09	SHA
11.5	-0.64	-0.03	-0.04	0.15	TUC
11.5	-0.64	0.45	0.16	0.27	VIC
11.5	-0.64	0.22	-0.30	-0.41	WES
12.5	-0.57	-0.40	-0.20	-0.23	YKC
19.5	-0.04	0.18	-0.02	0.17	ALQD
16.5	-0.27	0.20	0.01	0.17	LOND
16.5	-0.27	-0.53	-0.17	-0.31	SCPD
15.0	-0.38	-0.51	0.02	0.02	RSCP
16.0	-0.30	-0.09	-0.05	0.09	RSSD
15.5	-0.34	-0.19	-0.07	-0.05	RSON
16.0	-0.30	0.18	0.33	0.22	RSNY
15.5	-0.34	-0.40	-0.20	-0.23	RSNT
18.0	-0.16	1.21	0.01	0.19	JAS

TABLE 2

No. Sta.	Ms	Ms s.e.	Shot Info.	Event	Julian Date
1	2.49	-	R__	rainier	57262
1	3.25	-	R__	logan	58289
1	3.73	-	R__	blanca	58303
1	2.96	-	NBG	hardhat	62046
1	2.89	-	YAA	dormouseprime	62095
1	3.57	-	YA_	aardvark	62132
1	3.12	-	YAA	haymaker	62178
1	3.69	-	YAA	sedan	62187
1	3.66	-	YA_	mississippi	62278
2	4.85	0.22	YBT	bilby	63256
1	3.77	-	RAT	clearwater	63289
2	3.07	0.28	YAL	handcar	64310
2	2.54	0.08	YAA	merlin	65047
1	2.82	-	NAA	wishbone	65049
12	3.97	0.06	YBT	wagtail	65062
6	3.96	0.07	YAT	cup	65085
1	2.59	-	PAR	palanquin	65104
4	2.40	0.06	PBT	buteo	65132
4	3.08	0.09	NAA	dilutedwaters	65167
7	3.66	0.05	YAT	charcoal	65253
5	3.81	0.09	YBT	lampblack	66018
8	3.91	0.12	PBT	rex	66055
13	3.96	0.07	PAR	duryea	66104
5	3.47	0.11	NAT	pinstripe	66115
3	2.81	0.05	YAA	cyclamen	66125
11	4.01	0.10	PAR	chartreuse	66126
15	4.34	0.04	YBT	piranha	66133
6	3.50	0.06	YAT	discusthrower	66147
26	4.27	0.04	CBG	piledriver	66153
18	4.29	0.03	YBT	tan	66154
3	2.70	0.13	YAA	vulcan	66176
3	5.06	0.15	PBR	halfbeak	66181
3	5.37	0.11	PBT	greeley	66354
2	2.39	0.05	YAA	ward	67039
1	2.38	-	YAA	persimmon	67053
5	4.55	0.09	YAA	agile	67054
7	4.96	0.06	YBT	commodore	67140
10	4.64	0.07	PAR	knickerbocker	67146
3	3.46	0.05	RAT	midmist	67177
2	3.03	0.14	RAT	doormist	67243
5	3.86	0.04	YAT	yard	67250
1	2.08	-	YAA	marvel	67264
9	3.64	0.05	YBT	cobbler	67312
10	5.40	0.06	NBT	faultless	68019
6	3.53	0.05	RAT	dorsalfin	68060
4	2.85	0.06	N__	buggyl	68072
3	5.80	0.01	PBR	boxcar	68117
10	4.75	0.09	PAT	rickey	68167
11	4.48	0.06	PAR	chateaugay	68180
9	3.43	0.08	RAT	hudsonseal	68268
1	3.14	-	YAA	crew	68309
4	3.66	0.10	PAT	schooner	68343
4	5.92	0.08	PBT	benham	68354
11	4.03	0.05	RAT	wineskin	69015
1	3.20	-	RAT	cypress	69043

TABLE 2 (continued)

No. Sta.	Ms	Ms s.e.	Shot Info.	Event	Julian Date
15	4.06	0.04	YBT	blenton	69120
9	5.58	0.05	PBT	jorum	69259
9	4.68	0.05	PAR	pipkin	69281
3	2.11	0.06	YAT	cruet	69302
3	2.53	0.12	YAT	pod	69302
4	4.36	0.14	YBT	calabash	69302
2	3.17	0.02	R_	dieseltrain	69339
2	3.34	0.05	RAT	dianamist	70042
2	3.46	0.05	YAT	cumarin	70056
2	3.22	0.18	YAA	yannigan	70057
3	2.14	0.24	YAT	cyathus	70065
3	1.66	0.20	YAT	arabis	70065
2	2.22	0.27	YAA	jal	70078
17	4.29	0.05	YBT	shaper	70082
8	5.56	0.08	PBT	handley	70085
5	3.35	0.13	RAT	mintleaf	70125
7	3.76	0.08	YAT	cornice	70135
13	3.54	0.06	YAT	morrones	70141
2	1.79	0.33	YAT	manzanas	70141
5	3.12	0.06	RAT	hudsonmoon	70146
16	4.12	0.07	YAT	flask	70146
2	2.40	0.10	YAA	embudo	71167
4	3.01	0.09	YAT	laguna	71174
4	3.21	0.02	YAT	harebell	71175
10	3.16	0.06	RAT	camphor	71180
15	4.13	0.03	YBT	miniata	71189
21	3.63	0.06	YBT	algodones	71230
2	2.59	0.06	YAT	pedernal	71272
4	2.59	0.04	YAT	cathay	71281
4	2.29	0.17	YAA	longchamps	72110
7	3.44	0.10	RAT	mistynorth	72123
5	3.27	0.06	YBT	monero	72140
7	3.35	0.06	RBT	diamondsculls	72202
1	2.50	-	YA_	delphinium	72270
12	4.09	0.04	YBT	miera	73067
22	4.09	0.03	YBT	starwort	73116
8	3.35	0.08	RAT	didoqueen	73156
5	5.10	0.12	PBR	almendro	73157
15	4.35	0.05	YBT	latir	74058
8	3.43	0.08	RAT	mingblade	74170
20	4.59	0.05	YBT	escabosa	74191
13	3.96	0.05	YBT	stanyan	74269
15	4.02	0.04	YBA	cabrillo	75066
3	3.24	0.18	RAT	diningcar	75095
13	3.74	0.05	YBT	obar	75120
10	4.65	0.06	PBR	stilton	75154
23	4.51	0.06	YBT	mizzen	75154
3	5.53	0.02	PBT	camembert	75177
1	3.37	-	RAT	huskypup	75297
4	5.59	0.07	PBT	kasseri	75301
3	5.91	0.02	PBT	muenster	76003
14	4.49	0.05	YBT	keelson	76035
8	5.56	0.09	PBT	fontina	76043
13	5.15	0.05	PBR	cheshire	76045
6	5.62	0.11	PBT	colby	76074

TABLE 2 (continued)

No. Sta.	Ms	Ms s.e.	Shot Info.	Event	Julian Date
3	3.23	0.17	RAT	mightyepic	76133
8	4.24	0.05	YBT	rudder	76363
18	4.17	0.04	YBT	bulkhead	77117
10	4.09	0.05	YBT	crewline	77145
27	4.29	0.04	YBT	lowball	78193
4	3.12	0.17	R	diablohawk	78256
13	3.87	0.05	YBT	quargel	78322
21	4.35	0.04	YBT	quinella	79039
22	4.14	0.05	YBT	pyramid	80107
6	3.36	0.13	RAT	minersiron	80305
11	4.40	0.05	YAT	baseball	81015
10	4.18	0.07	YBT	rousanne	81316
9	4.67	0.05	YBT	jornada	82028
10	4.52	0.06	PBR	molbo	82043
8	4.41	0.08	PAR	hosta	82044
4	2.99	0.10	YAT	tenaja	82107
6	4.44	0.05	PAT	gibne	82115
15	4.29	0.04	YBT	bouschet	82127
9	4.52	0.05	PAR	nebbiolo	82175
9	3.04	0.10	YAT	monterey	82210
9	4.73	0.05	YBT	atrisco	82217
8	3.38	0.05	RAT	huronlanding	82266
5	3.54	0.11	RAT	frisco	82266b
2	2.49	0.29	YAA	seyval	82316
6	3.13	0.09	YAA	manteca	82344
2	1.80	0.01	YAA	cerro	82245
3	2.52	0.08	YBT	borrego	82272
11	4.01	0.05	PAR	cabra	83085
20	4.15	0.05	YBT	torquoise	83104
7	2.83	0.07	YAA	crowdie	83125
12	3.34	0.05	YAT	fahada	83146
10	2.93	0.06	YAA	danablu	83160
12	4.17	0.06	PAR	chancellor	83244
3	3.04	0.22	R	midnitezephyr	83264
5	2.50	0.04	YBT	techado	83265
11	3.81	0.06	YAT	romano	83350
9	3.42	0.06	RAT	midasmyth	84046
1	2.28	-	YAA	agrini	84091
19	4.40	0.04	YBT	mundo	84122
11	4.48	0.06	YBT	caprock	84152
4	3.16	0.17	YAT	duoro	84172
21	4.18	0.07	PAR	kappeli	84207
6	2.90	0.09	YAT	correo	84215
3	3.08	0.03	YAT	dolcetto	84243
5	3.58	0.08	YAT	breton	84257
4	2.80	0.08	YAA	villita	84315
12	4.23	0.06	PAT	egmont	84344
14	4.22	0.06	PAR	tierra	84350
11	4.43	0.07	YBT	tortugas	84061
5	3.39	0.06	YAT	vaughn	85074
4	4.03	0.23	YAT	cottage	85082
8	4.72	0.08	YBT	hermosa	85092
7	3.47	0.12	R_T	mistryrain	85096
19	4.37	0.06	PBT	towanda	85122
13	4.46	0.05	PBR	salut	85163

TABLE 2 (continued)

No. Sta.	Ms	Ms s.e.	Lot Info.	Event	Julian Date
12	4.30	0.05	PAR	serena	85206
4	3.24	0.13	YAT	ponil	85270
8	4.19	0.09	YBT	kinibito	85339
8	4.19	0.06	P__	goldstone	85362
4	4.07	0.06	YBT	glencoe	86081
7	3.40	0.09	RAT	mightyoak	86100
12	4.33	0.07	PAR	jefferson	86112
2	2.53	0.12	YAA	panamint	86141
7	4.22	0.10	YAT	tajo	86156
15	4.31	0.05	P__	darwin	86176
10	4.42	0.07	PAR	cybar	86198
2	2.97	0.02	YAA	cornucopia	86205
8	4.29	0.07	PAR	labquark	86273
7	4.34	0.05	P__	belmont	86289
5	4.58	0.07	YBT	gascon	86318
7	4.55	0.08	P__	bodie	86347
4	4.38	0.10	P__	delamar	87108
8	4.47	0.07	PAT	hardin	87120
4	3.66	0.14	Y__	midland	87197
5	4.60	0.08	Y__	tahoka	87225
4	4.51	0.13	P__	lockney	87267
3	3.87	0.06	Y__	borate	87296
1	4.09	-	PAT	kernville	88046
1	4.17	-	PAT	kearsarge	88230
1	3.36	-	Y__	kawich	89055

DISTRIBUTION LIST

Prof. Thomas Ahrens  
Seismological Lab, 252-21  
Division of Geological & Planetary Sciences  
California Institute of Technology  
Pasadena, CA 91125

Dr. T.J. Bennett  
S-CUBED  
A Division of Maxwell Laboratories  
11800 Sunrise Valley Drive, Suite 1212  
Reston, VA 22091

Prof. Keiiti Aki  
Center for Earth Sciences  
University of Southern California  
University Park  
Los Angeles, CA 90089-0741

Dr. Robert Blandford  
AFTAC/TT, Center for Seismic Studies  
1300 North 17th Street  
Suite 1450  
Arlington, VA 22209-2308

Prof. Shelton Alexander  
Geosciences Department  
403 Deike Building  
The Pennsylvania State University  
University Park, PA 16802

Dr. G.A. Bollinger  
Department of Geological Sciences  
Virginia Polytechnical Institute  
21044 Derring Hall  
Blacksburg, VA 24061

Dr. Ralph Alewine, III  
DARPA/NMRO  
3701 North Fairfax Drive  
Arlington, VA 22203-1714

Dr. Stephen Bratt  
Center for Seismic Studies  
1300 North 17th Street  
Suite 1450  
Arlington, VA 22209-2308

Prof. Charles B. Archambeau  
CIRES  
University of Colorado  
Boulder, CO 80309

Dr. Lawrence Burdick  
Woodward-Clyde Consultants  
566 El Dorado Street  
Pasadena, CA 91109-3245

Dr. Thomas C. Bache, Jr.  
Science Applications Int'l Corp.  
10260 Campus Point Drive  
San Diego, CA 92121 (2 copies)

Dr. Robert Burrige  
Schlumberger-Doll Research Center  
Old Quarry Road  
Ridgefield, CT 06877

Prof. Muawia Barazangi  
Institute for the Study of the Continent  
Cornell University  
Ithaca, NY 14853

Dr. Jerry Carter  
Center for Seismic Studies  
1300 North 17th Street  
Suite 1450  
Arlington, VA 22209-2308

Dr. Jeff Barker  
Department of Geological Sciences  
State University of New York  
at Binghamton  
Vestal, NY 13901

Dr. Eric Chael  
Division 9241  
Sandia Laboratory  
Albuquerque, NM 87185

Dr. Douglas R. Baumgardt  
ENSCO, Inc  
5400 Port Royal Road  
Springfield, VA 22151-2388

Prof. Vernon F. Cormier  
Department of Geology & Geophysics  
U-45, Room 207  
University of Connecticut  
Storrs, CT 06268

Dr. Susan Beck  
Department of Geosciences  
Building #77  
University of Arizona  
Tucson, AZ 85721

Prof. Steven Day  
Department of Geological Sciences  
San Diego State University  
San Diego, CA 92182

Marvin Denny  
U.S. Department of Energy  
Office of Arms Control  
Washington, DC 20585

Dr. Zoltan Der  
ENSCO, Inc.  
5400 Port Royal Road  
Springfield, VA 22151-2388

Prof. Adam Dziewonski  
Hoffman Laboratory, Harvard University  
Dept. of Earth Atmos. & Planetary Sciences  
20 Oxford Street  
Cambridge, MA 02138

Prof. John Ebel  
Department of Geology & Geophysics  
Boston College  
Chestnut Hill, MA 02167

Eric Fielding  
SNEE Hall  
INSTOC  
Cornell University  
Ithaca, NY 14853

Dr. Mark D. Fisk  
Mission Research Corporation  
735 State Street  
P.O. Drawer 719  
Santa Barbara, CA 93102

Prof Stanley Flatte  
Applied Sciences Building  
University of California, Santa Cruz  
Santa Cruz, CA 95064

Dr. John Foley  
NER-Geo Sciences  
1100 Crown Colony Drive  
Quincy, MA 02169

Prof. Donald Forsyth  
Department of Geological Sciences  
Brown University  
Providence, RI 02912

Dr. Art Frankel  
U.S. Geological Survey  
922 National Center  
Reston, VA 22092

Dr. Cliff Frolich  
Institute of Geophysics  
8701 North Mopac  
Austin, TX 78759

Dr. Holly Given  
IGPP, A-025  
Scripps Institute of Oceanography  
University of California, San Diego  
La Jolla, CA 92093

Dr. Jeffrey W. Given  
SAIC  
10260 Campus Point Drive  
San Diego, CA 92121

Dr. Dale Glover  
Defense Intelligence Agency  
ATTN: ODT-1B  
Washington, DC 20301

Dr. Indra Gupta  
Teledyne Geotech  
314 Montgomery Street  
Alexandria, VA 22314

Dan N. Hagedorn  
Pacific Northwest Laboratories  
Battelle Boulevard  
Richland, WA 99352

Dr. James Hannon  
Lawrence Livermore National Laboratory  
P.O. Box 808  
L-205  
Livermore, CA 94550

Dr. Roger Hansen  
HQ AFTAC/TTR  
Patrick AFB, FL 32925-6001

Prof. David G. Harkrider  
Seismological Laboratory  
Division of Geological & Planetary Sciences  
California Institute of Technology  
Pasadena, CA 91125

Prof. Danny Harvey  
CIRES  
University of Colorado  
Boulder, CO 80309

Prof. Donald V. Helmberger  
Seismological Laboratory  
Division of Geological & Planetary Sciences  
California Institute of Technology  
Pasadena, CA 91125

Prof. Eugene Herrin  
Institute for the Study of Earth and Man  
Geophysical Laboratory  
Southern Methodist University  
Dallas, TX 75275

Prof. Robert B. Herrmann  
Department of Earth & Atmospheric Sciences  
St. Louis University  
St. Louis, MO 63156

Prof. Lane R. Johnson  
Seismographic Station  
University of California  
Berkeley, CA 94720

Prof. Thomas H. Jordan  
Department of Earth, Atmospheric &  
Planetary Sciences  
Massachusetts Institute of Technology  
Cambridge, MA 02139

Prof. Alan Kafka  
Department of Geology & Geophysics  
Boston College  
Chestnut Hill, MA 02167

Robert C. Kemerait  
ENSCO, Inc.  
445 Pineda Court  
Melbourne, FL 32940

Dr. Max Koontz  
U.S. Dept. of Energy/DP 5  
Forrestal Building  
1000 Independence Avenue  
Washington, DC 20585

Dr. Richard LaCoss  
MIT Lincoln Laboratory, M-200B  
P.O. Box 73  
Lexington, MA 02173-0073

Dr. Fred K. Lamb  
University of Illinois at Urbana-Champaign  
Department of Physics  
1110 West Green Street  
Urbana, IL 61801

Prof. Charles A. Langston  
Geosciences Department  
403 Deike Building  
The Pennsylvania State University  
University Park, PA 16802

Jim Lawson, Chief Geophysicist  
Oklahoma Geological Survey  
Oklahoma Geophysical Observatory  
P.O. Box 8  
Leonard, OK 74043-0008

Prof. Thorne Lay  
Institute of Tectonics  
Earth Science Board  
University of California, Santa Cruz  
Santa Cruz, CA 95064

Dr. William Leith  
U.S. Geological Survey  
Mail Stop 928  
Reston, VA 22092

Mr. James F. Lewkowitz  
Phillips Laboratory/GPEH  
Hanscom AFB, MA 01731-5000( 2 copies)

Mr. Alfred Lieberman  
ACDA/VI-OA State Department Building  
Room 5726  
320-21st Street, NW  
Washington, DC 20451

Prof. L. Timothy Long  
School of Geophysical Sciences  
Georgia Institute of Technology  
Atlanta, GA 30332

Dr. Randolph Martin, III  
New England Research, Inc.  
76 Olcott Drive  
White River Junction, VT 05001

Dr. Robert Masse  
Denver Federal Building  
Box 25046, Mail Stop 967  
Denver, CO 80225

Dr. Gary McCartor  
Department of Physics  
Southern Methodist University  
Dallas, TX 75275

Prof. Thomas V. McEvelly  
Seismographic Station  
University of California  
Berkeley, CA 94720

Dr. Art McGarr  
U.S. Geological Survey  
Mail Stop 977  
U.S. Geological Survey  
Menlo Park, CA 94025

Dr. Keith L. McLaughlin  
S-CUBED  
A Division of Maxwell Laboratory  
P.O. Box 1620  
La Jolla, CA 92038-1620

Stephen Miller & Dr. Alexander Florence  
SRI International  
333 Ravenswood Avenue  
Box AF 116  
Menlo Park, CA 94025-3493

Prof. Bernard Minster  
IGPP, A-025  
Scripps Institute of Oceanography  
University of California, San Diego  
La Jolla, CA 92093

Prof. Brian J. Mitchell  
Department of Earth & Atmospheric Sciences  
St. Louis University  
St. Louis, MO 63156

Mr. Jack Murphy  
S-CUBED  
A Division of Maxwell Laboratory  
11800 Sunrise Valley Drive, Suite 1212  
Reston, VA 22091 (2 Copies)

Dr. Keith K. Nakanishi  
Lawrence Livermore National Laboratory  
L-025  
P.O. Box 808  
Livermore, CA 94550

Dr. Carl Newton  
Los Alamos National Laboratory  
P.O. Box 1663  
Mail Stop C335, Group ESS-3  
Los Alamos, NM 87545

Dr. Bao Nguyen  
HQ AFTAC/TTR  
Patrick AFB, FL 32925-6001

Prof. John A. Orcutt  
IGPP, A-025  
Scripps Institute of Oceanography  
University of California, San Diego  
La Jolla, CA 92093

Prof. Jeffrey Park  
Kline Geology Laboratory  
P.O. Box 6666  
New Haven, CT 06511-8130

Dr. Howard Patton  
Lawrence Livermore National Laboratory  
L-025  
P.O. Box 808  
Livermore, CA 94550

Dr. Frank Pilotte  
HQ AFTAC/TT  
Patrick AFB, FL 32925-6001

Dr. Jay J. Pulli  
Radix Systems, Inc.  
2 Taft Court, Suite 203  
Rockville, MD 20850

Dr. Robert Reinke  
ATTN: FCTVTD  
Field Command  
Defense Nuclear Agency  
Kirtland AFB, NM 87115

Prof. Paul G. Richards  
Lamont-Doherty Geological Observatory  
of Columbia University  
Palisades, NY 10964

Mr. Wilmer Rivers  
Teledyne Geotech  
314 Montgomery Street  
Alexandria, VA 22314

Dr. George Rothe  
HQ AFTAC/TTR  
Patrick AFB, FL 32925-6001

Dr. Alan S. Ryall, Jr.  
DARPA/NMRO  
3701 North Fairfax Drive  
Arlington, VA 22209-1714

Dr. Richard Sailor  
TASC, Inc.  
55 Walkers Brook Drive  
Reading, MA 01867

Prof. Charles G. Sammis  
Center for Earth Sciences  
University of Southern California  
University Park  
Los Angeles, CA 90089-0741

Prof. Christopher H. Scholz  
Lamont-Doherty Geological Observatory  
of Columbia University  
Palisades, CA 10964

Dr. Susan Schwartz  
Institute of Tectonics  
1156 High Street  
Santa Cruz, CA 95064

Secretary of the Air Force  
(SAFRD)  
Washington, DC 20330

Office of the Secretary of Defense  
DDR&E  
Washington, DC 20330

Thomas J. Sereno, Jr.  
Science Application Int'l Corp.  
10260 Campus Point Drive  
San Diego, CA 92121

Dr. Michael Shore  
Defense Nuclear Agency/SPSS  
6801 Telegraph Road  
Alexandria, VA 22310

Dr. Matthew Sibol  
Virginia Tech  
Seismological Observatory  
4044 Derring Hall  
Blacksburg, VA 24061-0420

Prof. David G. Simpson  
IRIS, Inc.  
1616 North Fort Myer Drive  
Suite 1440  
Arlington, VA 22209

Donald L. Springer  
Lawrence Livermore National Laboratory  
L-025  
P.O. Box 808  
Livermore, CA 94550

Dr. Jeffrey Stevens  
S-CUBED  
A Division of Maxwell Laboratory  
P.O. Box 1620  
La Jolla, CA 92038-1620

Lt. Col. Jim Stobie  
ATTN: AFOSR/NL  
Bolling AFB  
Washington, DC 20332-6448

Prof. Brian Stump  
Institute for the Study of Earth & Man  
Geophysical Laboratory  
Southern Methodist University  
Dallas, TX 75275

Prof. Jeremiah Sullivan  
University of Illinois at Urbana-Champaign  
Department of Physics  
1110 West Green Street  
Urbana, IL 61801

Prof. L. Sykes  
Lamont-Doherty Geological Observatory  
of Columbia University  
Palisades, NY 10964

Dr. David Taylor  
ENSCO, Inc.  
445 Pineda Court  
Melbourne, FL 32940

Dr. Steven R. Taylor  
Los Alamos National Laboratory  
P.O. Box 1663  
Mail Stop C335  
Los Alamos, NM 87545

Prof. Clifford Thurber  
University of Wisconsin-Madison  
Department of Geology & Geophysics  
1215 West Dayton Street  
Madison, WI 53706

Prof. M. Nafi Toksoz  
Earth Resources Lab  
Massachusetts Institute of Technology  
42 Carleton Street  
Cambridge, MA 02142

Dr. Larry Turnbull  
CIA-OSWR/NED  
Washington, DC 20505

DARPA/RMO/SECURITY OFFICE  
3701 North Fairfax Drive  
Arlington, VA 22203-1714

Dr. Gregory van der Vink  
IRIS, Inc.  
1616 North Fort Myer Drive  
Suite 1440  
Arlington, VA 22209

HQ DNA  
ATTN: Technical Library  
Washington, DC 20305

Dr. Karl Veith  
EG&G  
5211 Auth Road  
Suite 240  
Suitland, MD 20746

Defense Intelligence Agency  
Directorate for Scientific & Technical Intelligence  
ATTN: DTIB  
Washington, DC 20340-6158

Prof. Terry C. Wallace  
Department of Geosciences  
Building #77  
University of Arizona  
Tuscon, AZ 85721

Defense Technical Information Center  
Cameron Station  
Alexandria, VA 22314 (2 Copies)

Dr. Thomas Weaver  
Los Alamos National Laboratory  
P.O. Box 1663  
Mail Stop C335  
Los Alamos, NM 87545

TACTEC  
Battelle Memorial Institute  
505 King Avenue  
Columbus, OH 43201 (Final Report)

Dr. William Wortman  
Mission Research Corporation  
8560 Cinderbed Road  
Suite 700  
Newington, VA 22122

Phillips Laboratory  
ATTN: XPG  
Hanscom AFB, MA 01731-5000

Prof. Francis T. Wu  
Department of Geological Sciences  
State University of New York  
at Binghamton  
Vestal, NY 13901

Phillips Laboratory  
ATTN: GPE  
Hanscom AFB, MA 01731-5000

AFTAC/CA  
(STINFO)  
Patrick AFB, FL 32925-6001

Phillips Laboratory  
ATTN: TSML  
Hanscom AFB, MA 01731-5000

DARPA/PM  
3701 North Fairfax Drive  
Arlington, VA 22203-1714

Phillips Laboratory  
ATTN: SUL  
Kirtland, NM 87117 (2 copies)

DARPA/RMO/RETRIEVAL  
3701 North Fairfax Drive  
Arlington, VA 22203-1714

Dr. Michel Bouchon  
I.R.I.G.M.-B.P. 68  
38402 St. Martin D'Herès  
Cedex, FRANCE

Dr. Michel Campillo  
Observatoire de Grenoble  
I.R.I.G.M.-B.P. 53  
38041 Grenoble, FRANCE

Dr. Jorg Schlittenhardt  
Federal Institute for Geosciences & Nat'l Res.  
Postfach 510153  
D-3000 Hannover 51, GERMANY

Dr. Kin Yip Chun  
Geophysics Division  
Physics Department  
University of Toronto  
Ontario, CANADA

Dr. Johannes Schweitzer  
Institute of Geophysics  
Ruhr University/Bochum  
P.O. Box 1102148  
4360 Bochum 1, GERMANY

Prof. Hans-Peter Harjes  
Institute for Geophysic  
Ruhr University/Bochum  
P.O. Box 102148  
4630 Bochum 1, GERMANY

Prof. Eystein Husebye  
NTNF/NORSAR  
P.O. Box 51  
N-2007 Kjeller, NORWAY

David Jepsen  
Acting Head, Nuclear Monitoring Section  
Bureau of Mineral Resources  
Geology and Geophysics  
G.P.O. Box 378, Canberra, AUSTRALIA

Ms. Eva Johannisson  
Senior Research Officer  
National Defense Research Inst.  
P.O. Box 27322  
S-102 54 Stockholm, SWEDEN

Dr. Peter Marshall  
Procurement Executive  
Ministry of Defense  
Blacknest, Brimpton  
Reading FG7-FRS, UNITED KINGDOM

Dr. Bernard Massinon, Dr. Pierre Mechler  
Societe Radiomana  
27 rue Claude Bernard  
75005 Paris, FRANCE (2 Copies)

Dr. Svein Mykkeltveit  
NTNT/NORSAR  
P.O. Box 51  
N-2007 Kjeller, NORWAY (3 Copies)

Prof. Keith Priestley  
University of Cambridge  
Bullard Labs, Dept. of Earth Sciences  
Madingley Rise, Madingley Road  
Cambridge CB3 0EZ, ENGLAND